8

RF System for the Main Linacs

Contents

8.1 Introduction

The basic design of the NLC main linacs rests on global experience gained from the design, construction, and 30 years of operation of the 3-km-long SLAC linac, which is powered at a frequency of 2.856 GHz [Seeman 1991, Seeman 1993]. Since its initial operation in 1966, the SLAC linac has been continuously upgraded for higher energy, higher intensity, and lower emittance.

The radio frequency (rf) system for the NLC main linacs is similar in character to the SLAC linac. The SLAC linac is currently energized by 240 high-power S-band klystrons. The klystron peak power and pulse duration are, respectively, 65 MW and 3.5 μs. The power from each klystron is compressed by a SLED pulse compressor, and then split to feed four, 3-m-long, constant-gradient S-band accelerator structures operating in the $2\pi/3$ mode.

When the SLAC linac was built, the accelerating gradient was 7 MV/ m. The original design included a future upgrade path in which the number of klystrons would be quadrupled. The upgrades that were eventually implemented involved replacing each of the initial 24-MW klystrons with a single higher-power klystron (first with 35-MW, XK-5 tubes and, later on, with 65-MW, 5045 tubes), and adding a SLED pulse compressor downstream of each klystron. For present-day SLC operations, fully upgraded with 240 SLEDed, 65-MW klystrons, the accelerating gradient has been tripled, to 21 MV/ m, and the maximum beam energy is 60 GeV (for unloaded, on-crest operation).

8.1.1 Overview

The rf power system for the NLC's two high-gradient linacs that accelerate the electron and positron beams separately from 10 GeV to 250 GeV (in the initial design), and to 500 GeV or more (after the upgrade), operates at 11.424 GHz. This system includes all the hardware through which energy flows, from the AC line to the accelerator structures. Figure 8-1 shows one module of the rf system schematically, with emphasis on the flow of energy. Electrical energy is transformed at each stage shown in the diagram: the modulator converts AC power into high-voltage pulsed DC, the klystron transforms pulsed DC into high peak power rf, the SLED-II pulse-compression system increases the peak power by about a factor of four (at the expense of a reduced pulse width), and the accelerator sections convert rf power into beam power. Because of the high average rf power required to drive the accelerator structures, it is important that the highest possible efficiency be maintained for the processing and transmission of energy at every stage of the rf system.

The primary technical choice for the rf system is the use of the 11.424-GHz frequency. This frequency, high in the X-band (8.2–12.4 GHz), is exactly four times the operating frequency of the existing SLAC 60-GeV linac. The choice of such a high frequency, relative to existing high-energy linacs, allows higher accelerating gradient, shorter linac length, and lower AC power consumption for a given beam energy. Considering the size, weight, cost, and availability of standard microwave components, we have chosen a frequency in the X-band for a design that is upgradeable from an initial 250-GeV beam energy to 500 GeV or more. This choice requires the development of klystrons capable of delivering peak power significantly greater than previously achieved by commercially available X-band sources. As described in Section 8.4, klystrons which meet the 50-MW peak-power goal necessary for the initial 250-GeV beam energy in the NLC design have been developed, and are now operating in the Klystron Test Laboratory at SLAC.

The general parameters of the high-power rf system and its major subsystems (klystrons, modulators, rf pulse compressors, and the accelerator structure itself) are specified in Table 8-1. The set of parameters has been optimized to provide high acceleration gradient (35–64 MV/ m) for trains of bunches with moderate charge per bunch (1.2–1.8 nC). This optimization keeps single-bunch wakefields under control and reduces the beamstrahlung at the collision point to tolerable levels. The upgrade to 500-GeV beam energy (1-TeV center-of-mass energy) is accomplished by doubling

the number of modulators (as shown by dashed lines in Figure 8-1), and by replacing each 50-MW klystron with a pair of 75-MW klystrons. The total active length of linac must also be increased from 16,300 m to 17,700 m. The upgrade also includes improvements in the modulator and pulse compression systems to increase the rf system efficiency. The upgrade to 1-TeV center-of-mass energy is described in more detail in Section 8.1.2.

The rf accelerator structure (discussed in Section 8.2) is designed to be very nearly a constant-gradient traveling-wave structure. The design of the structure has been optimized to reduce the wakefield seen by trailing bunches. This has been accomplished by tailoring the cell-to-cell frequency distribution of the dominant deflecting mode to yield an initial Gaussian-like decay of the wakefield amplitude. On a longer timescale, the higher-order beam-induced modes of the structure will be damped by vacuum manifolds to which each cell of the structure is coupled. This structure is designated by the acronym DDS (damped detuned structure). The damping manifolds run parallel to the beam channel and are terminated into matched loads. (The slots that couple the cells to the manifolds are cut off to the fundamental accelerating mode.) This damping scheme will reduce the typical quality (Q) factors of the deflecting modes to about 1000. The first prototype 1.8-m-long accelerator section, which was detuned but not damped, was high-power tested up to a gradient of 67 MV/ m. The effect of the detuning in that first prototype section was demonstrated experimentally by using positron and electron bunches from the SLC damping rings as probe and witness beams, respectively. Another prototype 1.8-m section that is both damped and detuned is being manufactured and will be used for a similar test before it is installed in the NLCTA.

Obtaining the X-band peak power for the NLC has required the development of klystrons (Section 8.4) capable of delivering peak power significantly greater than previously achieved by commercially available X-band sources. Both the peak power and the pulse length have already been achieved by four solenoid-focused X-band klystrons at SLAC. These klystrons will be used to power the NLC Test Accelerator (Section 8.1.3). The most recent refinement of the klystron has achieved the peak power and exceeded the pulse length required for the NLC design and upgrade, at an efficiency of 48%. The solenoid which focuses the electron beam in the prototype klystrons has a weight of 750 kg and a power consumption of 20 kW. Currently nearing completion is the first prototype of a 50-MW klystron which is focused instead by a periodic permanent magnet (PPM) array of samarium cobalt ring magnets weighing about 9 kg. It is this klystron, which operates at a higher voltage and lower beam current for compatibility with PPM focusing, which is slated as the prototype for the NLC. Based on computer projections, the tube, designated X5011, is expected to operate at about 57% efficiency with 50 MW of peak output power.

Each high-power rf station consists of a pair of PPM-focused klystrons (50 or 75 MW) and a pulsed-DC energy delivery system (modulator) that is tightly integrated in design with the electron guns of the klystrons. The modulator system (discussed in Sections 8.5 and 8.7) includes a single-thyratron switch, a Blumlein pulse-forming network (PFN), a high-efficiency power supply for charging the PFN's capacitance, and a pulse transformer. Using a Blumlein PFN allows for a relatively low transformer turns ratio (7:1), which yields a reasonably fast rise time (0.3 μs), and hence, an improved efficiency.

The rf pulse-compression system (discussed in Section 8.3) is based on the SLED-II technique which is a modification of the SLED system currently in use on the existing 60-GeV SLAC linac. For SLED-II, the energy storage cavities of SLED are replaced by resonant delay lines in order to produce flat output pulses. A prototype SLED-II system has been tested up to compressed-pulse power levels of 200 MW. Transmission of high power with low loss is accomplished by using oversized waveguide components. Three SLED-II systems are being manufactured for the NLC Test Accelerator.

To achieve a highly mono-energetic multibunch beam pulse for the final focus, the beam loading induced by the bunch train must be compensated. The initial transient can be eliminated by pre-loading the sections by shaping the input rf pulse using an approximately linear rise of the field amplitude for one filling time of the structure. In this way, the first electron bunch will see a filled rf structure that appears to be in the steady state. As will be seen, this requires phase-agile control of the rf before it is amplified by the klystron.

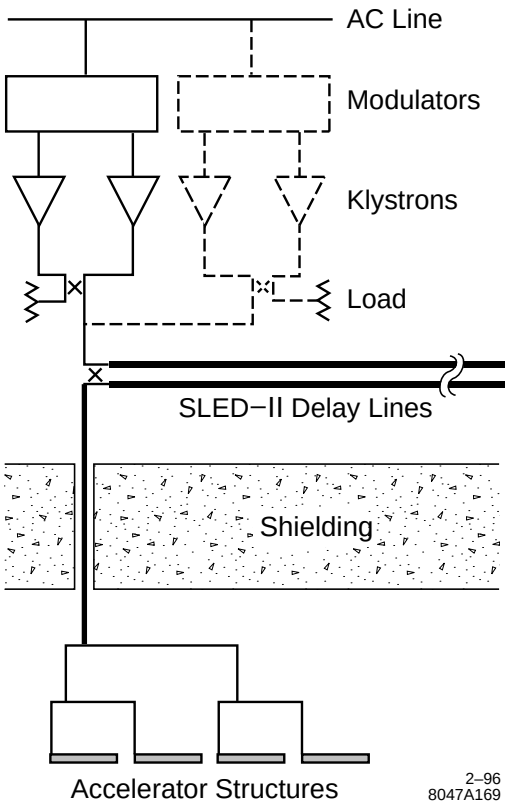

Figure 8-1. *One module of the high-power rf system for the main linacs. Dashes indicate additions for the beam-energy upgrade from 250 GeV to 500 GeV. Energy flows from the AC line to the accelerator structures.*

The design of the rf control system proposed for the NLC main linacs is based on experience derived from operating the SLAC linac. In particular, the methods of beam-loading compensation have been inspired, in part, by experience gained with beam-loading compensation while operating the SLAC linac in its long-pulse, high-average-current mode (for fixed-target experiments).

8.1.2 Upgrade to 1 TeV

As mentioned previously, the upgrade to 1-TeV center-of-mass energy is accomplished primarily by doubling the number of klystrons and modulators, and by increasing the peak power per klystron from 50 MW to 75 MW. Taking into account a small reduction in the power gain of the rf pulse compression system (which has been upgraded for higher efficiency at a lower compression ratio), this increase in rf power provides for an increase in the unloaded accelerating gradient from 50 MV/m to 85 MV/m. To obtain a center-of-mass energy of 1 TeV, the active linac length must also be increased slightly, from 16,300 m to 17,700 m. (If this additional length is not provided, the upgraded energy will be about 925 GeV).

A major part of the upgrade to 1 TeV will be to increase the efficiency of the rf system so that the AC wall-plug power is kept below 200 MW. After the 500-GeV design has been finalized, and before the 1-TeV upgrade is carried out,

	NLCTA Achieved	500-GeV Design Goal	1-TeV Upgrade
General Parameters			
Frequency (GHz)	11.4	11.4	11.4
Accel. Gradient (MV/m), Unloaded/Loaded	67/–	50/35.3	85/63.5
Overhead Factor,[a] F_{OH}		1.20	1.15
Active Linac Length[b] (m)	1.8	16,300	17,700
Total Linac Length (m) (1.08 × Active Length)		17,600	19,100
# 7.2-m RF Units and Pulse-Compression Systems		2264	2454
# Modulators		2264	4908
# Klystrons		4528	9816
Peak Power per Meter of Structure (MW/m)		50	145
RF Pulse Length at Structure (ns)	150	240	240
Repetition Rate (Hz)	60	180	120
Particles per Bunch (10^{10})		0.75	1.10
Number of Bunches per Pulse		90	90
Peak Beam Current (A)		0.86	1.26
RF Energy/Pulse at Structure Input (J/m)		12.0	34.7
Total Average RF Power at Structure[c] (MW)		34.1	71.3
Klystron			
Output Power (MW)	50, 75	50	75
Pulse Length (μs)	2.0, 1.1	1.2	0.96
Microperveance (μA/V$^{3/2}$)	1.2	0.6	0.75
Electronic Efficiency[d] (%)	48	57	60
Beam Voltage (kV)	440	465	487
Beam Energy per Pulse[e] (J)	310, 130	105	119
Focusing	Electromagnet	PPM	PPM
Cathode Loading (A/cm^2)	7.4	7.4	7.6
Overall Length (m)	1.3	1.3	1.3
Cathode Heater Power[f] (kW)		0.33	0.41
Modulator (Blumlein PFN, transformer ratio 7:1)			
PFN Voltage (kV)	48	68	71
Pulse Rise Time (ns)	500	275	175
Rise/Fall Energy Efficiency (%)		80	83
I^2R/Thyratron/Core Loss Efficiency (%)		97	97
Net Energy Transfer Efficiency (%)		77.4	80.6
$\frac{1}{2}$CV^2, two klystrons (J)		272	295
Power Supply Efficiency (%)		93	93
Net Modulator Efficiency (%)	58	72	75
Thyratron Heater + Reservoir Power[f] (kW)		1.5	1.5
Average AC Input Power (kW), Excl. Aux.	45	53	38

Table 8-1. *NLC main linac rf system parameters. (Continued on next page.)*

	NLCTA Achieved	500-GeV Design Goal	1-TeV Upgrade
RF Pulse Compression			
System Type	SLED-II	SLED-II	BPC/DLDS
Compression Ratio	5–7	5	4
Intrinsic Efficiency (%)	80.4–69.2	80.4	100
Loss Efficiency of Delay Lines, 3-db Coupler and Mode Converters (%)	92–90	95	93
Pulse Compression Efficiency (%)	73–64	76.5	93
Pulse Compression Power Gain	3.7–4.5	3.8	3.7
Power Transmission Efficiency (%)	90	94	94
Net Pulse-Compression Efficiency (%), Including Power Transmission Loss	66–58	72	87.5
Net Power Gain	3.3–4.1	3.6	3.5
Net RF System Parameters			
Total AC Power (MW), Excl. Aux.		116	181
RF System Efficiency (%), Excl. Aux.	19	29.6	39.4
Total Auxiliary Power[g] (MW)		5.4	12
Total AC Power, Including Auxiliary (MW)		121	193
RF System Efficiency (%), Including Auxiliary		28.2	37.0
Average Beam Power[h] (MW)		9.3	18.6
AC-to-Beam Efficiency (%)		7.7	9.4

[a] Includes overhead for BNS, feedback, and stations off for repair (see Table 7-1).

[b] Active length = F_{OH} ($E_0 - 20$ GeV)/(Loaded Gradient).

[c] Assumes 3% of klystrons and modulators are off (repair margin) or running off beam time (on standby).

[d] Given by simulated efficiency less 5 percentage points for 500-GeV design; equal to simulated efficiency for 1-TeV design.

[e] Useful energy in flat-top portion of pulse.

[f] Included in auxiliary power.

[g] Also includes power for modulators on standby (0.5%).

[h] Excludes injected beam power.

Table 8-1. *(continued): NLC main linac rf system parameters.*

several years of additional R&D will be possible in order to realize these potential gains in efficiency. The parameters listed in Table 8-1 for the 1-TeV upgrade are therefore somewhat less conservative than for the 500-GeV design.

In order to realize a substantial gain in the net rf system efficiency, each of the subsystems—klystrons, modulators, and pulse compression—must be examined for potential efficiency improvements. A slight gain is assumed in klystron efficiency (from 57% to 60%) by pushing closer to efficiency values given by simulations which are, in turn, expected to increase as experience is gained in klystron design. A modest improvement is assumed in modulator efficiency (from 72% to 75%), due mainly to a reduction in pulse transformer rise time. Several design approaches are being studied to reduce rise time. The greatest gain in rf system efficiency will result from an upgrade in the rf pulse compression system. The SLED-II system used in the 500-GeV design has a maximum intrinsic efficiency of 80.4%, even for lossless components, due mainly to reflected power during the period when the resonant delay lines are being charged with energy.

The SLED-II efficiency may be improved by using an active microwave switch to rapidly change the coupling (or Q) of the resonant delay lines [Tantawi 1995b]. Such a switch might be implemented as an optically-triggered silicon device operating in a low-field region of the microwave network. Experimental studies of optically-triggered silicon

devices for this purpose are underway at SLAC [Tantawi 1995c]. For a compression ratio of 4, the efficiency of the Q-switched SLED-II would be about 91%. Including the 94% power transmission efficiency, the net efficiency would be about 85% (a power gain of 3.4). Assuming the improvement in SLED-II efficiency can be realized, it remains to be determined that the power handling capability of the SLED-II configuration is adequate for the combined power of four 75-MW klystrons. (SLED-II has demonstrated its ability to handle a single 50-MW klystron. Tests with two 50-MW klystrons are expected to be performed in Summer 1996. Tests with four 75-MW klystrons will be performed when the 75-MW klystrons become available.)

An alternate upgrade path is to replace the SLED-II with a different type of rf pulse compression. By replacing this system with a Binary Pulse Compression (BPC) system [Farkas 1986, Lavine 1991], which has an intrinsic efficency of 100%, the net pulse compression efficiency (including power transmission losses) can be increased from 75% to 87.5%. At the same time, the compression ratio is reduced from 5 to 4, and the klystron pulse length is reduced from 1.2 μs to 0.96 μs. The higher compression efficiency together with the lower compression ratio results in a slight reduction in power gain from 3.6 to 3.5. The power-handling capability required of the BPC configuration is only half that of SLED-II because the BPC system has two outputs, each of which feeds only two structures, in contrast to SLED-II where a single output feeds four structures. The chief disadvantage of the BPC scheme is the longer length of delay-line pipe which is required (three times that for SLED-II). When upgrading from SLED-II, the components of the existing SLED-II delay lines can be reconfigured as the shorter of the two required BPC delay lines. However, an additional delay, twice as long, must be added to each system.

Variations of BPC can be utilized. Half of the BPC delay can be eliminated by the use of the Delay Line Distribution System (DLDS), as proposed at KEK. In the DLDS, rf energy is propagated upstream (toward the gun) by a distance equal to one half the required delay; the beam propagation time provides the other half of the delay. Loaded delay lines can also be used in principle to reduce the length of the added delay line.

Both of the above upgrade paths (adding Q switches to SLED-II, or replacing SLED-II with BPC or a variation of BPC) can be performed gradually, taking only one station offline at a time.

Since the BPC concept has been experimentally demonstrated [Lavine 1991], and the Q-switched SLED-II capable of handling four 75-MW klystrons has not, the upgrade path in Table 8-1 is based on the more conservative option of replacing the SLED-II systems with BPC systems. Additional R&D during the years after the 500-GeV design has been finalized, and before the 1-TeV upgrade, may make the Q-switched SLED-II (or other developments) possible, and more attractive.

Taken together, the above improvements lead to an increase in net rf system efficiency from about 30% for the 500-GeV design to almost 40% for the 1-TeV upgrade. Some of these potential design improvements may, in fact, be ready in time to be included in the final design of a 500-GeV machine. The 500-GeV parameters listed in Table 8-1 are, however, conservatively based on experience with, and measurements on, prototypes which exist at the present time.

8.1.3 The NLC Test Accelerator (NLCTA)

The design of the high-power X-band rf system for the NLC is based on specific experience gained from building X-band prototypes and operating them at high power, and on an rf systems-integration test—the Next Linear Collider Test Accelerator (NLCTA)—which is currently under construction at SLAC. The goals of the NLCTA project [SLAC 1993, Ruth 1993] are to integrate the technologies of X-band accelerator structures and high-power rf systems, to demonstrate multibunch beam-loading energy compensation and suppression of higher-order beam-deflecting modes, to measure any transverse components of the accelerating field, and to measure the growth of the dark current generated by rf field emission in the accelerator. The NLCTA design parameters and a possible upgrade path are summarized in Table 8-2.

The peak power and rf-system efficiency needed for the NLCTA have been demonstrated in a prototype system (discussed in Section 8.3.1). Upgrades to the NLCTA rf system will test the SLED-II design at the higher power levels and efficiencies needed for the NLC (Table 8-7). The NLCTA high-power rf system is depicted schematically in Figure 8-2. The system is comprised of four modules. Each module consists of a DC pulse modulator, up to two X-band klystrons (50 or 75 MW), a SLED-II pulse compressor, and two X-band accelerator sections. One module serves the injector. Three modules serve the linac. Power from the third and fourth modules will be combined in the pulse compressor of the third module, and then re-divided to energize the last four accelerator sections in order to test the topology that is proposed for the NLC.

The six accelerator sections in the NLCTA linac are each 1.8-m long. The two accelerator sections in the injector are similar to the linac sections, except that each is 0.9-m long to maintain beam loading comparable to the linac in the presence of approximately twice the current. All the X-band sections in the NLCTA will suppress transverse wakefields, either by cell-to-cell detuning [Thompson 1993], or by a combination of detuning and damping [Kroll 1994], as discussed in Section 7.4.2. The effect of detuning has been demonstrated experimentally with the prototype 1.8-m detuned X-band section by using positron and electron bunches from the SLC damping rings as probe and witness beams, respectively [Adolphsen 1994], as discussed in Section 8.2.10.

The high-power rf source for the NLCTA is the 50-MW, X-band klystron [Wright 1994] discussed in Section 8.4.2. Thus far, four prototype tubes (XL1, XL2, XL3, and XL4) have been manufactured and operated at 50-MW peak power for the required 1.5-μs pulse duration at 60 pulses per second.

Rf pulse compression in the NLCTA will be performed by the SLED-II technique. A prototype SLED-II system has been tested with an X-band klystron at compressed-pulse power levels up to 200 MW, to validate the design of the NLCTA pulse-compression system and its components [Nantista 1993], as discussed in Section 8.3. Power from the SLED-II prototype has been used to achieve a 67-MV/m accelerating gradient in the prototype 1.8-m-long accelerator section in the Accelerator Structure Test Area (ASTA) of the Klystron Test Laboratory at SLAC [Vlieks 1993, Wang 1994].

To achieve low rf losses, oversized circular waveguide will be used for the SLED-II delay lines and for the transmission lines that carry the rf from the klystron to SLED-II, and from SLED-II to the accelerator. The TE_{01} mode will be propagated in the circular waveguide. Matching to the TE_{10} mode in rectangular waveguide will be performed by compact, low-loss-mode transducers [Tantawi 1993], as discussed in Section 8.3.

The NLCTA rf system has been designed to accommodate the possibility of a future upgrade which would increase the accelerating gradient from 50 MV/m to 85 MV/m by replacing each 50-MW klystron with a pair of 75-MW klystrons. Each NLCTA pulse modulator is capable of accommodating a pair of either 50-MW or 75-MW tubes.

The 70-MeV, X-band injector module and two of the three 130 MeV, X-band linac modules of the NLCTA are expected to become operational in 1996, with each module powered by a single 50-MW klystron. The first accelerator physics experiments are planned for 1996–1997. The last linac rf module (including the fifth and sixth 1.8-m-long X-band sections) is planned to be installed in 1997. It is expected that the upgrade from 50-MW klystrons to 75-MW klystrons will occur gradually as the new higher-power tubes become available through the klystron development program. The initial complement of 50-MW klystrons, and the first of the 75-MW klystrons, will be solenoid-focused. Later versions of both 50-MW and 75-MW klystrons are expected to be focused by cylindrical arrays of PPMs, as discussed in Section 8.4.

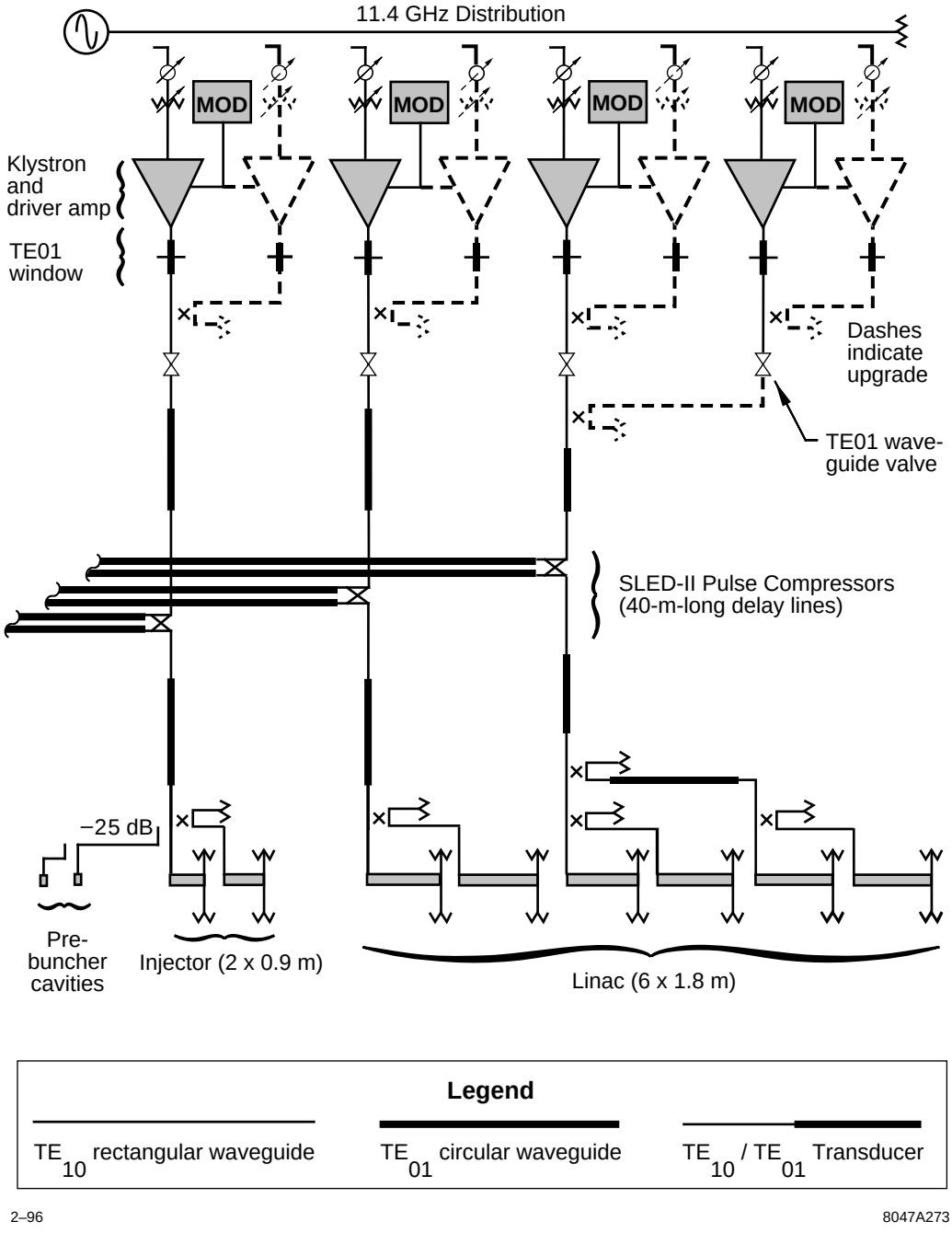

Figure 8-2. *Schematic layout of the NLC Test Accelerator's high-power rf system.*

Parameter	Design	Possible Upgrade
Beam:		
Electrons per bunch	0.4×10^9	6.5×10^9
Bunch frequency	11.424 GHz	0.714 GHz
Bunches per pulse	1440	90
Pulse length	0.125 μs	
Beam pulse repetition rate	10 Hz	
Accelerator:		
Accelerating gradient, unloaded	50 MV/m	85 MV/m
Accelerating gradient, full current	37 MV/m	64 MV/m
Filling time	0.1 μs	
Section length	1.8 m	
Sections per module	2	
Modules in linac (excluding injector)	3	
RF Pulse Compression:		
Compressed rf pulse length	0.25 μs	
Compression ratio	6	
Efficiency (intrinsic $\times$ components)	0.75 $\times$ 0.90 = 0.67	
Peak power gain	4.0	
RF Power Transmission:		
Transmission Efficiency	0.86	
Klystrons:		
Klystrons per module	1	2
Peak rf power per klystron	50 MW	75 MW
Klystron pulse length	1.5 μs	1.1 μs
Voltage	440 kV	500 kV
Perveance	1.2 μA/ V$^{3/2}$	0.75 μA/ V$^{3/2}$
Electronic efficiency	0.43	0.60
Rf pulse repetition rate	180 Hz	120 Hz

Table 8-2. *NLCTA design parameters and a possible upgrade path.*

8.1.4 Outlook

The design of the rf system for the main linacs of the NLC is supported by existing and planned developmental prototypes, and by the NLCTA. Key NLC parameters such as the klystron power, acceleration gradient, and pulse-compression power gain have been exceeded in prototype systems. The next steps in the development program are completion of the NLCTA, the first damped and detuned structure, and the first PPM klystron prototype. The design of the NLC high-power rf system is mature and is progressing toward detailed engineering considerations. Because of the magnitude of the project, special emphasis is now being placed on designing for manufacturability and for overall system reliability.

8.2 Accelerator Structure

The design of the X-band accelerator structures for the NLC is based on theoretical and experimental experience gained by numerically modeling and building accelerator structures for the NLCTA, and operating them at high gradients. One of the main challenges is to suppress the deflecting modes that will otherwise cause severe multibunch emittance growth in the NLC linacs. Suppression of the transverse wakefield will be achieved through a combination of precision alignment and by detuning and damping higher-order modes. Another challenge in the design of the accelerator structures for the NLC is suppressing field emission at the high-surface field gradients encountered in these structures. This suppression, so far, has been achieved through machining, processing, and handling techniques that minimize surface roughness and eliminate contamination of the high-gradient surfaces. Other, additional methods may be adopted later.

There is a significant amount of overlap in the discussions of the previous chapter and this present one, since both deal with the design and performance of the main linacs. The previous chapter focused on beam dynamics issues, most importantly preservation of the beam emittance and stability. This chapter is concerned with the systems needed to accelerate the beams. This section outlines an engineering design of the accelerator structures that will meet the beam dynamics requirements.

As part of the process of developing the structure design for the NLC, several 1.8-m NLC-type accelerating structures are being built for use in the NLCTA. These are of two types: some with detuning alone, and others with both detuning and damping. In both cases, the accelerator structure is a disk-loaded waveguide driven at 11.424 GHz, the phase advance per cell for the accelerating mode is chosen to be $2\pi/3$, and the detuned distribution of the synchronous lowest dipole-mode frequencies has a density in frequency space that is Gaussian with truncation at $\pm 2\sigma$ and a total detuning range of 10%. (Only damped, detuned structures will be used in the NLC main linacs.)

The frequency spread in this detuned-mode distribution results in an interference between modes that strongly attenuates the corresponding component of the wakefield that drives multibunch beam break-up. The desired Gaussian distribution of detuned modes is obtained (while also keeping the accelerating mode frequency fixed) by varying the dimensions along the structure, the main influence coming from the cell radii (*b*) and the iris radii (*a*). To reduce the smaller but non-negligible effect of the higher dipole modes, we also vary the disk thickness (t) ranging from 1 mm in the first cell to 2 mm in the last cell, in a truncated Gaussian pattern having standard deviation $\sigma_t = 0.25$ mm. (See discussion in Section 7.4.2.) Because the number of cells used to implement the Gaussian detuning pattern is finite, the wakefield resurges on a distance scale of about $c/2\Delta f \approx 30$ m, where Δf is the cell-to-cell frequency separation in the center of the distribution. To suppress this resurgence of the long-range wakefield, the damped and detuned structure (DDS) incorporates dipole-mode damping in addition to the detuning discussed above. This damping is accomplished by coupling each accelerator cell to four evacuated waveguide manifolds running parallel to the structure, symmetrically located around its circumference. The manifolds are terminated at each end by matched

loads. No manifold modes propagate at the frequency of the accelerating mode, so there can be large coupling to the dipole modes without significant damping of the accelerating mode. (We have set a limit of a few percent degradation of the shunt impedance of the accelerating mode.) Because the higher-order modes are tuned to different frequencies, one finds (Section 7.4.2) that they have a broad spectrum of phase velocities of both signs. They are therefore capable of coupling effectively to all propagating modes in the damping manifolds.

In this section, we discuss the calculation of the dimensions of the individual cells, which vary along the structure. Next, tolerances on the dimensions and alignment of the cells in the structure are discussed. Following this, the steady-state unloaded and beam-loaded gradients are calculated. In the absence of beam-loading compensation, there would be a large sag (on the order of 25%) in the beam energy during the first 100 ns (equal to the structure filling time) following beam turn-on. There are several possibilities for compensating this transient energy variation. The method chosen here is to tailor the amplitude of the rf power during the structure filling time so that the exact steady-state beam-loaded gradient (at every position along the length of the structure) is present at the moment the beam passes through. This method of multibunch energy compensation has already been introduced in Section 7.4.5, where for simplicity the approximation of a constant-gradient structure was assumed. In this chapter the scheme is extended to calculate the exact final amplitude function needed for the NLC quasi-constant-gradient structure described here.

We then dicuss in some detail the mechanical design of the structure, including vacuum and thermal calculations, high-power tests, and material handling and processing techniques.

Next, we summarize the tolerances on ripple of the phase and amplitude of the incoming rf pulse that are needed to meet given requirements on the energy and energy spread of the multibunch beam. The experimental program planned for the NLC Test Accelerator, which is designed to achieve these tolerances, is discussed.

Finally, we discuss some of the tests and diagnostics related to the detuning and damping of the accelerator structures. The Accelerator Structure SETup (ASSET) Facility at SLAC uses the SLC positron and electron bunches to probe and witness, respectively, the wakefields in accelerator structures. Excitations of the dipole modes in a structure may be used as a diagnostic to measure the alignment of the structure with respect to the beam.

8.2.1 Calculation of Structure Dimensions

The task of designing the accelerator structure includes calculating the physical dimensions of a set of cells with a common rf feed (a section) that results in a truncated Gaussian distribution for the lowest dipole-mode frequencies, while maintaining the desired frequency and phase advance per cell for the accelerating mode. The truncated Gaussian distribution has a given standard deviation σ_f and a density of frequency components near the central frequency $\bar{f}_1$ proportional to $\exp[-(f-\bar{f}_1)^2/\,2\sigma_f^2]$. This means that the spacing between adjacent modes near the ith mode is given implicitly by

$$\mathrm{erf}\left(\frac{f_{1,i}-\bar{f}_1}{\sqrt{2}\,\sigma_f}\right) = \mathrm{erf}\left(\frac{f_{1,i-1}-\bar{f}_1}{\sqrt{2}\,\sigma_f}\right) + A \quad , \tag{8.1}$$

where A is a constant, given by

$$A \equiv \frac{2\,\mathrm{erf}\,(n_\sigma/2\sqrt{2})}{N-1} \quad . \tag{8.2}$$

Here, N is the number of cells in the accelerator structure,

$$n_\sigma \equiv \Delta f_{\mathrm{tot}}/\sigma_f \tag{8.3}$$

is the full width of the truncated distribution in units of σ_f, and $\mathrm{erf}\,(x)$ is the error function:

$$\mathrm{erf}(x) \equiv \frac{2}{\sqrt{\pi}}\int_0^x e^{-u^2}\,du \quad . \tag{8.4}$$

In the central core of the distribution, the fractional spacing between adjacent frequency components is approximately

$$\frac{\delta f}{\bar{f}_1} \approx \frac{\sqrt{2\pi}}{N-1}\frac{\sigma_f}{\bar{f}_1}\,\mathrm{erf}\left(\frac{n_\sigma}{2\sqrt{2}}\right) \quad . \tag{8.5}$$

We discuss next how we arrive at structure dimensions that satisfy these requirements on the accelerating mode and higher-order modes. Increasing the cavity radius b causes both the accelerating mode frequency and the first dipole-mode frequency f_1 to decrease, while increasing the iris radius a leads to an increased accelerating mode frequency and a decreased first dipole-mode frequency. As noted earlier, we also choose to vary the disk thickness t in a specified pattern. Keeping the frequency of the accelerating mode constant (11.424 GHz) yields a unique relation between iris radius a, cell radius b, and disk thickness t. Each of these triplets (a, b, t) corresponds to a different dipole-mode frequency. If a certain detuning range of the dipole modes is given, and t is varied in the specified truncated Gaussian pattern from 1 mm to 2 mm, the triplets (a, b, t) for the two end-cells of the accelerator section can be found. It is always possible to find a unique triplet (a, b, t) to set the dipole-mode frequency to any value between the frequencies of the first and last cells and also to keep the frequency of the accelerating mode constant; we choose to vary the lowest dipole-mode frequency in a truncated Gaussian pattern, with total frequency spread of about 10% and truncation at $\pm 2\sigma_f$.

We first discuss the calculation of dimensions for the detuned structure. The overall design procedure, which uses polynomial three-parameter fits, is as follows:

1. Using the computer code YAP [Nelson 1992a], the relationship among a, b, and t, given the fixed accelerating frequency and phase advance per cell ($2\pi/3$), may be found for the structure (taking into account the effect of the rounded corners on the irises).
2. Again using YAP, the relationship among the synchronous dipole-mode frequency f_1, a, b, and t may be found (where b is fixed by step 1).
3. The desired spacings of the dipole-mode frequencies, $\{f_{1,i} - f_{1,i-1}\}$, and the distribution of disk thicknesses, $\{t_i\}$, are specified. As already noted, both of these are chosen to be truncated Gaussian distributions.
4. Given a value a_1 for the iris radius of the first cell, the central frequency $\bar{f}_1$ and all of the a_i and b_i are uniquely determined by the above constraints. We adjust a_1 to obtain the desired filling time T_f for the structure.

The resulting structure parameters are summarized in Table 8-3. When a parameter varies along the structure, the range of values from the first to the last cell is given.

This procedure must be further modified to calculate the dimensions for the DDS. The reduction of each cell diameter required to compensate for the presence of the damping manifolds is calculated using the 3-D MAFIA code. Starting from the (a, b) pairs obtained for the purely detuned structure, we calculate the increment in b that is needed to tune the fundamental mode back to the desired rf frequency of 11.424 GHz. These calculations are to be verified by microwave measurements on a series of uniform cavity stacks corresponding to different cavities in the section.

For an accelerator structure consisting of N cells, the above procedure gives the frequencies of the synchronous dipole modes for each of N periodic structures, where each such structure is constructed from cells like one of those in the actual structure. The relationship between the dipole mode frequencies in these equivalent periodic structures and the coupled-mode frequencies (and mode field distribution patterns) in the 206-cell accelerator structures is calculated using equivalent circuit models, both for the undamped detuned structure [Bane 1993a] and for the DDS [Kroll 1994]. In the case of the DDS, the damping of the structure modes due to their coupling to the manifolds is also obtained from the model. Detailed discussion of these equivalent circuit models and the resulting calculations of long-range wakefields were given in Section 7.4.2.

Accelerating mode frequency	11.424 GHz
Phase advance per cell	$2\pi/3$
Structure length	1.8 m
# of cells	205 + 1 couplers
Iris radius, a	0.572 to 0.390 cm
Cell radius, b	1.084 to 0.998 cm
Disk thickness, t	1 to 2 mm
Frequency range of dipole modes	14.312 to 15.834 GHz
Mean dipole-mode frequency, $\bar{f}_1$	15.073 GHz
$\sigma_f/\bar{f}_1$	2.5%
Total fractional spread, $\Delta f_{\rm tot}/\bar{f}_1$	10.1%
Group velocity, v_g/c	0.12 to 0.03
Filling time, T_f	100 ns
Attenuation parameter, τ	0.533
Elastance, $s \equiv \omega r/Q$	652 to 946 V/pC/m
Peak power per feed (for 50 MV/m unloaded)	89.8 MW
Q of lowest dipole mode	≈ 6500

Table 8-3. *Parameters for an NLC structure.*

8.2.2 Tolerances on Dimensions and Alignment

The tolerance on the structure dimensions, particularly on cell radius b, comes from the effect on the distribution of dipole mode frequencies, which is designed to be a truncated Gaussian. The tolerance on the frequency is roughly the core spacing of the truncated Gaussian distribution of frequencies. The tolerance on misalignments of the structures comes from the effect on the transverse emittance of the multibunch beam. This tolerance is dependent on the longitudinal correlation length of the misalignments, but it is fairly tight on all scales. (See Section 7.4.6: "Structure Misalignments".) Both these tolerances are looser for the DDS than for the undamped Gaussian detuned structure.

Tolerances on Frequency Errors

There are two extreme cases for the frequency errors: the case where the error in each frequency in the design distribution is the same in all sections (we denote this as "systematic"), and the case where the error in each frequency is totally random from section to section. Note that our definition of systematic means that the errors are the same in corresponding cells of a given structure type, but they are still random from cell to cell in each structure type. Systematic errors can lead to considerable worsening of the long-range wakefield behavior; the totally random errors are much less harmful. If care is taken to randomize the production of various cell types, it should be possible to keep the systematic components of the errors significantly smaller than the random component, perhaps by nearly an order of magnitude.

As one might expect, the transverse multibunch beam emittance growth is not much affected by the frequency errors, provided that the fractional errors in the frequency distribution are kept small compared to the core spacing.

For a single detuned accelerator section, the fractional core spacing $\delta f/\bar{f}_1$ for the fundamental dipole-mode frequencies is about 3×10^{-4}. Machining precisions for conventional machining and diamond-point machining (obtained at KEK), and alignment tolerances of stacks of cells, are given in Table 8-4. Since the cell radius is about a centimeter,

diamond point machining should produce a random $\delta f/f$ error somewhat less than the core spacing. The systematic error, as noted above, should be significantly less than this.

Misalignment Tolerances

Misalignment tolerances, on scales ranging from a few cells within a structure to several structures, were discussed in the preceding chapter. It was found that the tightest tolerances occurred for the alignment of groups of about 20–40 cells. Thus, great care must be taken in brazing together the subsections of structures after their initial assembly from individual cups.

8.2.3 Calculation of Steady-State Gradients

In this section, we discuss the calculation of the unloaded and loaded accelerating gradients. We also discuss the proposed compensation of the transient beam loading that occurs during the first filling time after the beam is injected.

Unloaded Gradient

The power flow in the accelerator structure can be expressed as

$$P(z) = P_{in} e^{-2\tau(z)} \quad , \tag{8.6}$$

where P_{in} is the input power and $\tau(z)$ is the attenuation along the structure, given by:

$$\tau(z) = \omega_{rf} \int_0^z \frac{dz'}{2Q(z')v_g(z')} \quad . \tag{8.7}$$

The shunt impedance $r(z)$ can be calculated using the code SUPERFISH. Then the accelerating electric field $E_z(z)$ can be calculated as

$$E_z(z) = \sqrt{r(z)\frac{dP(z)}{dx}} \quad , \tag{8.8}$$

where $r(z)$ is the shunt impedance per unit length. In Figure 8-3, $E_z(z)$ is shown for an input power of 100 MW. For comparison, $E_z(z)$ for a conventional constant-gradient structure and for a constant-impedance structure, with the same input power and attenuation as the detuned structure, are also plotted.

Beam-loaded Gradient

In this section, we generalize Equation 8.8 so that the discrete nature of the structure is explicitly taken into account. The analysis is then extended to include beam loading. The underlying assumption is that the structure parameters vary slowly and smoothly with length, and that the structure can be treated as locally periodic. In this case, the unloaded steady-state gradient in the nth cell is given by

$$G_0(n) = \left[2\alpha(n)r(n)P(n)\right]^{1/2} \quad , \tag{8.9}$$

where α is the attenuation parameter per unit length. It is related to the other structure parameters by

$$\alpha = \frac{\omega}{2v_g Q} = \frac{s}{2v_g r} \quad , \tag{8.10}$$

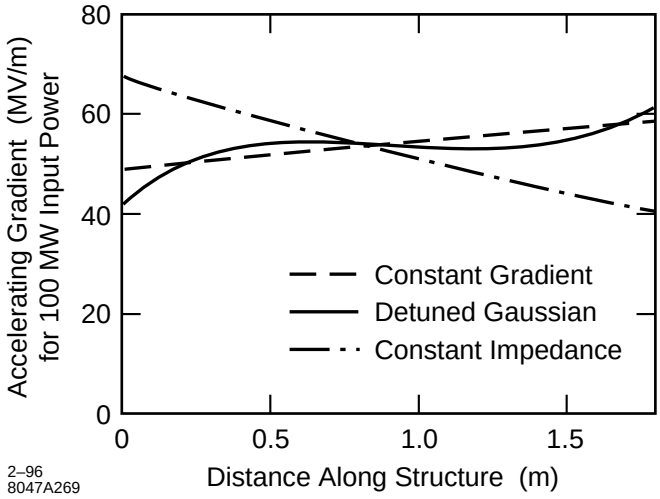

Figure 8-3. *Accelerating electric field gradient along the axis of detuned structure. Electric field gradients for conventional constant-impedance and "constant-gradient" structures with the same input power and attenuation are also shown for comparison.*

where $s = \omega(r/Q)$ is the local elastance per unit length. Using Floquet's theorem with Equation 8.9, we get

$$G_0(n+1) = \left[\frac{\alpha(n+1)r(n+1)}{\alpha(n)r(n)}\right]^{1/2} e^{-\alpha(n)d} G_0(n) \quad . \tag{8.11}$$

Here $d = L_s/N$ is the cell length, where N is the total number of cells in a structure of length L_s. The gradient in the first cell is $G_0(1) = [2\alpha(1)r(1)P_0]^{1/2}$, where P_0 is the steady-state input power. The distance, attenuation, filling time and voltage from the input to the end of the nth cell are

$$z(n) = nd \tag{8.12}$$

$$\tau(n) = d\sum_{i=1}^{n} \alpha_i \tag{8.13}$$

$$T_f(n) = d\sum_{i=1}^{n} 1/v_{gi} \tag{8.14}$$

$$V(n) = d\sum_{i=1}^{n} G_i \quad . \tag{8.15}$$

We assume that the structure is operated synchronously (no cell-to-cell phase error for a velocity-of-light electron), although the analysis can easily be extended to the nonsynchronous case.

The gradient induced by a charge Δq passing through the nth cell is $\Delta G_b(n) = s(n)\Delta q/2$. Using $\Delta q = I_0 d/v_g(n)$ and Equation 8.10, the gradient induced during the time it takes for the accelerating wave to pass through the cell is

$$\Delta G_b(n) = \alpha(n)r(n)I_0 d \quad , \tag{8.16}$$

where I_0 is the steady-state beam current. The beam-induced gradient in the first cell is $G_b(1) = \alpha(1)r(1)I_0 d$. The net beam-loading gradient in the nth cell is the sum of $\Delta G_b(n)$ and a term due to power flow from the gradient induced

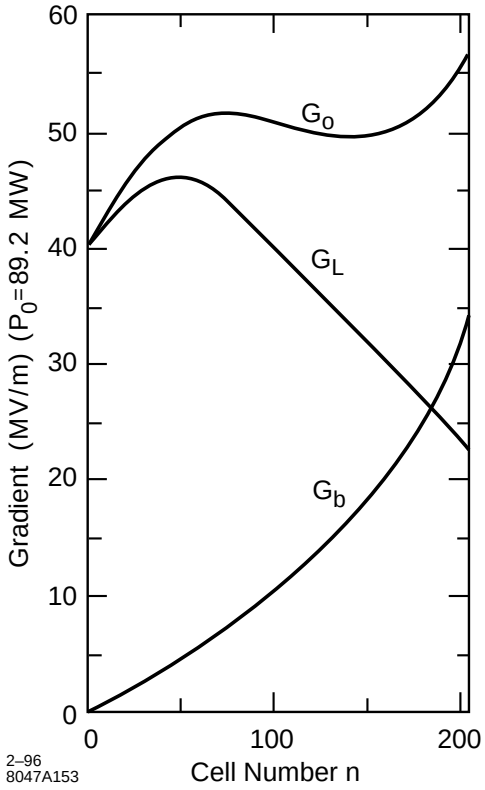

Figure 8-4. *Generator (G_0), beam (G_b), and loaded (G_L) gradients as a function of cell number n.*

in upstream cells. In analogy with Equation 8.11, the gradient in cell $n+1$ in terms of the gradient in cell n is then

$$G_b(n+1) = \left[\frac{\alpha(n+1)r(n+1)}{\alpha(n)r(n)}\right]^{1/2} e^{-\alpha(n)L_c}G(n) + \alpha(n)r(n)I_0 d \quad . \tag{8.17}$$

The net beam-loaded gradient in the nth cell is

$$G_L(n) = G_0(n) - G_b(n) \quad . \tag{8.18}$$

The functions G_0, G_b and G_L are plotted in Figure 8-4 for an average unloaded gradient $\bar{G}_0 = V_0(N)/L_s$ = 50 MV/m. It is assumed that the presence of a damping manifold results in a 3% reduction in Q. The required input power is 89.2 MW per structure (50 MW/m). The average beam-loading gradient is 14.7 MV/m for a charge per bunch of 7.5×10^9 electrons, giving a net loaded gradient of 35.3 MV/m. The beam-loading derivative is 17.13 MV/A. Further details are given in NLC Technical Notes [Farkas 1994, Farkas 1995].

Transient Beam-Loading Compensation

To compensate for transient beam loading, it is necessary to produce the steady-state beam loaded gradient profile, $G_L(n)$, by varying the generator power flow during one filling time prior to beam turn-on at time $t = 0$. This compensation is tantamount to "pre-loading" the structure. Taking into account the attenuation and propagation time

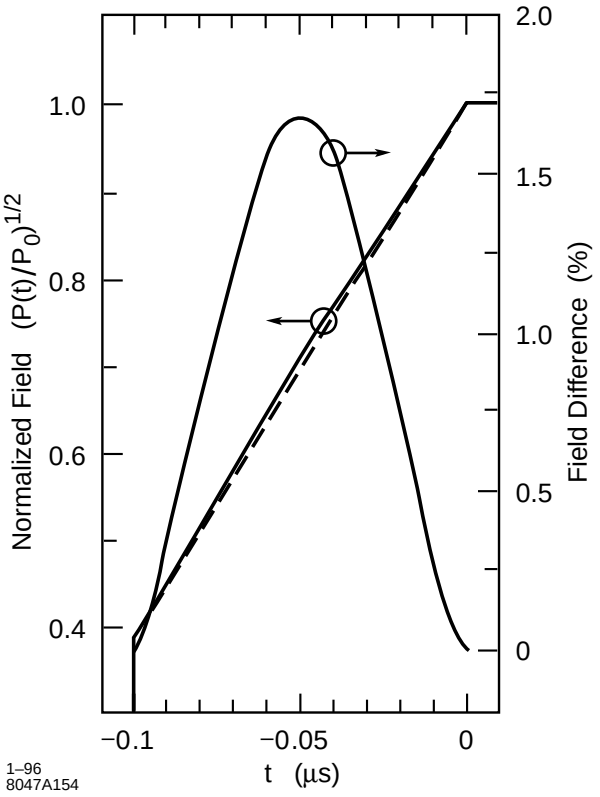

Figure 8-5. *Normalized input field $[P(t)/P_0]^{1/2}$ and the difference between it and a linearly-ramped field (dashes), vs. time. (The initial normalized input field is 0.385.)*

from the input cell to cell n, and the relation between power flow and gradient as given by Eq. 8.9, the required ramping profile is

$$P\left[-T_f(n)\right] = \frac{{G_L}^2(n)e^{2\tau(n)}}{2\alpha(n)r(n)} \quad . \tag{8.19}$$

where $T_f(n)$ and $\tau(n)$ are given by Eqs. 8.13 and 8.14.

The normalized field ramp $[P(t)/P_0]^{1/2}$ is plotted in Figure 8-5. For a true constant-gradient structure, this field ramp would be exactly linear. A linear ramp is also plotted in Figure 8-5 for comparison, along with the relative field difference on an expanded scale. The relative deviation from a linear ramp reaches about 1.5% (3% in power) at $t \approx -0.5T_f$. Use of a linear ramp instead of the exact compensation profile would result in an energy variation of about 1% along the bunch train.

8.2.4 Mechanical Design of the Accelerator Structure

This section gives a general description of the mechanical design of the damped and detuned structure (DDS). The discussion covers the design and tolerances of the cells, vacuum pumping and water cooling systems, the input coupler, and the supporting strongback. Stack assembly for diffusion bonding is described. Starting with the unavoidable geometrical complexity which is mandated by the theoretical specifications, an attempt has been made to keep the rest

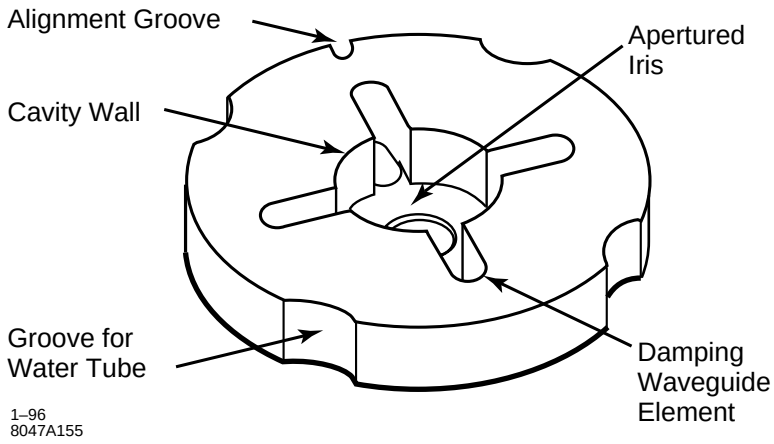

Figure 8-6. *Basic cell design.*

of the design as simple as possible to minimize costs and to facilitate automation of the production of the very large quantities of components required.

Cell Design

The basic features of the cell are shown in Figure 8-6. The central portion is the conventional "cup" consisting of a cylindrical cavity wall and an apertured iris which, when stacked in a row with other cells, forms the disk-loaded waveguide accelerator structure. The diameter of the cavity wall, the thickness of the iris, and the diameter of its aperture vary progressively from cell to cell to "detune" the beam-deflecting dipole modes and suppress short-range cumulative build-up of wakefields, while maintaining the quasi-constant-gradient characteristics of the fundamental accelerating mode. The central cavity is slot-coupled to four outer rectangular holes. When the cells are stacked, the holes form four waveguides which run parallel to the axis of the structure. When terminated in matched loads, the four waveguides become "damping manifolds." The slots (which are cut off for the fundamental accelerating mode) couple power from beam-excited dipole modes into these damping manifolds, lowering the Q and suppressing long-range wakefield build-up. Microwave signals from the damping manifolds can be used to monitor the alignment of the structure with respect to the beam.

The waveguide height and its distance from the structure axis vary progressively from cell to cell, as described in Section 8.2.1. Thus, for example, cells 10, 70, 122 and 196 appear as shown in Figure 8-7. All cells have the same thickness.

The cells have four circular-sector grooves equispaced around their periphery to accommodate four water-cooling tubes which are attached in a final brazing operation. The partially inset tubes provide adequate thermal conductance while avoiding direct water-to-vacuum diffusion bond interfaces. Since there are 205 cells in each accelerator section, forming the water channels by lining up four holes drilled through each cell would have resulted in over 800 such bonds in each section, greatly increasing the probability of failure due to leakage.

Each cell has an additional groove which is used to determine rotational alignment during assembly.

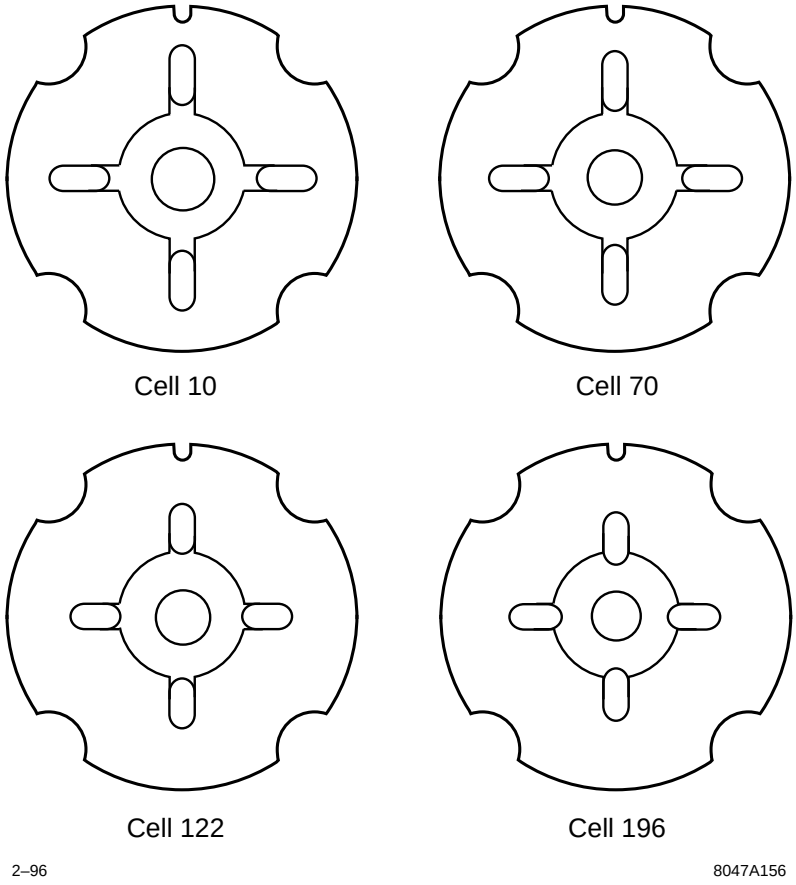

Figure 8-7. *Front view of typical cells.*

Cell Tolerances

The goal is an accelerator section 205 cells long (plus the input coupler) in which the axes of the individual cavities lie on a straight line to within 15 μm (rms).

To avoid a cumulative tolerance build-up which exceeds this goal, many other cell dimensions have to be held to tolerances in the 2 to 3 μm range. This applies particularly to the diameter and coaxiality of the outer surface of the cell, since this has to be the reference surface used in stacking the cells prior to bonding. It also applies to the perpendicularity, flatness and parallelism of the cell faces. Errors here will cause "bookshelving" [Seeman 1985] in the cell stack. Equally important is the coaxiality of the iris aperture with respect to the cavity outer wall.

These tight tolerances on cavity dimensions (including the thickness of the iris and the radius of its edge) are also necessary to achieve the design fundamental and dipole-mode frequency characteristics, because provision for tuning after assembly has been eliminated.

Flatness of cell faces is also essential to achieve diffusion bonding (discussed below) over relatively large surface areas with a very low expected failure rate.

	Detuned 1.8-m Section #1	Detuned 0.9-m Sections #1 & 2	Detuned 1.8-m Section #2 and DDS #1
Machining Technique	Conventional	Conventional	Diamond-point
Alignment Technique	Nesting	Vee-Block	Vee-Block
Diameters	± 7	± 7	± 2
Concentricity	10	10	1
Thickness	± 7	± 7	± 2
Parallelism	10	10	0.5
Flatness	10	10	0.5
Surface Finish	0.4	0.4	0.05
Cell-to-cell Alignment of Outer Cylindrical Surfaces:			
(a) Expected	22	10	3
(b) Measured after diffusion bonding or brazing	10	6	4

Table 8-4. *Cell machining and assembly tolerances achieved (in microns).*

Single-crystal diamond-point machining is to be used on all surfaces of each cavity, the cell faces and outer periphery. The hardness, high thermal conductivity, and low thermal expansion of diamond result in a superior tool which, when used in a vibration-free lathe, yield mirror-like surfaces on copper which have a roughness of 0.1 μm or less. This finish is necessary to obtain good diffusion bonding, high Q factors, low dark current and high power-handling capability. The sharpness, mechanical stability, and minimal wear of the tool allow the dimensional tolerances to be met.

Surface finish and dimensional tolerances are less stringent for the side-coupled holes which form the damping waveguides. Respectively, 0.5 μm and ± 20 μm are sufficient. The surface finish in the grooves for the water tubes can be 1 μm.

Table 8-4 illustrates what tolerances on dimensions and alignment have been achieved to date at SLAC, and what can reasonably be expected with the best technology available today. It can be seen that the most significant advances have been made by resorting to diamond-point machining and by using precision granite vee-blocks to align the stacks of cells prior to brazing or diffusion bonding. Cells designed to nest into each other have to fit loosely enough to permit assembly without galling, and this can result in unacceptable misalignment.

Our present experience is that stacks of 38 cells can have a bow of a few tens of microns after diffusion bonding. This can be reduced to a few microns by setting the stack horizontally in cradles on a granite block and applying bending forces while monitoring movement with a precision coordinate measuring machine.

Vacuum Pumping

In addition to direct pumping along the beam-interaction region, the structure is pumped in parallel by the four damping waveguides. Assuming a residual outgassing rate of 10^{-12} Torr-ℓ/cm^2/s for the copper surfaces, the combined conductance of this system is high enough to reduce the pressure to approximately 10^{-8} Torr in the middle of the structure when pumps are connected only at each end. Since lower pressure may be required, two groups of four special pumping cells will be inserted into the structure, at points one-fourth of the section length from each end. Each pumping cell has high-conductance slots cut in the middle of the broad walls of the damping waveguides. These slots, which are cut off to the fundamental accelerating mode, connect to four ducts and two pumping manifolds and pumps,

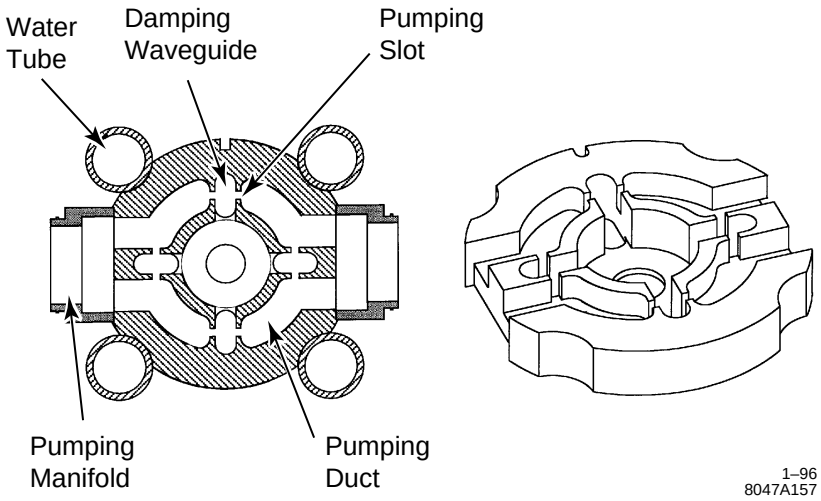

Figure 8-8. *Cross section and isometric view of pumping cell.*

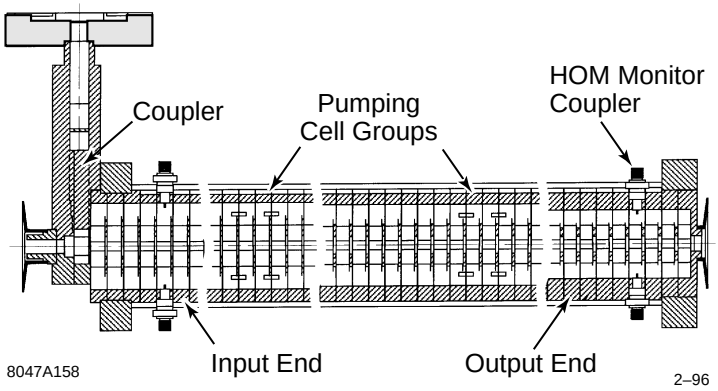

Figure 8-9. *Longitudinal cross section of accelerator section.*

as shown in Figure 8-8. By pumping only at the two quarter-points, the maximum pressure will be four times less than when pumping only at the end points (and 20 times less than when pumping from the ends of the beam-interaction region in the absence of any manifolds).

A longitudinal cross section of the accelerator section is shown in Figure 8-9. Each pumping cell group is connected to two pumps via short transverse manifolds. Each of these contains two short bellows sections to allow for a small range of accelerator movement in the vertical plane with the two pumps rigidly attached to the strongback (accelerator support beam). The horizontally opposed system ensures that there is no net transverse force on the accelerator due to atmospheric pressure.

The Input Coupler

Some details of the input coupler are shown in Figure 8-10. The coupler is a compact version of the symmetrical coupler used on the first 1.8-m sections for the NLCTA. The input cavity has double symmetrical matching irises in

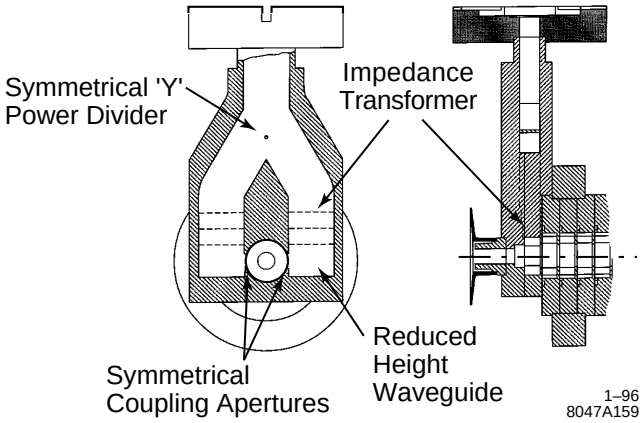

Figure 8-10. *Symmetrical input coupler.*

the horizontal plane which couple into the *sides* of two WR-90 low-impedance waveguides (instead of the ends, as used in the NLCTA design).

The waveguides are matched into standard WR-90 by step transformers, after which they combine into a common feed guide by means of a symmetrical post-matched "Y" power divider. This compact design can be machined in two blocks of copper and brazed together, ensuring electrical symmetry and minimum insertion loss.

Figure 8-9 shows no output coupler. The intention is to provide internal matched terminations for both the fundamental accelerating mode and the wakefield modes by depositing lossy coatings on the walls of the cavities and the damping manifolds in the last four cells. A coaxial loop loosely coupled to the last cavity will be used to monitor the fundamental-mode power. This signal will pass through a coaxial rf window in the cell wall, and will be used by the klystron phasing system. However, if satisfactory internal terminations cannot be developed, external loads and couplers will have to be used.

Water Cooling

After the stack of cells has been assembled by diffusion bonding, four water-cooling tubes are brazed into the grooves which are shown in Figures 8-6, 8-7, and 8-8. At each end of the section, the tubes connect to circular manifolds which provide additional conduction cooling of the input coupler and the lossy termination cavities at the output end. The direction of flow alternates from tube to tube.

Strongback Design

The standard strongback supports two 1.8-m accelerator sections. It is a 15-cm $\times$ 10-cm, aluminum box beam with a 6-mm wall. The input coupler of the first accelerator section is rigidly attached to the strongback. All other supports are flexible. Four supports are situated under the pumping cell regions of the two sections. In addition, there are supports under the middle of each section and under the input coupler and the output end of the second section. The latter is fixed in height, but all other flexible supports have adjustment mechanisms which can set the height to a few microns. These are intended only to compensate for residual elastic bowing of the accelerator-and-strongback assembly due to gravity. Any straightening of the sections which requires bending them beyond their elastic limit must be done before attaching them to the strongback.

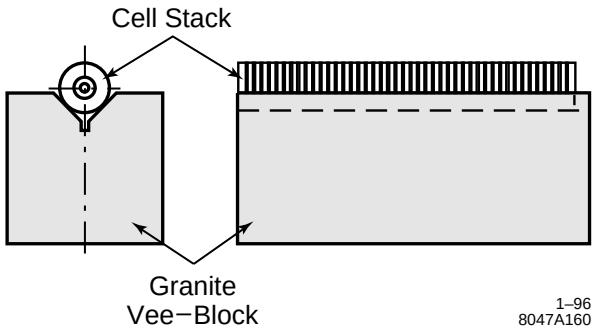

Figure 8-11. *Schematic of cell assembly on vee-block.*

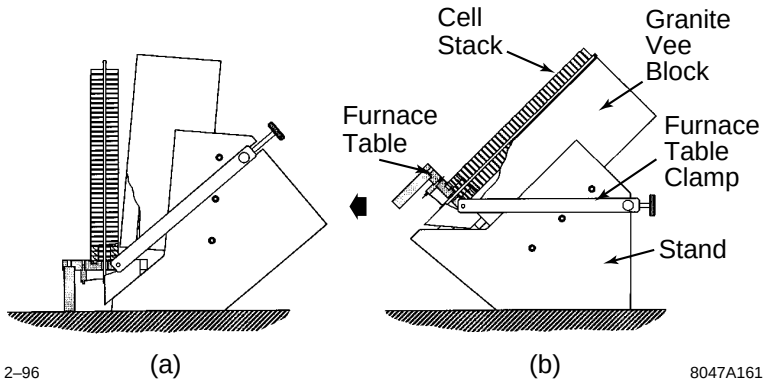

Figure 8-12. *Cells stacked on table in vee-block.*

The flexible supports are, of course, necessary to allow for differential expansion between accelerator and strongback. As presently designed, the bending radius of the flexible arm is approximately 48 mm. Thus, if the temperature of the two accelerator sections is allowed to rise 20°C above the strongback temperature, the free end will expand about 1.5 mm, which results in the accelerator axis drooping by 23 μm. An adequate solution to this problem is to maintain the strongbacks at close to the same temperature as the accelerator sections by using the same water supply in series to control their temperatures. The temperature match between accelerator and strongback does not need to be very close. Even a 5°C average difference results in a drop at the free-end of only 1 μm.

For a discussion of distortions due to transverse thermal gradients across the strongback (girder) itself, see Section 7.9.1.

Assembly: Diffusion Bonding and Brazing

The cells are presently aligned in stacks by placing them in a precision granite vee-block, as shown schematically in Figure 8-11. Actually, the cells rest on a table (Figure 8-12) which is held against the end of the block. A tension frame presses the cells against the table, so that they retain their precise alignment as the stack and table are moved away from the vee-block and transferred to the furnace.

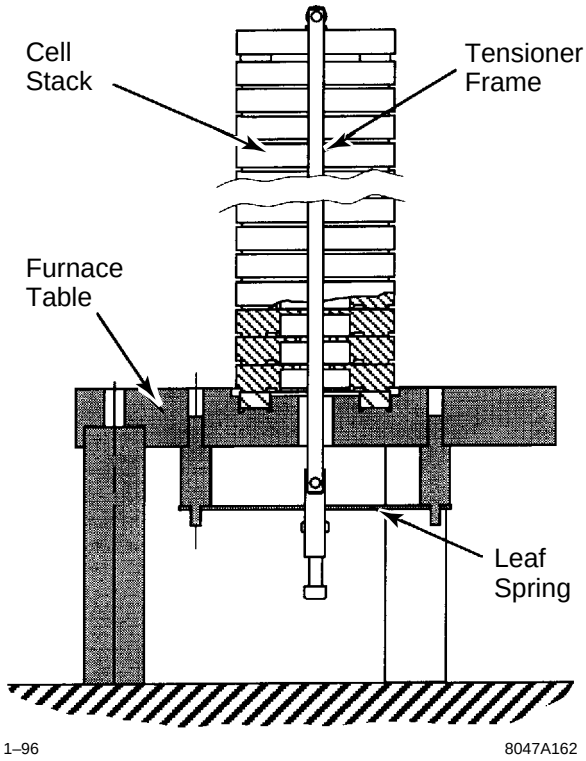

Figure 8-13. *Cells stacked for diffusion bonding.*

The cells, pressed together by the tension frame as shown in Figure 8-13, are diffusion-bonded together by heating to 1000°C in hydrogen. The number of cells bonded into a stack at one time is to be determined. Long stacks reduce the number of assembly steps but increase the difficulty of handling.

The coupler, drift tubes, and vacuum and water manifolds are added in a final furnace cycle, using a copper/gold braze. Coupling tubes are also added in two special manifold cells (one near each end of the section), into which coaxial feedthroughs (Figure 8-14) can be welded for monitoring dipole mode-induced fields in the lossy waveguides.

Leak Checking and Straightening

After the final braze, the coaxial feedthroughs are welded in. The completed section is leak-checked and then attached to a special straightening strongback. Each assembly, at present, is then transferred to a coordinate measuring machine, where the alignment of every cell is checked (with the section still hanging vertically to eliminate bending due to gravity). Corrective bending is done at intervals along the section by applying transverse forces from adjustable micrometer jacks built into the special strongback. Two sets of jacks allow bending corrections to be made in two orthogonal planes through the axis of the section.

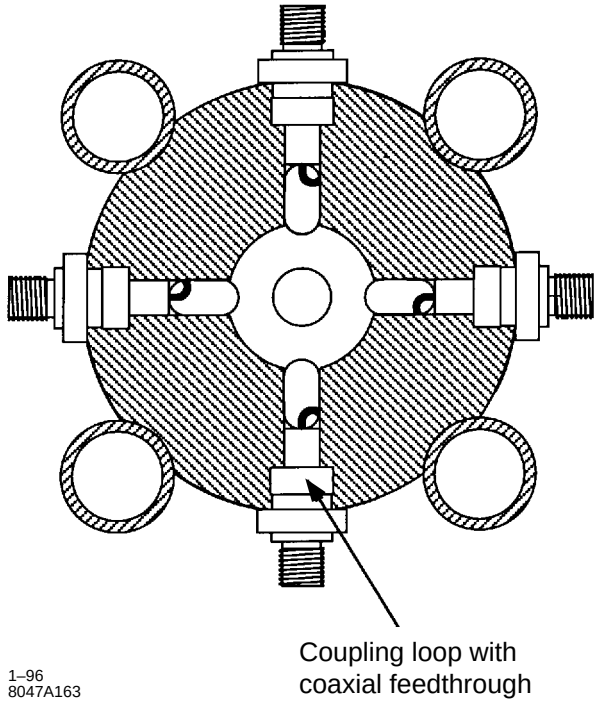

Figure 8-14. *Wakefield monitoring cell.*

Cold Testing

After straightening, the section is moved to a cold-testing station where network analyzer measurements are made to determine the input match and the phase advance per cell of the fundamental mode. The measurements are made and recorded rapidly and largely automatically (possibly by dropping a reflecting bead along the beam axis from output to input). A second set of measurements is made in the frequency band of the dipole modes, using the coaxial feeds to check the transmission characteristics from one damping waveguide across the cavities to the opposite damping waveguide. All these tests result in a simple "accept" or "reject" decision for the section, as no provision for tuning or other adjustment is made.

Bakeout

Still hanging vertically, the section is removed from the special strongback and transferred to a bake station. The section is evacuated and baked at about 500°C (in a vacuum oven) until the internal vacuum stabilizes in the low 10^{-8}-Torr region. After cooling, the section is back-filled with filtered, purified, nitrogen gas, and attached, with a second section, to a standard double-length strongback on which it will be installed in the NLC machine. The double-section assembly is shown in Figure 8-15.

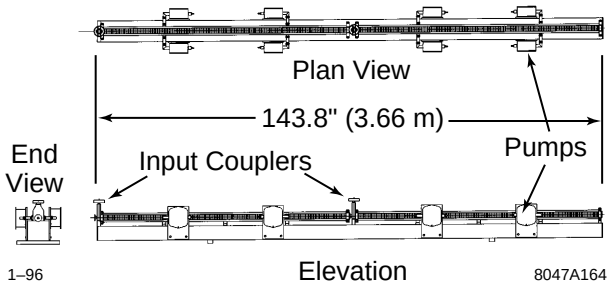

Figure 8-15. *Two NLC accelerator sections mounted on a strongback.*

Large Quantity Production of Accelerator Cells

The two main linacs will contain about 1.5 million cells, which have to be produced in about three years. Assuming that a specialized plant set up to fabricate the cells operates 50 weeks per year at two shifts per day, then, at 80% efficiency, a production rate of about 2.6 cells per minute is required. A close estimate of the time taken to machine a single cell cannot be made without reference to specific machines and machining techniques. (See, for example, the study reports prepared for the CERN CLIC cells [Read 1993] [OWGR 1993].) However, very rough estimates may be drawn from those reports, noting that the surface area of the X-band DDS cell is about three times that of the CLIC cell. All the features of the DDS cell shown in Figure 8-6 could be machined to conventional tolerances on the end of bar stock (leaving excess material on the critical surfaces to be diamond-point machined in subsequent operations), using a multipurpose CNC turning and milling machine. The cell could thus be cut from the bar using a parting-off tool, stress-relieved and delivered to a diamond-point lathe for finishing in two steps. In the first step, the cell could be gripped on the outside by a precision chuck while the back face is diamond turned. In the second step, the back face could be held in a vacuum chuck while the front face and cavity surfaces are diamond finished. Estimated operation times are: 1.5 min for conventional turning, 7 min for milling, 1 min for first-cut diamond-point turning, and 2 min for second-cut diamond-point turning. These machining times indicate that the plant will need a minimum of 22 conventional CNC turning and milling machines and 8 diamond-point lathes, with appropriate numbers of all supporting equipment (automatic handling and transfer machines, stress-relieving ovens, cleaning, QC, and packing stations) to maintain the required throughput.

8.2.5 Thermal Calculations

The thermal expansion of accelerator sections under high gradient with or without beam loading must be considered. A finite element analysis code is used to calculate the structure distortions. To maintain stabilized beam phase, a control loop is needed for adjustment of cooling water temperature.

Thermal expansion of accelerator sections under high gradient induces phase shifts with respect to the beam, and therefore detracts from beam energy stability. The heat dissipation in accelerator sections varies with the degree of beam loading and must be automatically compensated by controlling the inlet low conductivity water (LCW) temperature.

The thermal effects for the NLC accelerator sections have been calculated under the following conditions. Onto each 1.8-m-long accelerator section are brazed four cooling pipes of $0.325''$ inner radius, which are made of oxygen-free high-conductivity (OFHC) copper, aligned along the length of the structure, and spaced azimuthally 90° apart. The pipes are connected in a counterflow pattern such that one pair of 180°-separated pipes carries water from one end of

	0.5 TeV		1.0 TeV	
	Peak power/section 90 MW Total pulse length 240 ns Repetition rate 180 Hz		Peak power/section 261 MW Total pulse length 240 ns Repetition rate 120 Hz	
	No Beam	Peak Beam Curr. 0.86 A	No Beam	Peak Beam Curr. 1.26 A
Avg. dissipated power/section (kW)	2.88	2.17	5.56	4.39
Avg. temp. rise of structure ($^\circ$C)	2.03	1.55	3.93	3.10
Integrated phase shift per section ($^\circ$)	14.2	10.9	27.5	21.7

Table 8-5. *Thermal effects in 1.8-m-long X-band accelerator sections.*

the structure and the other pair carries water from the other end of the structure. The total flow rate is 16 gallons per minute. The average copper temperature is 45°.

The cooling water for the accelerator structure is provided from a manifold which supplies water to a large number of accelerator sections. The manifold will be supplied with water regulated to better than 0.1°C using a three-way mixing valve. Water flow to individual sections will be controlled using either manually adjustable control valves with optical flow meters, or flow-limiting orifices. This level of thermal control has been maintained, in the absence of varying rf power levels, for the S-band accelerator sections of the SLC at SLAC. For the NLC, the average rf power dissipated by the accelerator structure will be kept constant by combining, in phase quadrature, the power from pairs of klystrons.

In the calculation of rf power dissipation, the rf pulse in the first 100 ns is modulated to create a quasi-linearly ramped accelerating field profile at the input end of the accelerator section. The heating contribution of rf power due to the intrinsic efficiency of the SLED-II is also included. The average temperature increase of the copper structure is considered to be the average bulk water temperature change plus average film temperature drop. Table 8-5 shows the average temperature increase and corresponding integrated phase change per section for the 0.5-TeV and 1-TeV center-of-mass cases, with and without beam loading.

A finite element analysis code was used to calculate the structure distortions. The maximum asymmetry in distortion at the ends of an accelerator section is negligible (less than 0.4 μm in cavity diameter). This will not introduce excitation of higher-order dipole modes.

8.2.6 High-power Tests and Dark Current Studies

The theoretical and experimental studies on the behavior of copper accelerator structures under extremely high-rf fields have been carried out at SLAC for several years [Loew 1988a, Wang 1994a]. We have studied in considerable detail the problems of rf breakdown and dark current generated by field emission at high gradient. The dark current

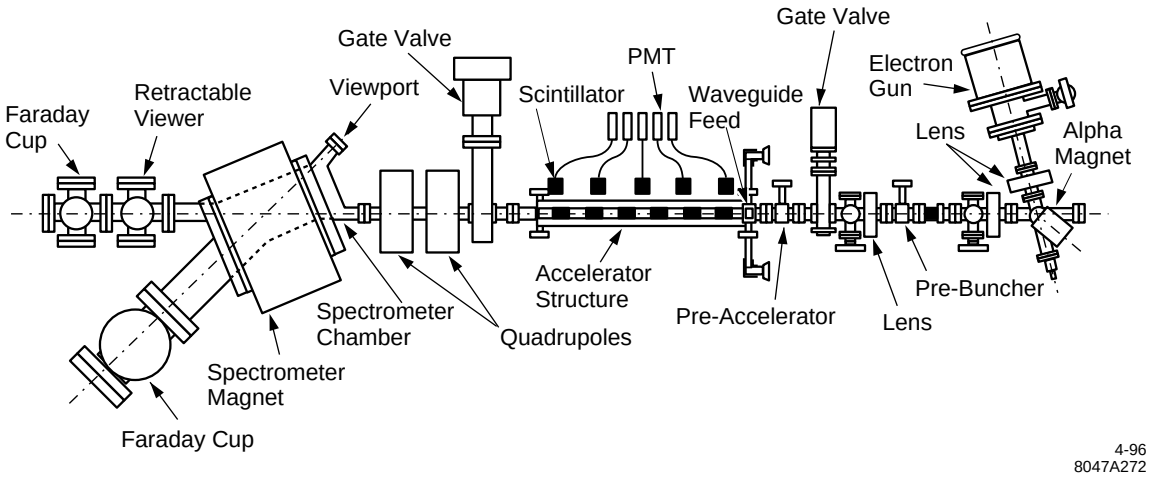

Figure 8-16. *Schematic of Accelerator Structure Test Area (ASTA).*

may absorb rf energy, get captured, and produce undesirable steering effects and detrimental x-ray radiation. Many experiments have been done to measure the amplitude and energy spectrum of the dark current and to study phenomena related to rf breakdown such as outgassing, radiation, heating, etc. We have concluded that the dark current can be minimized by improving surface finish and cleanliness, and by rf processing.

The structures which have been examined at X-band are a 6-cm standing-wave (SW) section and a 26-cm constant-impedance traveling-wave (TW) section, a 75-cm constant-impedance TW section, and a 1.8-m TW section. All of the structures were tested in the Accelerator Structure Test Area (ASTA) facility located in a shielded area. As shown in Figure 8-16, ASTA consists of a gun and beam focusing system, a prebuncher, a preaccelerator, a precision rail for mounting the accelerator sections to be tested, and a 45° spectrometer capable of analyzing electron beam energies up to 200 MeV with a resolution of $\pm 0.5\%$. Four directional couplers at input and output ports of the accelerator sections are used to pick up forward and reflected rf signals. Five collimated scintillators alongside the accelerator sections monitor localized radiation and breakdown. The accelerator structures are powered by a SLAC X-band klystron followed by a SLED-II pulse compression system.

The characteristics, main rf parameters of those structures, and high-power test results are listed in Table 8-6. The high-power tests with an electron beam have demonstrated that the 1.8-m section is properly tuned to 11.424 GHz and can accelerate a beam at a gradient of more than 67 MV/m.

Figure 8-17 shows the dark current measured in a Faraday cup as a function of average accelerating field for the 75-m constant-impedance structure and the 1.8-m detuned structure. The dark current for an accelerating gradient of 50 MV/m was found to be negligible. At 85 MV/m, it was estimated to be tolerable. The energy spectrum of the dark current was measured and found to be sufficiently low that the quadrupoles will overfocus and sweep the field-emission beam away from the primary, high-energy beam.

8.2.7 Material Handling and Processing Techniques

Experiments performed with S-band accelerators at KEK [Takeda 1991, Matsumoto 1991] have shown that the dark current produced by field emission from the accelerator disks is reduced by an order of magnitude when stringent precautions are taken to exclude dust during fabrication, assembly, processing and testing. These experiments indicate

Parameter	6 cm (SW)	26 cm (TW)	75 cm (TW)	1.8 m (TW)
Frequency, f (MHz)	11424	11424	11424	11424
Structure type	C.I.	C.I.	C.I.	Detuned
Iris diameter, $2a$ (cm)	0.75	0.75	0.856	1.134–0.786
Cavity diameter, $2b$ (cm)	2.12	2.12	2.158	2.284–2.139
Disk thickness, t (cm)	0.146	0.146	0.146	0.1–0.2
Total # of cavities	7	30	86	206
Shunt impedance (MΩ/m)	98/2	98	88	67–88
Figure of merit, Q	6960	6960	7005	7020
Coupler type	Single	Double	Double	Double
Group velocity, v_g/c	–	0.033	0.048	0.118–0.03
Filling time, T_f (ns)	80	26.5	52	100
Attenuation, τ	–	0.136	0.267	0.505
Rf pulse length (ns)	770	60	75	150
Peak input power (MW)	13.8	116	130	160
Maximum $E_{\rm acc}$ (MV/m)	–	108[b]	90 [b]	70[b]
Average $E_{\rm acc}$ (MV/ m)	110[a]	101[b]	79[b]	67[b]
Maximum surface field, E_s (MV/m)	500[a]	235[b]	206[b]	180[b]
Ratio $E_s/E_{\rm acc}$	4.55	2.275	2.292	2.37[c]

[a] Limited by rf breakdown

[b] Limited by klystron output power

[c] Ratio $E_s/\bar{E}_{\rm acc}$

Table 8-6. *Characteristics of tested structures*

that the NLC accelerator cells should be cleaned in ultra-pure, dust-free chemical solutions and rinses, assembled and bonded under clean-room conditions, and perhaps given a final rinse in ultra-pure water before vacuum bakeout and installation.

8.2.8 Multibunch Energy Spread and Compensation

Multibunch energy spread and the scheme for multibunch energy compensation were discussed in Section 7.4.5 and in Section 8.2.3: "Transient Beam-Loading Compensation". As noted in those sections, transient beam loading for both regular accelerator sections (quasi-constant gradient structures) and injector sections (over-compensated quasi-constant gradient structures) can be compensated by using a specially-modulated rf pulse, so that the rf electrical field envelope at the input end is ramped quasi-linearly during one filling time before the injection of a bunch train.

Here we summarize the tolerances (on rf phase and amplitude ripple) that come from the effect of the ripple on multi-bunch energy and energy spread. As noted in Chapter 7, the effect of dispersion of different frequency components in the rf pulse needs to be taken into account, and we have treated each bunch as a single macroparticle (*i.e.*, intrabunch energy spread is ignored in these calculations). Also, the calculations presented here do not take into account the averaging of the ripple over different rf sections, which loosens the tolerances by approximately $\sqrt{N}$ where N is the number of sections over which we average. (We expect N to be approximately the number of rf sections between linac diagnostic stations, unless there are effects that cause the ripple to be correlated over different stations.)

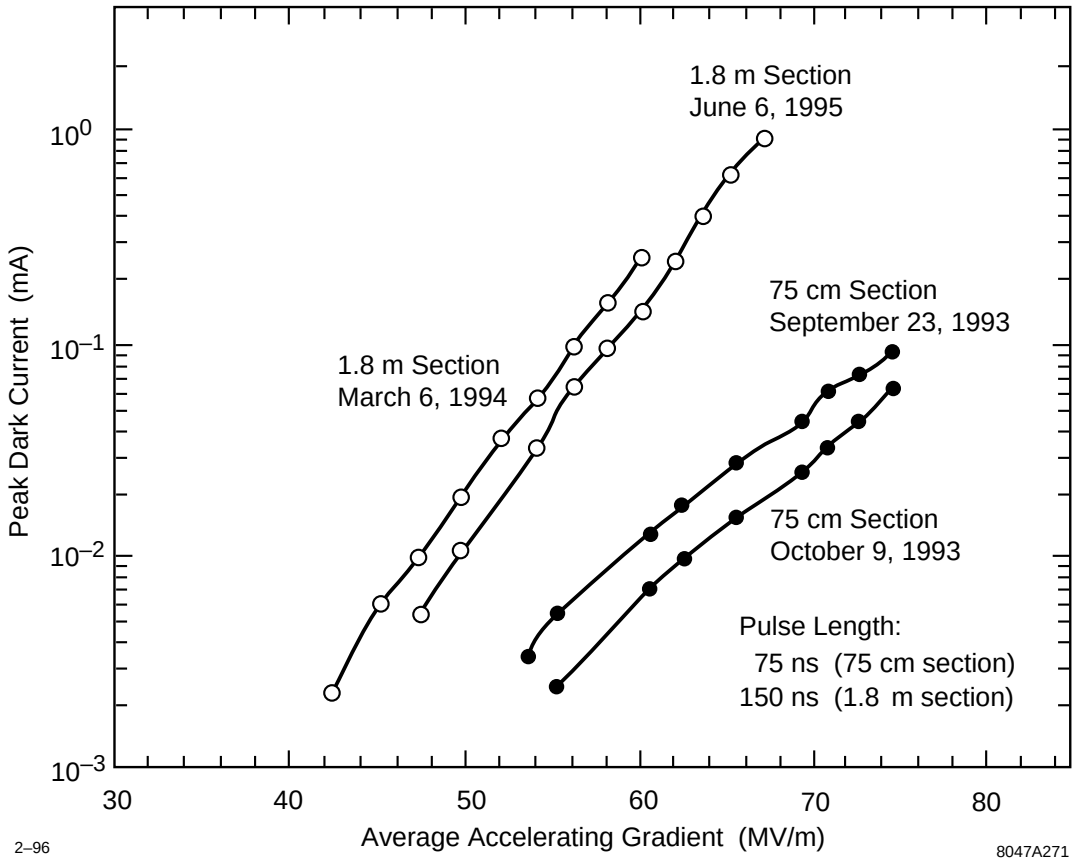

Figure 8-17. *Dark current as a function of average accelerating field for the 75-cm constant-impedance structure and 1.8-m detuned structure.*

RF Phase Variations

We considered the effect of rf phase ripple superimposed on the incoming 11.424-GHz rf pulse in the preceding chapter, where we assumed that the ripple is a cosine wave with a given period (in nanoseconds) and amplitude (in degrees at the rf frequency). For convenience, we summarize here the resulting tolerance on phase ripple as a function of ripple time scale, in order to meet given energy and energy spread tolerances on the beam pulse, consisting of a train of 90 point-like bunches. Here the tolerances on the multibunch energy spread and on the variation in the average energy of the beam have both been taken to be about $\Delta E/E \sim 10^{-3}$.

We take the tolerance on the rms fractional bunch-to-bunch energy spread to be 0.1%. As noted above, we ignore the contribution from the intrabunch spread, which would add about another 0.1% to the spread. We also take the tolerance on the energy centroid shift to be $\pm 0.1\%$. Figure 8-18 (a) shows the approximate tolerance on the rf phase ripple as a function of the period of the ripple, to meet the tolerance on the rms energy spread. Figure 8-18 (b) shows the approximate tolerance on the rf phase ripple as a function of the period of the ripple, to meet the tolerance on the centroid energy shift. The tolerances in the middle of the range of ripple timescales are approximate since they are somewhat dependent on the phase of the ripple with respect to the beam; we have recorded the most conservative values obtained in simulations.

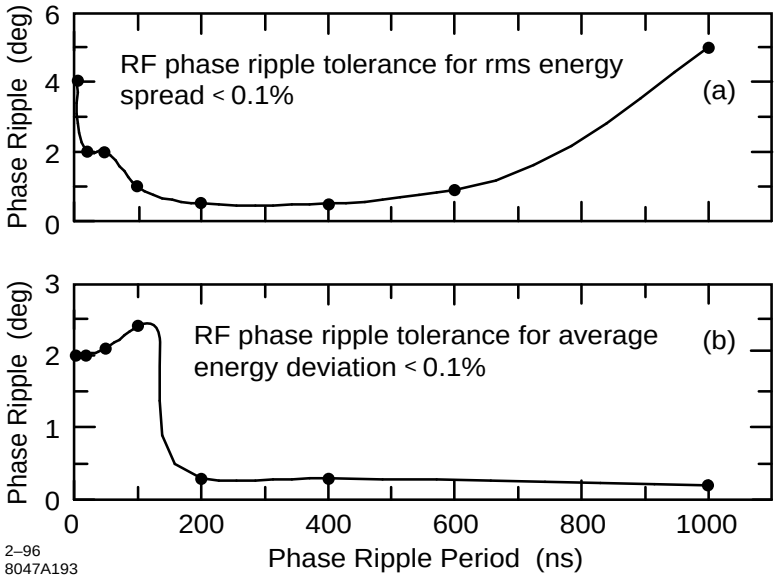

Figure 8-18. *(a) Tolerance on the rf phase ripple as a function of the period of the ripple, to meet a tolerance of 0.1% on the rms energy spread. (b) Tolerance on the rf phase ripple as a function of the period of the ripple, to meet a tolerance of 0.1% on the centroid energy shift.*

RF Field-Amplitude Variations

In Chapter 7 we also considered the effect of ripple in the amplitude of the incoming rf pulse, supposing that the ripple is a cosine wave with given period (in nanoseconds) and amplitude (in megavolts).

Figure 8-19 (a) shows the approximate tolerance on the rf field-amplitude ripple as a function of the period of the ripple, to meet the 0.1% tolerance on the rms energy spread. Figure 8-19 (b) shows the approximate tolerance on the rf field-amplitude ripple as a function of the period of the ripple, to meet the $\pm 0.1\%$ tolerance on the centroid energy shift. Again these are rough estimates, especially in the middle of the range of ripple time scales, since they are somewhat dependent on the phase of the ripple with respect to the beam.

8.2.9 NLC Test Accelerator Experiments

The goal of the NLCTA experimental program is to measure the performance characteristics of the multi-section X-band linac and high-power rf systems. The experiments will go beyond the work with single power sources and structures at the Accelerator Structure Test Area (ASTA) in the Klystron Test Laboratory; the NLCTA beam will be much more intense, will be much better defined, and will be more precisely analyzed, both before and after acceleration. In addition to system operations tests, beam-dynamics studies will be done using three types of bunch trains: a short bunch train of a few nanoseconds will be used to measure the unloaded energy-gain characteristics of the linac, a variable-length bunch train will be used to measure field-emission currents in the linac with and without injected beam, and the nominal 125-ns-long bunch train will be used to test multibunch beam-loading compensation. The specifics of these experiments are discussed in the following sections, concluded by a discussion of other types of wakefield studies that will be made possible by upgrading the NLCTA injector. An important part of the NLCTA experimental program, of great relevance for the NLC, is the commissioning of the multibunch beam instrumentation.

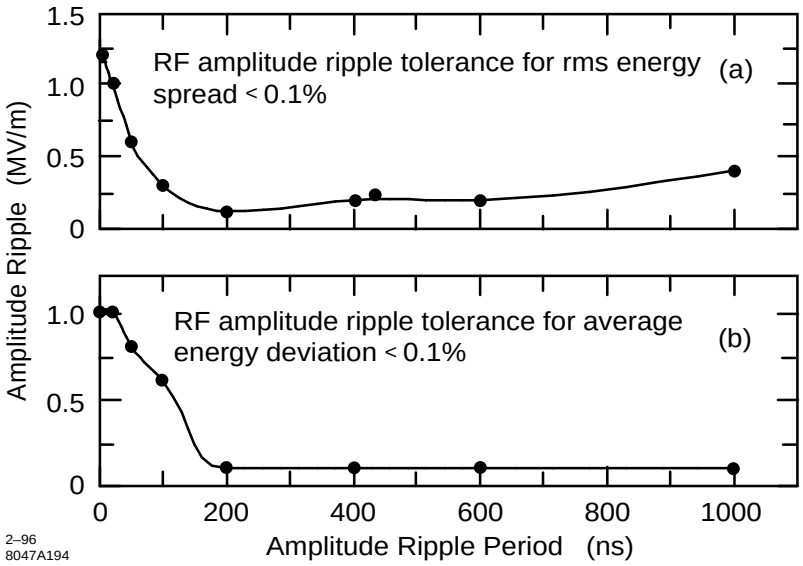

Figure 8-19. *(a) Tolerance on the rf field-amplitude ripple as a function of the period of the ripple, to meet tolerance of 0.1% on the rms energy spread. (b) Tolerance on the rf field-amplitude ripple as a function of the period of the ripple, to meet tolerance of 0.1% on the centroid energy shift.*

System Studies

The NLCTA rf system was designed to be large enough in scale, with four klystrons powering eight structures through SLED-II rf pulse compressors, that it will serve to test system control and monitoring methods applicable to NLC-scale linacs. A key component of the monitoring system will be instrumentation that can detect and digitize the phase and amplitude envelopes of the 250-ns-long rf pulses. This waveform system, which will be based on commercially available high-speed waveform digitizers, is intended to resolve 0.1% amplitude and 0.1° phase variations on time-scales longer than a few nanoseconds. The data acquisition will be controlled by local microprocessors, one of which will be assigned to each rf station, in order to permit parallel, high-level processing of the data.

We plan to monitor the transmitted and reflected rf pulses at many points along the route between each klystron and its associated accelerator structures. There will be two waveform digitizers per rf station, into which the rf phase and amplitude signals from the monitor points can be multiplexed. In this way, correlations between any two signals can be examined. An important function of the monitoring system will be to characterize the stability of the rf pulses. For this purpose, the signals will be analyzed in two basic ways. To characterize the short-term stability of some aspect of the waveform, a few hundred consecutive pulses will be sampled and analyzed. To monitor long-term stability, a sample will be taken every few minutes and stored in history buffers.

Unloaded Energy Gain

To measure the unloaded energy gain characteristics of the linac, only one klystron will be run at a time. A short bunch train, which makes the beam loading negligible, will be used to simplify the measurement. The energy gain of the bunch train depends on the rf waveform entering the two energized structures, on the rf transmission properties of the structures, and on any field emission (or breakdown) that occurs in the structures. The rf transmission properties of the structures have been computed so that, from a measurement of the input rf waveform, one can predict how the ideal energy gain should vary as a function of the transit time of the bunch train relative to the rf pulse. By comparing

this calculation to measurements done at low rf-power levels, we will test our theoretical understanding of the rf transmission properties of the accelerator sections. By comparing low- and high-power measurements, we will look for effects from possible field emission within the structures. Checks for field emission will also be made by observing the energy-gain stability at a fixed transit time for different rf power levels.

Linac Field-Emission Current

In addition to over-loading individual structures, there is a concern that field emission currents will be accelerated sufficiently to be captured by the accelerating wave and transported in an NLC-like linac. To investigate this possibility, and to provide more data on field-emission activity in the structures, the NLCTA linac will be instrumented with two types of detectors. An extended scintillation counter will be placed alongside each of the structures to provide a measure of the expelled (uncaptured) field-emission current, and toroids will be installed in the beam line at the beginning, middle, and end of the linac to measure the transported current. The time-resolution of the scintillation counters will be approximately 20 ns. The time-resolution of the toroids will be approximately 1 ns.

With the beam off, we will measure the expelled and transported current signals as functions of the rf power and of the strengths of the intervening quadrupole and dipole magnetic fields. With a strong dipole field, any wall monitor currents should be due only to field emission in the structure immediately upstream. By observing the change in the currents with no dipole field, but with different-strength quadrupole configurations, we will characterize the transport of field-emission current in the linac. Although the quadrupole field strengths available in the NLCTA will not be as great as the strengths that will be used in an NLC main linac, we believe that they will be sufficient to fully suppress the transport of the field-emission current. Studies will also be done to measure how much of the field-emission activity is associated with the presence of the beam by varying the length of the bunch train and observing the change in the time-structure of the monitor signals.

Multibunch Beam-Loading Compensation

One of the goals of the NLCTA is to demonstrate that multibunch beam-loading compensation can be readily maintained at the 0.1% level for a beam current yielding a steady-state loading of 25%. To achieve the compensation, the shape and/or timing of the rf pulses will be adjusted so that the resulting change in unloaded energy gain along the bunch train offsets the energy loss from the loading. Demonstrating compensation at the 0.1% level will require careful preparation of the bunch train so as not to generate other sources of bunch-to-bunch energy differences. The bunch train injected into the linac will be checked for tolerances on the uniformity of bunch energy, intensity, and spacing. To measure the degree of compensation, the bunch train will be analyzed in the spectrometer using a vertical kicker magnet, which will spread the bunches on a screen. From the measurements of the rf waveform entering the structures, and from our theoretical understanding of the rf transmission through the structures we should be able to predict the gross features of the bunch-to-bunch energy differences that are observed.

The method for shaping the rf waveforms will be to modulate the phase of the rf drive to the klystrons, prior to SLED-II pulse compression. Maintaining the stability of the rf pulses may require feedback which should be relatively straightforward to implement in the rf control system of the NLCTA.

Transverse Components of the Accelerating Field

The tolerances on the allowable transverse components of the accelerating field in the structures of an NLC linac are fairly tight compared to SLC standards. These tolerances differ depending on whether the transverse electric field is in-phase or 90° out of phase with the bunches, and on whether the field jitters from pulse to pulse or is static. In the

NLCTA, we will be able to measure transverse electric-field components with resolution on the order of, or smaller, than the NLC tolerances.

The basic approach in these measurements is to vary the phase of one klystron at a time and to record the change in the bunch trajectories using the BPMs downstream from the associated pair of structures. Fitting the amplitudes of the observed betatron oscillations to a sinusoidal function of the klystron phase will yield the in-phase and out-of-phase static components of the accelerating field. To measure the jitter in these components, the pulse-to-pulse rms variation of the induced betatron motion will be computed with the klystron on and off, and at the in-phase and out-of-phase settings.

To obtain accurate results will require special attention to how the data are taken. A short bunch train will be used, only one linac klystron will be powered at a time, and the quadrupoles will be turned off downstream of the associated structures so that bunch energy changes do not produce trajectory changes. The measured outgoing trajectory will be corrected pulse-to-pulse to account for any changes in the incoming trajectory. This correction will be based on the trajectory fit to the BPM data in the region between the center of the chicane and the structures being powered. With this procedure, a resolution of about 0.2 keV in the transverse accelerating field should be achieved.

The out-of-phase component of the transverse field, which will degrade the bunch emittance in the NLC due to the differential kick it produces along the length of the bunch, should be less than 1 keV to keep the emittance growth below 10%. Therefore both static and jitter components of this magnitude should be discernible in the NLCTA. Jitter in the in-phase component of the transverse field will also lead to emittance growth in the NLC, as a result of the dispersion it generates. The tolerance for a 10% growth is much smaller, about 0.2 keV, so we will not be able to put tight limits on the NLC emittance growth from this mechanism if indeed no jitter is observed.

A static in-phase component of the transverse field is fairly benign since its effect can be offset with a dipole magnet. Coupled with jitter in the energy gain, however, it also contributes to the emittance growth in the same manner as in-phase jitter. A 1% jitter in energy gain, which is reasonable for the klystrons being developed, yields a tolerance 100 times larger, or 20 keV, on the static in-phase component. Our resolution for measuring this component is also much larger since an absolute measure of the bunch angular trajectories relative to the structure axes is needed to correct the measurement for the transverse field component due to off-angle trajectories. For this correction, we will rely on the absolute BPM calibration and on the BPM alignment to the structure axes, each of which will be known to about 100 μm. These errors translate into a 10-keV uncertainty in the static field strength so, again, the measurement resolution is near the tolerance.

Transverse Multibunch Beam Breakup

The NLCTA (like the NLC) would not operate stably if conventional constant-impedance accelerator structures were used. In both cases the offset of the bunches would be amplified by many orders of magnitude by the end of the linac. The detuned structures for the NLCTA will eliminate this blowup. This will be tested experimentally using the straight-ahead line of the spectrometer and the vertical kicker magnet.

Using corrector magnets in the chicane, the bunch train will be launched into the linac with a horizontal position or angle offset. The resulting positions of the bunches exiting the linac will be measured using a profile monitor in the straight-ahead line of the spectrometer in conjunction with the vertical kicker. This will allow us to distinguish the bunches along the train by their vertical offset while observing the amplification of the initial horizontal betatron amplitude.

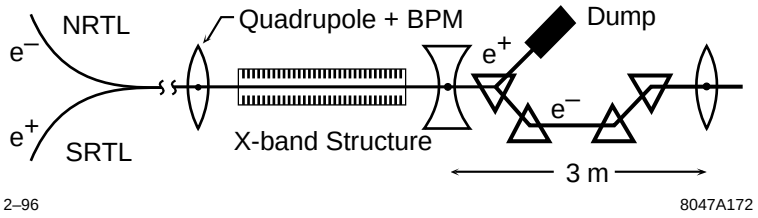

Figure 8-20. *Layout of the ASSET facility in the SLC.*

Studies with an Upgraded NLCTA Injector

There are a number of NLC linac beam-dynamics issues which cannot be readily addressed with the NLCTA as designed. The small bunch intensity produced by the X-band injector makes single-bunch longitudinal- and transverse-wakefield effects too small to be measured easily. Also, the small bunch spacing makes it extremely difficult to accurately measure the strength of the long-range transverse wakefield from its effect on betatron motion. We plan to upgrade the NLCTA injector in the future to produce NLC-like bunch trains with 0.75×10^{10} electrons per bunch and 1.4-ns bunch spacing. If a photocathode rf gun is used, we may be able to produce an adjustable-length bunch train (from 1 to 100 bunches) with a fairly small normalized (invariant) emittance ($\epsilon_n < 10^{-5}$ m-rad) and NLC-like bunch lengths (100 μm after compression).

With such an injector operating in a single-bunch mode, the mean energy of the bunch in the spectrometer would be measured as a function of bunch intensity to infer the short-range longitudinal wakefield strength. The size of this quantity is of particular interest since it has some theoretical uncertainty for such short bunches. Similarly, the strength of the short-range transverse wakefield would be inferred by measuring the change in the transverse bunch profile, using the wire scanner before the spectrometer bend, as a function of bunch intensity and betatron amplitude in the linac. To study the long-range transverse wakefields, a long bunch train would be used and the effects of the wakefields on the betatron motion of the bunches in the linac would be measured.

Until a new injector is built, some of these issues will be addressed with the Accelerator Structure SET-up (ASSET) facility at the SLC. (See Section 8.2.10.)

8.2.10 ASSET Measurements

To test the suppression of the transverse wakefields in the proposed NLC accelerator structures, a new facility has been incorporated into the SLC. This facility, the Accelerator Structure SETup (ASSET) [Adolphsen 1992] [Adolphsen 1995a], takes advantage of the low-emittance e^+ and e^- bunches that can be produced in the SLC, with individual control of the two bunch intensities and relative timing. Using the e^+ bunch as a probe, and the e^- bunch as a witness, the wakefields can be measured over an interbunch separation from zero to several hundred nanoseconds, with the sensitivity that is needed to verify the wakefield suppression required in the NLC.

The layout of ASSET is shown in Figure 8-20. One of the 3-m-long S-band accelerating sections has been removed from the SLC, and the X-band structure to be tested is inserted in its place, followed by a combination of a beam dump (for the e^+ probe bunch) and chicane (for the e^- witness bunch). The wakefield kick from the probe bunch is determined from the betatron oscillations it induces on the witness bunch.

Measurements of the wakefield amplitude in a 1.8-m-long detuned X-band structure are shown (points) in Figure 8-21, along with theoretical predictions of the amplitude (solid curves), with and without cell frequency errors included.

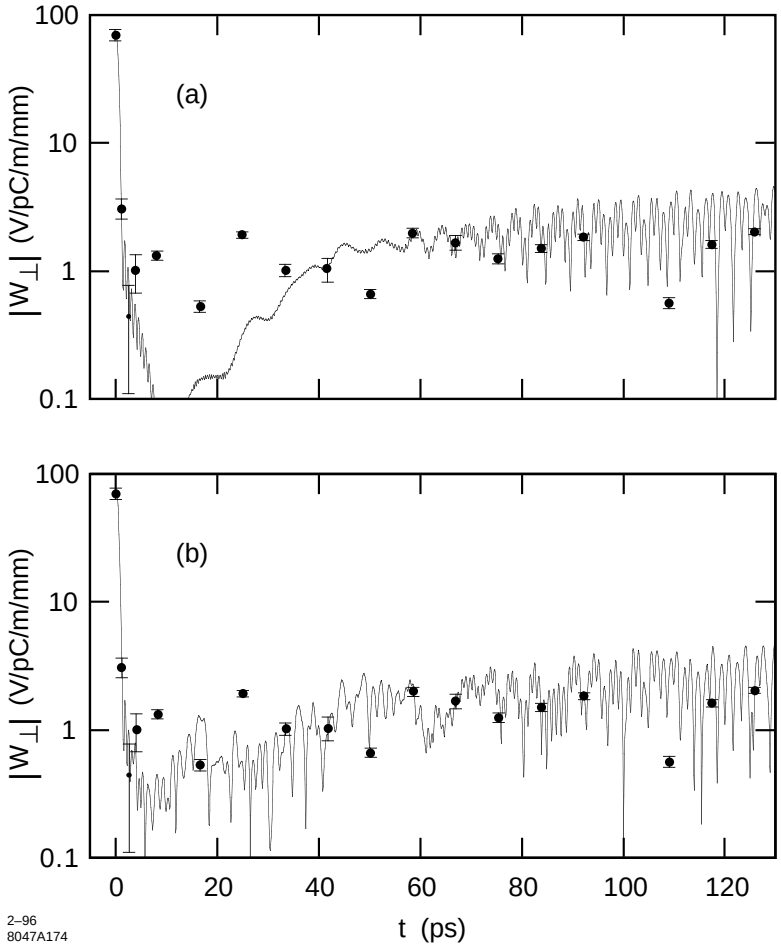

Figure 8-21. *Dipole wakefield amplitude measurements and prediction from equivalent circuit model (a) without cell frequency errors and (b) with* 1.5×10^{-4} *rms fractional frequency errors.*

The fractional frequency errors have an rms of 1.5×10^{-4}. The agreement, when frequency errors are included, is reasonably good, although the wake is somewhat more suppressed at long distances than was predicted by the equivalent circuit model, assuming Q values of 6500 for the lowest-dipole deflecting mode.

Measurements of the wakefield in the DDS will be made using ASSET when the first prototype DDS becomes available.

8.2.11 Use of Beam-Excited Modes to Monitor Alignment of Structures

Each dipole mode in the DDS (as well as the structure with detuning alone) is localized in a particular region of the structure, depending on the mode's frequency and where that frequency is cut off in the structure. Thus it is proposed to pick up the frequency of two modes, one localized near each end of the structure, and use them to measure the alignment of the structure with respect to the beam.

The desired dynamic range for the detection of position offsets in such a system is large—from about a millimeter down to a micron. Details on the design of such structure beam position monitors are given in Section 7.10.3.

8.3 RF Pulse Compression and Power Transmission

This section describes the use of rf pulse compression to multiply peak power in the NLC linac high-power rf system. The 1.2-μs-long X-band klystron pulses will be compressed by a factor of five—to 0.24 μs—using the SLED-II rf pulse compression technique [Wilson 1990]. SLED-II is a modification of SLED [Farkas 1974]. SLED is used to increase the rf power into the 60-GeV SLAC linac by a factor of about 3. In this section, we discuss the performance required, present a physical layout, and analyze its efficiency.

8.3.1 Performance

A SLED-II pulse compressor works by storing microwave energy in a pair of high-Q resonant delay lines for most of the duration of the klystron pulse. The round-trip transit time of the rf in the delay lines determines the duration of the compressed pulse. The SLED-II microwave network is shown schematically in Figure 8-22. The delay lines are coupled to input and output waveguides by a four-port 3-dB coupler (such as a "Magic T"). In normal operation with a pulse-compression ratio of five, the delay lines are filled with microwave energy for four round-trip-delay times. The microwave energy stored in the delay lines is discharged by reversing the phase of the drive power to the klystron. The stored energy then is discharged through the fourth port of the 3-dB coupler, where it combines constructively with power still coming from the klystron, forming the compressed, high-power pulse.

To achieve low losses, oversize circular waveguide, propagating the TE_{01} mode, has been used for delay lines in SLED-II prototypes. Delay-line quality (Q) factors between 4.3×10^5 and 1.0×10^6 have been achieved [Tantawi 1995a, Tantawi 1996]. Converting between the TE_{01} circular-waveguide mode and the TE_{10} rectangular-waveguide mode has been performed by compact, flower-petal type, low-loss mode transducers (see below) [Lanciani 1953, Hoag 1993, Tantawi 1993]. Figure 8-23 shows the demonstrated performance of a prototype high-power SLED-II pulse compressor at SLAC. The small variations on top of the compressed pulse are not a property of the SLED-II pulse compressor, as demonstrated by low-power testing that produced a flat pulse [Tantawi 1995a], but are due to mode impurities in the transmission line from the klystron to the pulse compressor. The design of the mode transducer has been modified, to better suppress mode impurities in the oversized TE_{01} waveguide, by adding a choke for TE_{41} and a pair of interacting chokes for TE_{11} and TM_{11} [Tantawi 1995b]. The effectiveness of this modification has already been demonstrated in a low-power "cold test" of the new mode-transducer design.

In general, there is a trade-off between the peak-power gain achieved by pulse compression, and the efficiency of the pulse compressor. For SLED and SLED-II pulse-compression systems, the trade-off is shown in Figure 8-24 [Wilson 1992]. The intrinsic inefficiency of SLED-type pulse compressors results from the inability of a SLED energy storage cavity, or a SLED-II resonant delay line, to charge or discharge completely, in a finite amount of time, through the coupling aperture that is shown schematically in Figure 8-22. A SLED-II pulse compressor with a compression ratio of five has a maximum (intrinsic) efficiency of 80.4%, which is achieved when the voltage-reflection coefficient of the coupling aperture is 0.651. (Hence, 0.651^2, or 42% of the power incident on SLED-II is reflected at the beginning of the klystron pulse.)

The net peak-power gain is the product of the pulse-compression ratio (5), the intrinsic efficiency of the pulse compressor (0.804), and the cumulative efficiency of all of the waveguides and other microwave components in the pulse compressor and transmission lines. The minimum peak power gain required to achieve the NLC-design

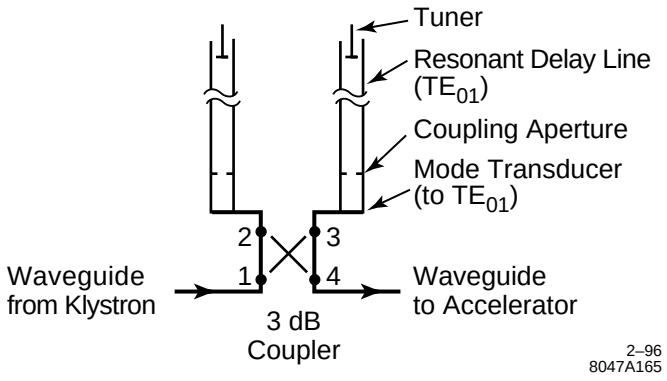

Figure 8-22. *Microwave network of a SLED-II pulse compressor.*

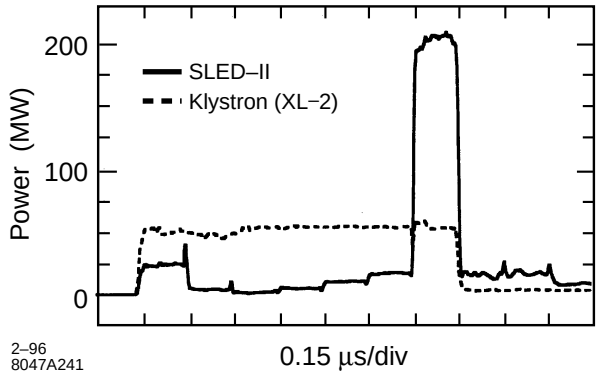

Figure 8-23. *Demonstrated performance of a prototype high-power SLED-II pulse compressor.*

accelerating gradient is 3.6. Therefore, the cumulative losses that occur due to finite conductivity and mode conversion in the entire system must be limited to 10% to achieve the desired power gain product:

$$5(0.804)(1-0.10) = 3.6 \quad . \tag{8.20}$$

Developmental SLED-II systems have been tested at SLAC with high-power X-band klystrons to validate the design and its components [Nantista 1993, Vlieks 1993, Wang 1994]. The peak power and efficiency needed for the NLCTA have been demonstrated in a prototype system. Further validation of the SLED-II design at the higher power levels and efficiencies needed for the NLC will be performed in upgrades to the NLCTA. Table 8-7 summarizes the performance of the SLED-II prototype and the plans for using SLED-II in the NLCTA and in the NLC. The rf pulse compression systems in the NLC and NLCTA are designed to accommodate future upgrades in which the peak rf power is nearly tripled, by replacing each 50-MW klystron with a pair of 75-MW klystrons, as indicated in Table 8-7.

8.3.2 Physical Layout

Figure 8-25 illustrates the physical layout of the waveguide network for rf pulse compression and power transmission to four 1.8-m-long linac sections for the two-tunnel (“SLAC-type”) configuration shown in Figure 7-11.

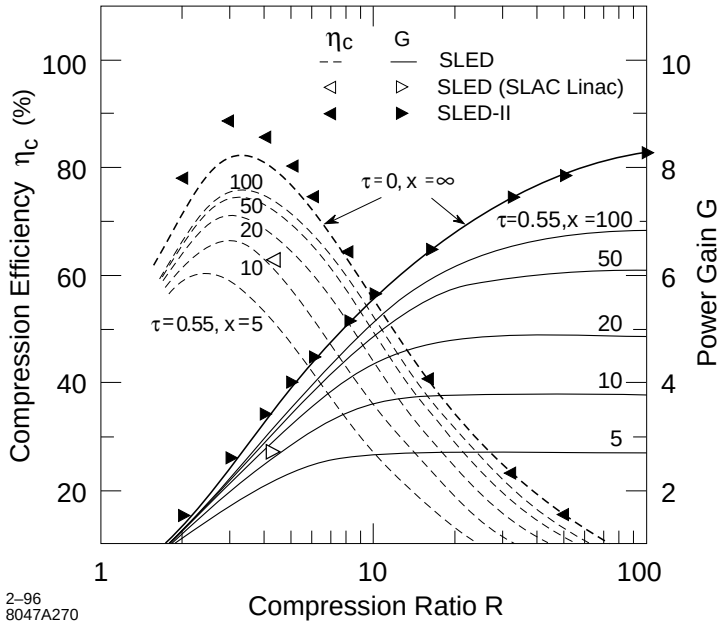

Figure 8-24. *Power gain (solid curves) and compression efficiency (dashed curves) for a SLED-II rf pulse compressor driving an accelerator structure with τ and x as indicated. τ is the voltage attenuation parameter (nepers) for the structure. x is the unloaded time constant of the pulse-compression energy-storage cavities ($2Q/\omega$) normalized to the structure filling time. The top curves show gain and efficiency for SLED as implemented for the SLAC linac. The solid triangular points are for a SLED-II system with lossless components.*

To achieve low rf power losses, oversized circular waveguides will be used for the SLED-II delay lines, and for the high-power transmission lines. The TE_{01} mode will be propagated in the circular waveguides that comprise the delay lines, in the transmission lines from the klystrons to the power combiners, and in the transmission lines from the klystron gallery to the linac tunnel. The waveguide diameters that have been chosen to avoid spurious-mode cut-offs near the operating frequency are 4.75 in (WC475) for the delay lines and 2.93 in (WC293) for the transmission lines from the klystrons. The HE_{11} "hybrid" mode will be propagated in flexible corrugated circular waveguides of approximately two-inch inner diameter that distribute power to the four accelerator sections powered by each SLED-II pulse compressor.

Rectangular waveguides, propagating the TE_{10} mode, also will be used in parts of the transmission system. The rectangular waveguide sizes that have been chosen are WR100 (1.0 in $\times$ 0.5 in) and oversize WR100 (1.0 in $\times$ 0.9 in).

Conversion between the TE_{01} circular-waveguide mode and the TE_{10} rectangular-waveguide mode will be performed by compact, flower-petal type, low-loss mode transducers [Lanciani 1953, Hoag 1993, Tantawi 1993]. Transducers of this type, shown in Figure 8-26 have been analyzed, measured, and used extensively at SLAC.

The four-way power splitter that will divide the compressed rf pulses into four equal parts has been designed by computer simulation [Kroll 1995], but the design has not yet been manufactured and tested. The four-way splitter is shown in Figure 8-25; an enlarged view is shown in Figure 8-27. The device accepts the TE_{01} circular-waveguide mode, and divides the power equally into four TE_{10}-mode rectangular waveguides.

Matching the HE_{11} "hybrid" mode in corrugated circular waveguide to the TE_{10} mode in rectangular waveguide may be performed by relatively simple tapers, since the two modes have essentially the same character.

	Prototype 3/95[a]	NLCTA Design	NLCTA Upgrade	NLC Design	NLC Upgrade
Klystron pulse width	1.05 μs	1.5 μs	1.5 μs	1.2 μs	1.1 μs
Compressed pulse width	0.15 μs	0.25 μs	0.25 μs	0.24 μs	0.22 μs
Compression ratio	7	6	6	5	5
Klystron peak power	55 MW	50 MW	$4\times$(50–75) MW	2×50 MW	4×75 MW
Intrinsic efficiency of SLED-II without losses[b]	0.692	0.746	0.746	0.804	0.804
Efficiency of SLED-II components	0.92	0.90	0.90	0.95	0.95
SLED-II gain (Max. possible)	4.42 (4.82) [c]	4.0 (4.48)	4.0 (4.48)	3.8 (4.02)	3.8 (4.02)
Efficiency of transmission lines	0.84	0.90	0.90	0.95	0.95
Transmitted power	205 MW	180 MW	720–1080 MW	360 MW	1080 MW
Net power gain	3.7	3.6	3.6	3.6	3.6

[a] Achieved.

[b] Assumes the delay-line reflection coefficient is optimized for the stated compression ratio.

[c] The delay-line reflection coefficient was optimized for a compression ratio of 8 in the prototype test.

Table 8-7. *Performance of SLED-II rf pulse compressors.*

The waveguide layout is sufficiently flexible to absorb the absolute motion of the accelerator sections due to their mechanical movers (± 1 mm) and the relative motion between the klystron gallery and the accelerator tunnel due to settling (± 10 mm).

The SLED-II waveguide networks are located in the low-radiation environment of the klystron gallery so that the rf pulse-compression system may be modified, station by station, if necessary for upgrade to higher beam energies, simultaneously with colliding beam operations.

Since the round-trip delay time in the 4.75-in-diameter waveguide (at the group velocity, 0.964c) must equal the rf pulse duration (0.24 μs), the physical length of the SLED-II delay lines is 34.7 m. The physical layout can accommodate this delay-line length by spatially overlapping the delay lines from adjacent rf stations. Since the total length of linac fed by each rf station is approximately eight meters, each pair of delay lines will overlap parts of five other pairs of delay lines.

The alternate tunnel configuration, the semi-elliptical highway-style tunnel shown in Figure 7-12 is topologically similar to the physical layout presented above. The waveguide configurations differ only in the lengths of very low-loss oversized circular waveguides. The circular waveguide from each klystron to the power combiner is longer (3 m *vs.* 1 m) since it must pass through the shielding wall. The waveguide from the pulse compressor to the accelerator is much shorter (1 m *vs.* 10 m) since, in this configuration, the pulse compressors are in close proximity to the linac.

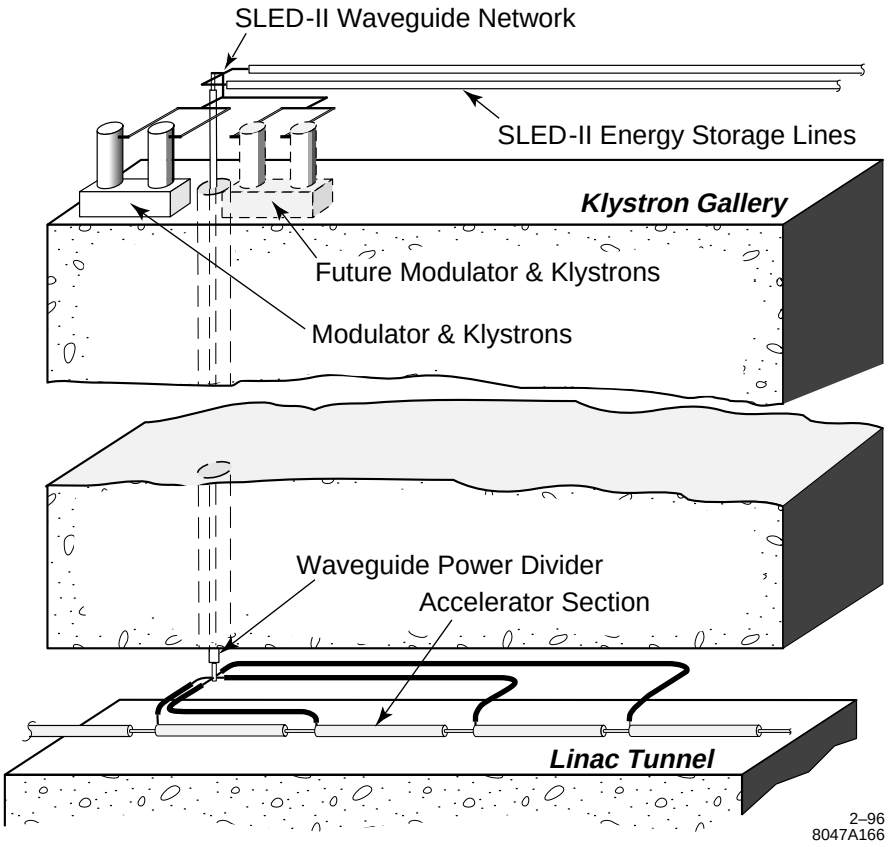

Figure 8-25. *Physical layout of the waveguide network for rf pulse compression and power transmission.*

8.3.3 Power Losses

To realistically estimate the peak power gain of the physical layout illustrated in Figure 8-25 we have constructed a “loss budget” for the rf system based on the separate components from which the above physical layout might be assembled. The losses assumed for the individual components are based on a combination of actual experience with identical or similar devices, and theoretical estimates derated for imperfect conductivity and manufacturing tolerances.

Ohmic losses in all waveguides are assumed to exceed standard theory [Ramo 1984] by 20% to allow for imperfect conductivity and surface roughness. This has been confirmed empirically for the NLCTA's WC293 transmission lines.

The 3-dB power combiner/divider is assumed to be a WR100 “Magic T” with one-way power loss of 1%. Our experience with WR90 Magic Ts consistently has yielded losses of about 1.2%, due to a combination of ohmic loss, energy trapped in the junction, and finite reflection. Using a WR100 is expected to reduce the ohmic contribution by the ratio of ohmic losses in WR100 compared to WR90, which is 3/4.

The power loss assumed for the flower-petal-type mode transducer, 0.7%, is consistent with the measured loss of the NLCTA mode transducers.

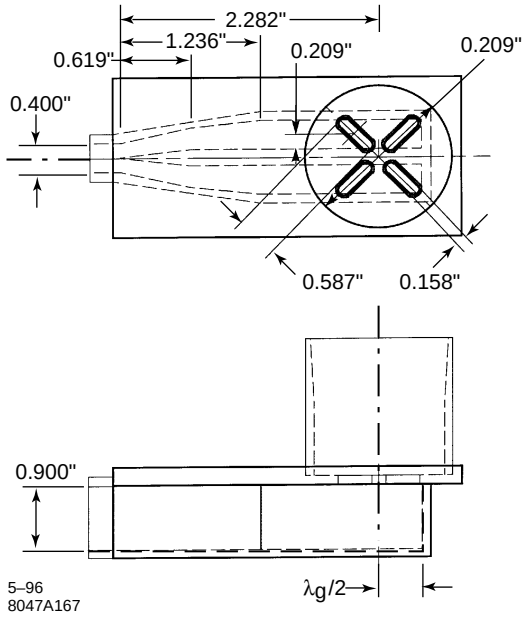

Figure 8-26. *Mechanical drawing of the "flower-petal" mode transducer.*

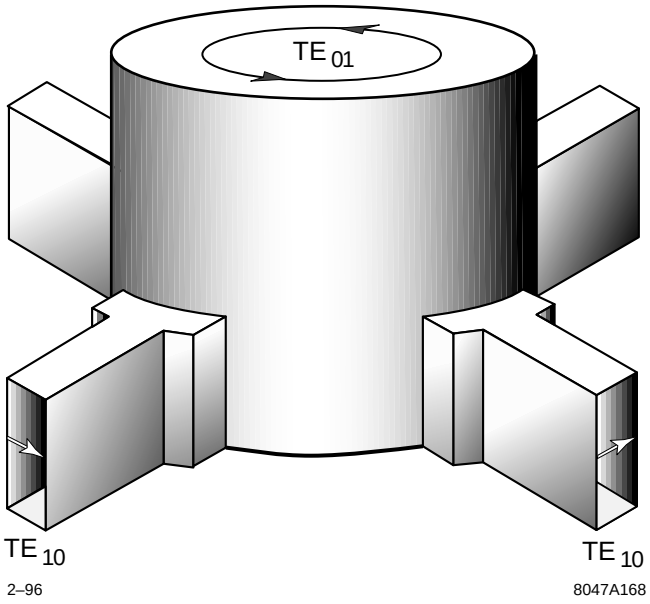

Figure 8-27. *Sketch of the four-way power splitter designed by computer simulation.*

Power losses in the four-way power splitter are assumed (in the absence of a measured prototype) to be the same as for the flower-petal-type transducer, 0.7%. Less loss is expected due to the symmetry of the device, which guarantees mode purity (in the absence of mechanical imperfections).

The loss budget for the physical layout shown in Figure 8-25 is summarized in Table 8-8. In the table, power losses and transmission fractions are tabulated for individual components and for groups of components, including the SLED-II pulse compressor, the transmission lines from the klystrons, and the transmission lines to each accelerator section. The net power gain is tabulated separately for each of the four accelerator sections. The table presents a detailed accounting of the power losses for each of the four accelerator sections. The average power transmission is 89.6%, resulting in a net power gain (averaged over the four accelerator sections) of 3.60.

For the semi-elliptical highway-style tunnel configuration shown in Figure 7-12, the waveguide configuration differs only in the lengths of very low-loss oversized circular waveguides. The loss budget and the resulting net power gain are nearly identical to those in the two-tunnel (SLAC-type) configuration.

8.4 High-Power Klystrons

The design of the 50-MW (X5011) klystron is the product of an ongoing development program which began at SLAC in 1988. At that time, the peak power, frequency, and pulse duration required in combination were well beyond the state of the art. As a result, rf circuit breakdown and output window failures plagued early development efforts at SLAC. Through a steady stream of improvements, the failure modes are largely under control. SLAC presently has four 50-MW solenoid-focused klystrons in operation. Three of these are suitable for use in the NLC Test Accelerator. The PPM-focused X5011 klystron, in which a periodic permanent magnet (PPM) array replaces the solenoid, is in the final stages of computer simulation, mechanical design and fabrication. Those parameters which have not yet been demonstrated have been shown to be achievable through computer simulation.

The upgrade of the NLC to 1 TeV center-of-mass energy requires a 75-MW peak power klystron. The preliminary electrical and mechanical design of this klystron, designated X7511, has been carried out. The criteria applied in the design of the 75-MW klystron were not to exceed the design limits imposed on the 50-MW klystron and, to the greatest extent possible, to stay within the gradients and stress levels demonstrated in the X5011. The upgrade is discussed in Section 8.4.3, “Upgrading Performance”.

Design and performance parameters for the X5011, 50-MW X-band klystron are given in Table 8-9. Key features of the tube are identified in Figure 8-28.

8.4.1 Design Features

Table 8-9 lists the design and performance parameters which make up the preliminary specification for the X5011 klystron. The design features and innovations which make the specification achievable are described below.

Electron Gun

Figure 8-29 shows the electrode configuration of the electron gun and the electron beam which is produced, based on the computer code EGUN. The cathode diameter (5.72 cm) is a compromise. A larger cathode would reduce the maximum voltage gradient (230 kV per cm, which is high, but acceptable), but would increase the beam area

Component	Unit	Loss	Transmission Subtotals				Net Gain[a]	
		(Linear)	(Linear)	(dB)	(dB)	(Linear)	(dB)	(Linear)
Definitions of Components								
TE_{01}–TE_{10} Transducer	(each)	0.0070	0.993	−0.031				
WR100 "Magic T"	(each)	0.0100	0.990	−0.044				
WR100 ($1.0'' \times 0.5''$)	(m)	0.0205	0.979	−0.090				
Oversize WR100 ($1.0'' \times 0.9''$)	(m)	0.0133	0.987	−0.058				
Corrugated WC220 (HE_{11})	(m)	0.0011	0.9989	−0.0048				
WC293 (TE_{01})	(m)	0.0010	0.9990	−0.0042				
WC475 (TE_{01})	(m)	0.00022	0.99978	−0.00093				
Trans. Line from Klystron					**−0.137**	**0.969**		
WC293 (TE_{01})	1.0	0.0010	0.999	−0.004				
Mode Transducer	1	0.0070	0.993	−0.031				
Oversize WR100	0.5	0.0067	0.993	−0.029				
WR100 "Magic T" Combiner	1	0.0100	0.990	−0.044				
Oversize WR100	0.5	0.0067	0.993	−0.029				
SLED-II Pulse Compressor					**−0.233**	**0.948**		
WR100 "Magic T"	2	0.0199	0.980	−0.087				
Mode Transducer	2	0.0140	0.986	−0.061				
WC475 Delay Lines (TE_{01})	34.7	0.0193	0.981	−0.084				
Trans. Line to Linac Tunnel					**−0.070**	**0.984**		
Mode Transducer	1	0.0070	0.993	−0.031				
WC475 (TE_{01})	10	0.0021	0.998	−0.009				
Mode Transducer (4-way split)	1	0.0070	0.993	−0.031				
Trans. Line to Section #1					**−0.023**	**0.995**	**5.580**	**3.614**
WR100 Taper	0.1	0.0021	0.998	−0.009				
Corrugated WC220 (HE_{11})	1.0	0.0011	0.999	−0.005				
WR100 Taper	0.1	0.0021	0.998	−0.009				
Trans. Line to Section #2					**−0.030**	**0.993**	**5.572**	**3.608**
WR100 Taper	0.1	0.0021	0.998	−0.009				
Corrugated WC220 (HE_{11})	2.5	0.0028	0.997	−0.012				
WR100 Taper	0.1	0.0021	0.998	−0.009				
Trans. Line to Section #3					**−0.040**	**0.991**	**5.563**	**3.600**
WR100 Taper	0.1	0.0021	0.998	−0.009				
Corrugated WC220 (HE_{11})	4.5	0.0050	0.995	−0.022				
WR100 Taper	0.1	0.0021	0.998	−0.009				
Trans. Line to Section #4					**−0.049**	**0.989**	**5.553**	**3.592**
WR100 Taper	0.1	0.0021	0.998	−0.009				
Corrugated WC220 (HE_{11})	6.5	0.0072	0.993	−0.031				
WR100 Taper	0.1	0.0021	0.998	−0.009				
Average over all four sections					**−0.475**	**0.896**	**5.567**	**3.603**

[a] Net gain includes SLED-II compression ratio (5) and intrinsic efficiency (0.804).

Table 8-8. *Summary of the microwave power losses, power-transmission fractions, and power gains. The losses assumed for the separate components are defined in the topmost section.*

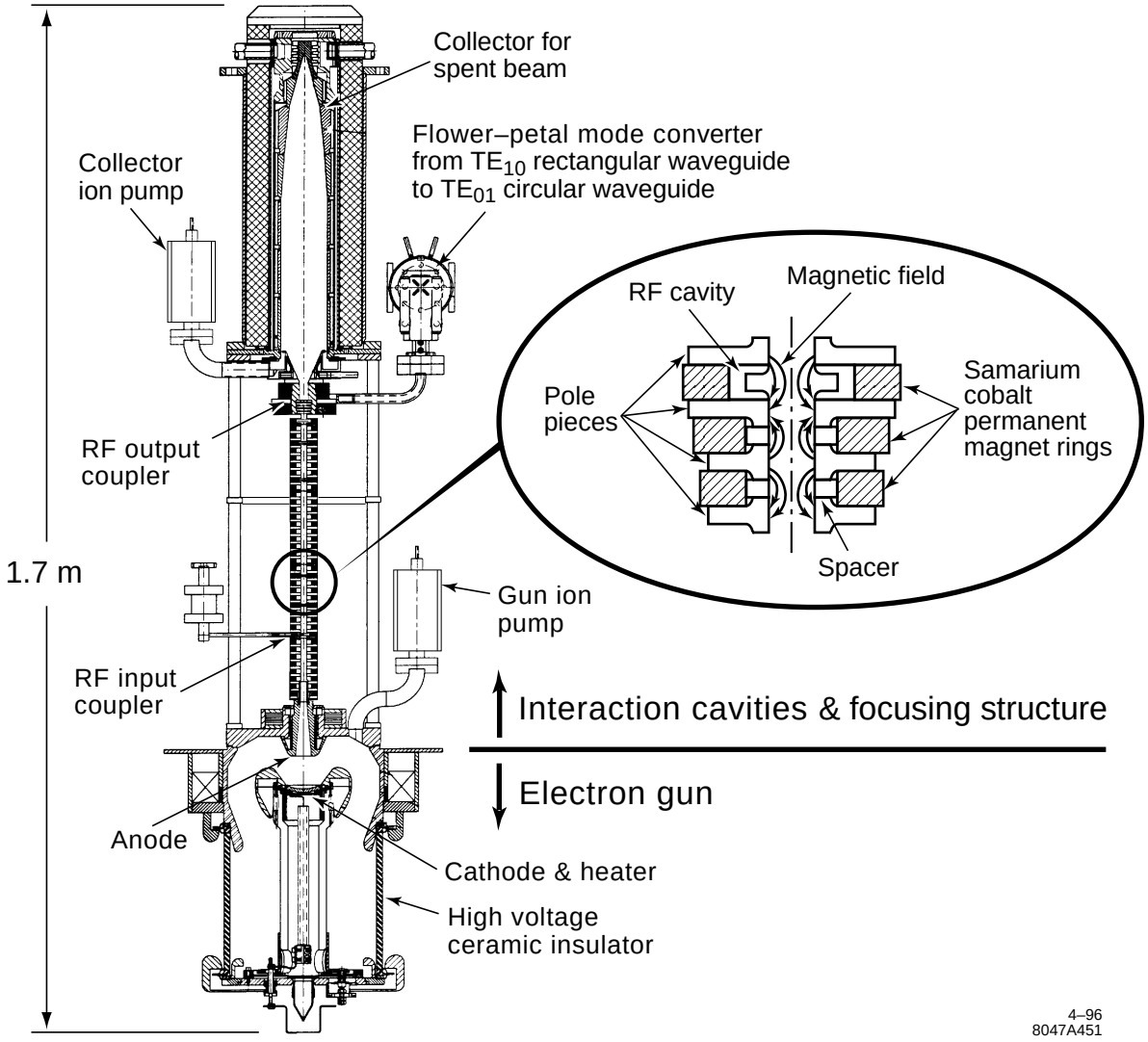

Figure 8-28. *Preliminary layout of the X5011 klystron, with water jacket removed. The insert shows one representative buncher cavity, to illustrate the use of oversize permanent magnets.*

Parameter	Units	Value
Electrical:		
Frequency	(GHz)	11.424
Peak Power	(MW)	50
Beam Voltage	(kV)	465
Beam Current	(A)	190
Beam Microperveance	(μA/ V$^{3/2}$)	0.6
Gain	(dB)	57
Bandwidth	(MHz)	100
Beam Modulation		Cathode Pulsed
Pulse Duration	(μs)	1.20
Rep Rate	(Hz)	180
RF Efficiency	(%)	57
Cathode Current Density	(A/cm^2)	7.4
Heater Voltage	(V)	15
Heater Current	(A)	21.5
Mechanical and Magnetic:		
Beam Focusing		Periodic Permanent Magnet (PPM)
Tube Weight	(kG)	32 (without lead)
Tube Length	(m)	1.3
Cathode Diameter	(cm)	5.72
Cathode Half Angle	(°)	25
Beam Area Convergence		144

Table 8-9. *Design and performance parameters for the X5011 klystron.*

convergence (currently 144/1, also high, but achievable). The resulting cathode current density, which averages 7.4 A cm^2, with a peak value of 10 A/ cm^2 at the cathode edge, is consistent with long cathode life. The 7.4 /Amp/ cm^2 compares with 6 A/ cm^2 in the 5045 SLC klystron, which has a mean time between failures (MTBF) in excess of 40,000 hours.

Elimination of the solenoid made possible by the PPM beam focusing removes any constraint on the size of the high-voltage ceramic, which allows for conservative high voltage-seal gradients. The absence of the solenoid also makes room for an ion pump which will be used to pump the gun directly through the anode, further reducing the risk of high-voltage gun breakdown.

Beam Focusing

Figure 8-28 shows details of the periodic magnetic structure and magnets which supply the beam focusing magnetic field. The magnetic circuit is designed to minimize the volume of the relatively high-cost samarium cobalt ring magnets. Oversized magnets are required at the location of the gain and buncher cavities as shown. A segmented magnet is used to supply the unidirectional field for the extended interaction output circuit (not shown).

Two key features of the magnetic circuit design make it possible for the periodic magnetic field to provide focusing, with and without rf drive, which is comparable with that provided by a high field solenoid.

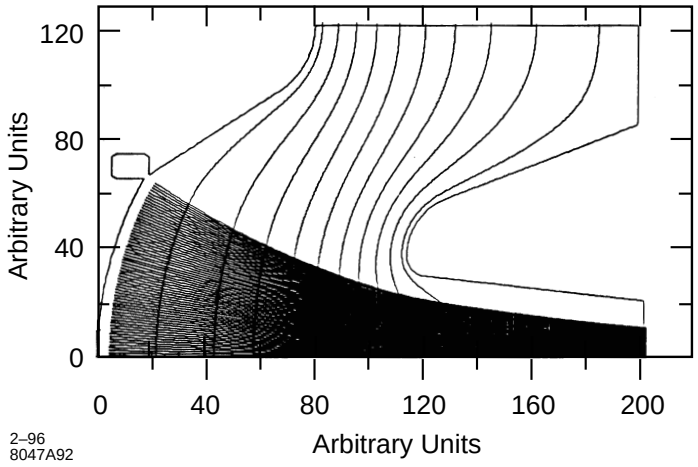

Figure 8-29. *Computer printout of gun electrodes and electron beam for the X5011.*

- **Short Magnet Period:** The periodic length of the PPM focusing structure used here is about one-half that customarily used in traveling-wave tubes, most of which are PPM focused. As a result, the stop-band voltage, the voltage below which all focusing ceases, a feature of all axially symmetric PPM focusing, occurs at about 6% of operating voltage where it does not materially worsen intercepted beam current during the pulse. By contrast, traveling-wave tubes with their longer magnet periods are forced to operate with stop-band voltage ratios of 25–50% of operating voltage.

  An even more important benefit of the short magnet period is that it produces a contoured field, having an rms value at the beam tunnel wall as much as twice that on the axis, which results in a high degree of beam stiffness. The higher field at the wall is capable of focusing a beam having a current density almost four times that which can be focused on the axis.

- **Tailored Field Amplitude:** Another advantage of PPM focusing over solenoid focusing is that the field amplitude can be tailored to a much greater degree to match the known beam conditions. As the beam is bunched and charge density increases in passing through the buncher cavities, the on-axis magnetic field required to maintain optimum focusing increases. The required tailoring of the magnetic field amplitude is easily carried out by simply using either larger diameter or higher-energy product magnets in the region where a higher field is required.

Figure 8-30 is a plot of the on-axis magnetic field which has been found in computer simulation to produce the best rf performance while avoiding beam interception. Figure 8-31 is a computer simulation of the focused beam with no rf drive.

RF Circuit

Figure 8-32 shows the layout of the rf circuit cavities approximately to scale and in their correct relative positions. The circuit consists of an input plus two gain cavities, three buncher cavities, and a five-cell, disk-loaded, extended-interaction, traveling-wave output circuit. These are described in more detail below:

Gain Cavities: The input and gain cavities are tuned near synchronism for maximum gain but with enough stagger to provide the bandwidth needed to ensure proper operation of the pulse compression system.

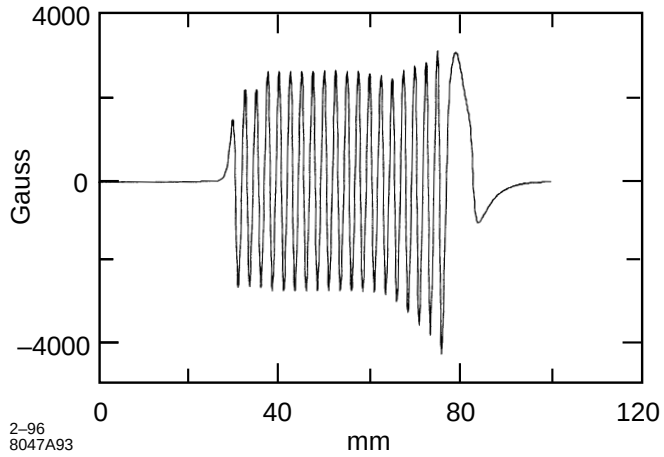

Figure 8-30. *Magnetic field profile for best efficiency without beam interception.*

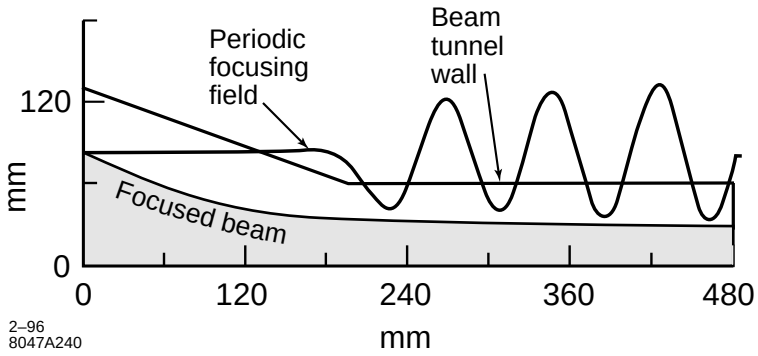

Figure 8-31. *Computer simulations of X5011 PPM-focused beam in the launch region. The periodic focusing field is also shown.*

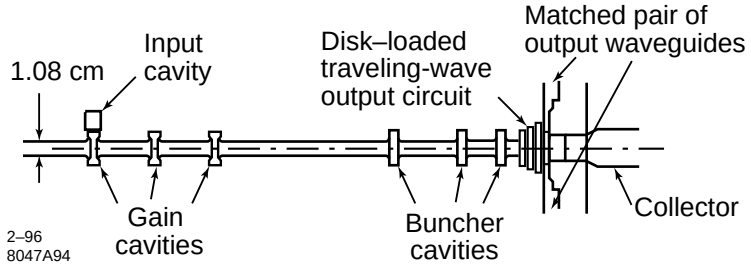

Figure 8-32. *Rf circuit cavity layout, drawn approximately to scale.*

Figure 8-33. *Computer simulation of bunched beam passing through the X5011 disk-loaded output circuit. The vertical scale is magnified by 3 to emphasize the growth of bunch amplitude in the output circuit.*

Buncher Cavities: The three buncher cavities replace the single penultimate cavity found in most klystrons. The buncher function was split into three parts to maintain an acceptable rf surface gradient. It was discovered that this approach has the further advantage that it provides a more adiabatic bunching of the beam with a higher rf current (I_1/I_0) which enhances efficiency.

Output Circuit: For the same reason that three buncher cavities are used, it was found necessary to employ an extended interaction type of output circuit to control rf breakdown. For high efficiency, rf voltage across the total length of the output circuit must be comparable with the 465-kV beam voltage. The maximum surface gradient is necessarily much higher than the on-axis gradient.

The output circuit is tapered in both impedance and velocity. Tapering the impedance from cavity to cavity by a factor of about five, from highest in the first cavity to lowest in the fifth cavity, produces a nearly constant rf voltage per gap. The velocity taper ensures that the wave remains in synchronism with the slowing beam for maximum energy extraction. It is fortuitous that the impedance taper is achieved with a physical taper of the circuit, with each successive cavity disk having an increased inner diameter, as efficiency is enhanced by allowing the highly bunched beam to expand as it traverses the output circuit. The circuit taper accommodates the beam expansion, free of beam interception. The computer simulation "snapshot" of the bunched beam traversing the output circuit under saturation conditions of Figure 8-33 clearly illustrates this phenomenon. The computed efficiency in the simulation was 63%. We have derated the specification efficiency to 57%, pending hot tests. A 10% reduction in measured versus simulated performance is not uncommon.

Output Coupler and RF Window

Rf power exits the klystron and passes through a pair of symmetrically-disposed, rectangular waveguides. It is then combined in a single rectangular waveguide before being converted to the TE_{01} circular waveguide mode, using a flower-petal mode converter. The power exits the klystron through a TE_{01} disk window. Figure 8-34(a) is a sketch of the circular disk window and matching irises which complete the rf output coupling from the tube. The matching irises and quarter wavelength ceramic disk window in combination are designed to produce a traveling-wave through the ceramic disk, as opposed to the standing wave which is used in the more conventional half-wave resonant window. The advantage of the traveling wave is that the rf gradient on the window surface is half as great for a given power flow as that for the standing-wave window. The lower gradient reduces the chance of window breakdown. The advantage

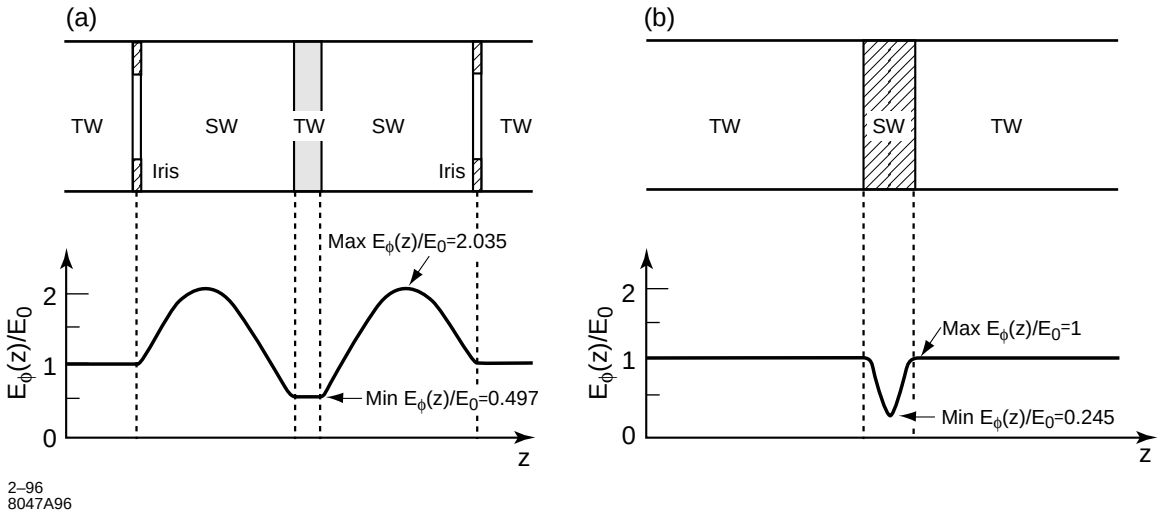

Figure 8-34. *Comparison of the reduced-field TW window (a) with a half-wave resonant SW window (b), both operating in the TE_{01} circular mode. In addition to the TW version having substantially lower rf electric field at the window surface, the integrated dielectric power losses are only 23% those of the half-wave resonant window. The horizontal scale is expanded for clarity.*

of coupling the power through the window in the TE_{01} mode is the total absence of rf electric field terminating on the metal wall of the waveguide, again enhancing power handling capability.

8.4.2 Results To Date

Status

SLAC currently has four operating 50-MW, X-band klystrons. Three of these will serve as klystrons for the NLCTA. The first of the series, XL-1, is not suitable for the NLCTA because of insufficient bandwidth. XL-2 and XL-3 operate at 50-MW peak power, at approximately 440-kV beam voltage, and at 36%–40% rf efficiency, depending upon operating settings. Preliminary testing of XL-4 has demonstrated up to 48% rf efficiency. These solenoid-focused klystrons use a microperveance 1.2 electron gun, with an input cavity, two gain cavities, and three buncher cavities. Both XL-1 and XL-2 have three-cell, disk-loaded, standing-wave, extended-interaction output circuits while the disk-loaded circuits in XL-3 and XL-4 are traveling wave. The 2.5D CONDOR computer simulation for XL-1 and XL-2 predicts a maximum efficiency of approximately 43% which yields about 10% more power than obtained experimentally. The maximum efficiency measured with XL-3 was 43% with a simulated value of 50%. XL-4 incorporates rf cavity design refinements and spurious mode suppression techniques which result in a simulated efficiency of 52% compared with the preliminary measured value of 48%.

Figure 8-35 is a pictorial overview of XL-1, including a drawing of the tube and solenoid, a table of design and performance parameters, and an oscillographic recording of beam current and rf input and output pulses.

XL-4, the most recent refinement of the solenoid-focused 50-MW klystron designs, has produced clean, stable rf pulses of 50-MW peak power for pulse durations up to 2 μs, and 75-MW peak power for pulse durations up to 1.1 μs. This performance exceeds the pulse durations required for the NLC design and upgrade. The 75-MW, 1.1 μs pulse is shown in Figure 8-36.

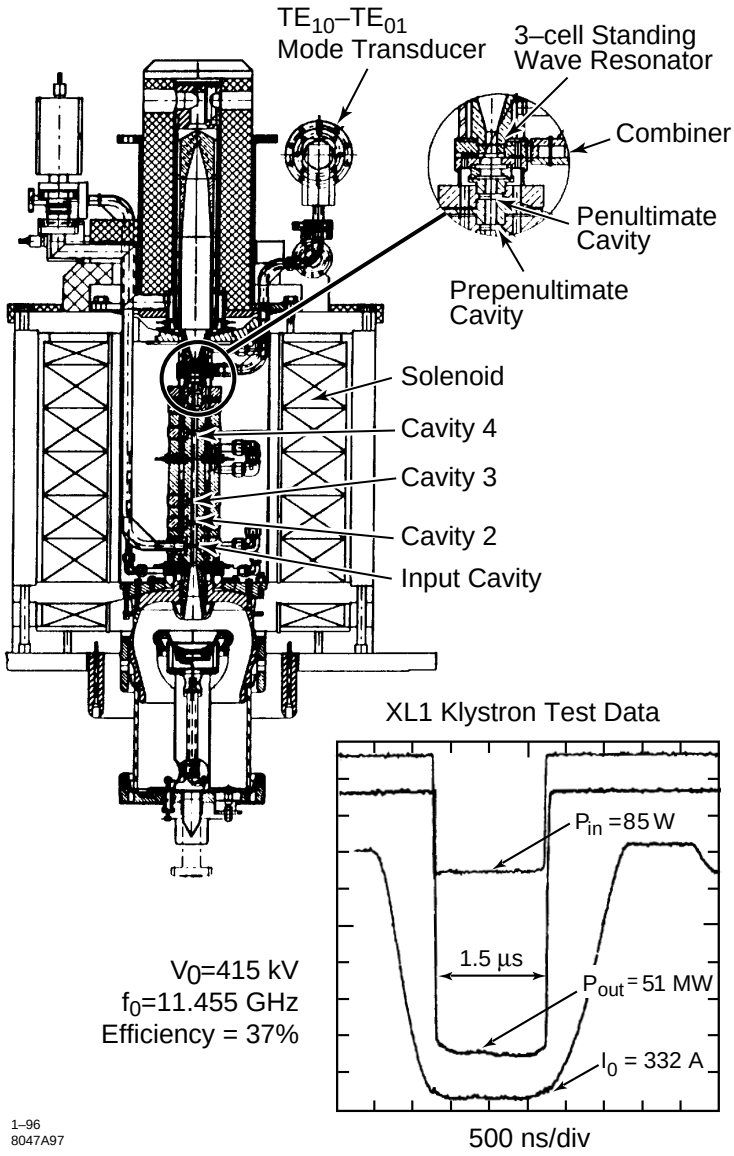

Figure 8-35. *Overview of XL-1, 50-MW klystron, and high-power test results.*

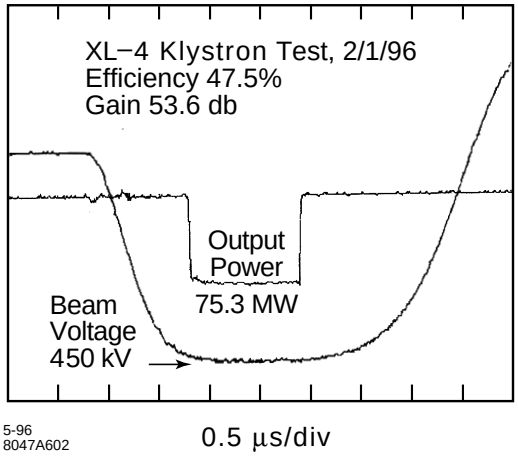

Figure 8-36. *High-powered test of XL-4 klystron. Output power, 75.3-MW. Pulse duration, 1.1 μs.*

Development History

All experimental results to date are based on solenoid-focused tubes. The XL series of klystrons is the most recent. These were preceded by the XC series of eight higher current tubes (microperveance 1.8). It was the experience gained from this earlier series of tubes that narrowed the choice of rf circuits suitable for the required peak power and pulse length, and that led to gun and rf window improvements which resulted in functional, long-pulse, 50-MW klystrons. Highlights of the development history follow.

Choice of Voltage and Current. The initial objective was to achieve 100 MW of peak power at 1 μs pulse length. It was necessary that these initial tubes match the capability of the modulators on hand at SLAC, which were limited to 440 kV. This, in turn, required high beam currents (1.8 microperveance) to obtain sufficient beam power to have a chance of producing 100 MW of peak power. The plan was to convert to higher voltage, lower current designs (for higher rf efficiency) when an appropriate modulator came online.

The choice, four years into the program, to develop 50-MW tubes for the NLCTA, made it possible to reduce the beam microperveance to 1.2 at the same 440-kV voltage with a consequent improvement in efficiency. This led to the XL tubes described earlier. In order to obtain equivalent power from PPM-focused tubes, the beam perveance needed to be reduced still further. This adjustment was imposed by the limit on the rms magnetic field obtainable from permanent magnets. The available range varies from microperveance 0.47 on the low side, dictated by the 500-kV maximum desirable beam voltage, to 0.9 on the high side, dictated by magnetic field considerations. The first PPM klystron, the X5011, described in Table 8-9, is currently in the design stage and will be tested in mid-year 1996. Computer simulations, showing up to 63% rf efficiency, have been carried out. The tube is designed to produce 50 MW of peak power at 465 kV at a microperveance of 0.6.

Rf Circuits. Figure 8-37 shows all of the rf circuit types that were tested in the XC phase of the development program. They include a conventional, single-reentrant cavity; two reentrant cavities; both inductively coupled and uncoupled; and three versions of disk-loaded (capacitively coupled) extended-interaction circuits; four- and five-cell traveling-wave and four-cell standing-wave. The single and double inductively coupled reentrant cavities were limited by rf breakdown to a pulse length of less than 200 ns. The uncoupled reentrant cavities performed well, producing

86-MW peak power at 36% efficiency at 600 ns of pulse length. This design approach was not pursued further because of the necessity of combining the power from four output waveguides, with an uncertain impact on rf stability.

The disk-loaded, traveling-wave circuit showed the best pulse length capability at 1 μs with 51-MW peak output power. The low measured efficiency, about 24%, also demonstrated the need for a more sophisticated design approach. This was achieved using 2.5D computer simulations which incorporated circuit tapers in both impedance and velocity. The first disk-loaded, standing-wave circuit, the four-cell XC8, exhibited a destructive zero mode oscillation which was eliminated in the subsequent XL-1 and XL-2 klystrons. The XL-1 and XL-2 use three-cell, standing-wave circuits.

One important design criterion to emerge from the XC series of the development was the need for good axial symmetry in the output circuit, including output and cavity-to-cavity coupling. All of the circuits with single-coupling slots or single (one-sided) output waveguides broke down at pulse lengths below 200 ns, in general with asymmetrical cavity damage. Symmetrical, disk-loaded cavities with two balanced output ports, and uncoupled reentrant cavity pairs with four balanced output ports performed best. It appears that field asymmetries cause beam steering which becomes destructive in much less than the required 1.5 μs.

Rf Windows. The rf window development and refinement is the most nearly complete of the major development efforts associated with the X-band klystron. The use of the traveling-wave, TE_{01} mode window as contrasted with the TE_{10} standing-wave, modified pill box window of our early X-band klystrons has had a remarkable effect on power handling capability. In the resonant ring, the traveling-wave TE_{01} windows have demonstrated the capability of transmitting 100 MW of rf power at 1.5 μs pulse length. By contrast, breakdown in the TE_{10} mode windows has been observed at as little as 25-MW peak power at a pulse length less than half of that achieved with the TE_{01} window.

The development progression was from TE_{10} modified pill box to the TE_{01} standing-wave window, followed by the TE_{01} traveling-wave window and finally the latter window using a high-purity, isostatically-pressed window disk. Isostatically-pressed windows have yet to fail in the resonant ring, even at a peak power above 100 MW. One traveling-wave window of standard grade alumina was punctured at 100 MW. At the present time, the high-purity, isostatically-pressed window is limited by vacuum leaks through the brazed joint. This has been of sufficient concern that no isostatically-pressed window has been used in a tube. The development effort to obtain better metalizing is continuing. Meanwhile, the 100-MW maximum capability demonstrated by the standard grade alumina disk provides an adequate margin.

8.4.3 Ongoing R&D

The remaining R&D is of three types:

- Validating basic design concepts.
- Strengthening those areas where more performance margin could lead to longer life and higher reliability.
- Upgrading performance.

Validating Basic Design Concepts

Disk-Loaded, Traveling-Wave Output Circuit (XL-3). At this writing (February 1996), the solenoid-focused XL-4 with the four-cell, disk-loaded output circuit, has undergone preliminary testing. In computer simulation, this circuit

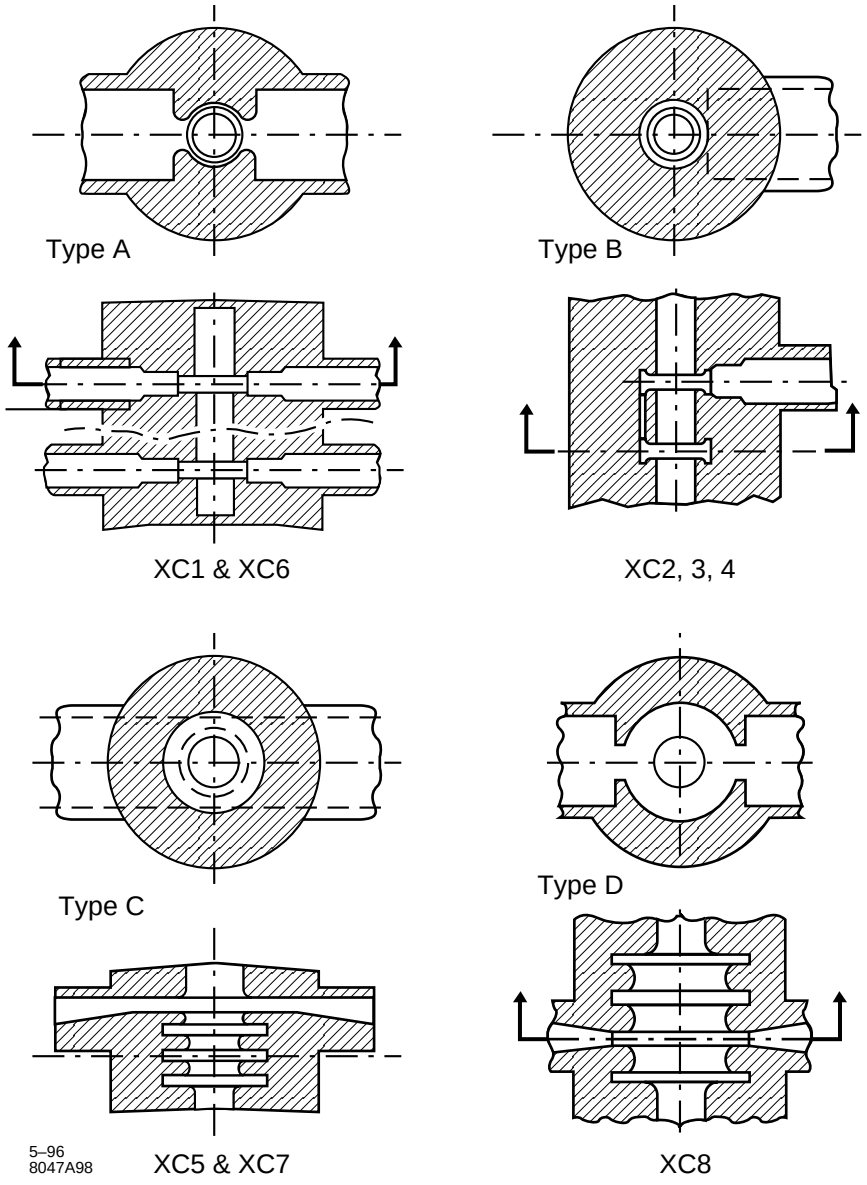

Figure 8-37. *Comparison of the rf output circuit types tested on the high-current XC series of NLC klystrons.*

showed the highest rf efficiency (52%) of the XL solenoid-focused series. This compares with a measured value of 48%.

PPM Focusing. Two PPM-focused test vehicles are currently under development. The first is the beam stick pictured in Figure 8-38. It is essentially a klystron without cavities. The beam stick is being used to test DC transmission (no rf) in two modes of operation:

- Brillouin Focusing (No flux threading the cathode)
- Partially Immersed Flow (50% flux threading the cathode)

All solenoid-focused, high-power klystrons use extensive cathode immersion (up to 95%) to achieve a high degree of beam stiffness to prevent rf driven beam interception. PPM simulations to date indicate that the combination of short magnet period which produces a contoured field, and the use of a profiled field (increase in amplitude with increased bunching) make it unnecessary to use partially immersed flow to further enhance beam stiffness. Because the simulations do not take into account a possible current halo around a real beam, we have also carried out PPM-focusing simulations, and the required design modifications to achieve beam flow with 50% cathode immersion.

The second test vehicle will be the X5011 klystron, which is designed to produce 50-MW output power at 465 kV with a beam microperveance of 0.6. Computer simulations of this tube predict an efficiency of 63% and no beam interception.

Performance Margin

Output Circuit RF Voltage Hold-off. An experimental program has been launched to identify the source of rf breakdown at relatively low-surface gradient which has been observed in all X-band klystron output circuits at SLAC. The output circuit breakdown occurs at about 20% of the rf surface gradient to which SLAC accelerator structures have been successfully subjected. At the present time, it is believed that the degradation in hold-off gradient is the result of the presence of the high-current electron beam, perhaps in conjunction with the solenoidal field which is used to confine the beam. The presence of the confining magnetic field alone has been ruled out as the cause, by initial tests of a cavity in the X-band resonant ring with and without magnetic field. A series of additional cavities is being tested in the resonant ring, to determine the effect on breakdown voltage of diamond-turned surfaces and more exotic surface cleaning procedures as well as the use of both sputter coatings and alternative cavity materials such as Elkonite (tungsten-copper) and perhaps Glidcop.

Use of Internal Loss. Most high-voltage klystrons display high-frequency anomalies in the form of observable oscillations at frequencies that are capable of propagating in the beam tunnel. The degree to which these occur appears to increase with increasing beam voltage. At SLAC, they became most pronounced in the first of two recently completed 535-kV, 150-MW, S-band klystrons developed for DESY in Germany. The problem was largely eliminated by substituting lossy stainless steel for copper in the beam drift tunnel in the second klystron. Similar oscillations, which limit the range of usable operating parameters, such as beam voltage and focusing field were encountered in the testing of XL-3. The objective of this R&D effort is to incorporate loss in the beam tunnel for the purpose of preventing, or at least damping out, such oscillations. The simple expedient of using stainless steel has been added to XL-4 in a manner similar to that of the second DESY klystron. It is too early in the test cycle to be sure that the modification has been completely successful.

The testing of a more invasive, but potentially more effective approach is planned. The initial test-bed for these experiments is the 65-MW, 5045, S-band klystron used in the SLC at SLAC. Lossy sleeves are to be inserted in a

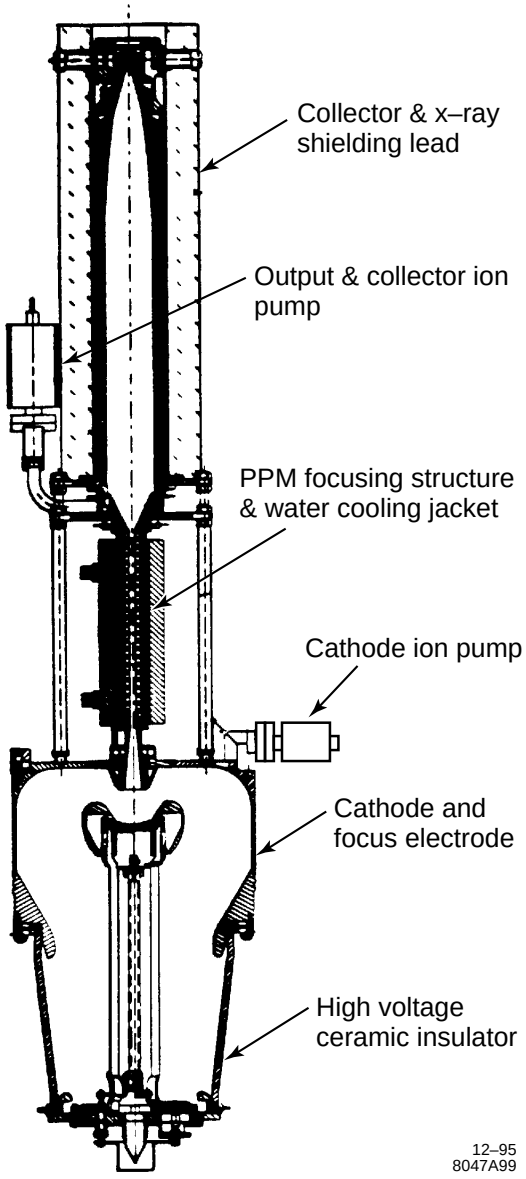

Figure 8-38. *PPM-focused "beam stick" which simulates the X5011 without rf drive. Transmission will be tested with and without flux through the cathode by means of separately tunable electromagnets (not shown).*

modified 5045 klystron to determine whether there are any deleterious effects, and whether any improvement can be detected. A pair of sleeves ground from single-crystal doped silicon having a resistivity between 1 and 4 Ω-cm have been procured. Should there be no deleterious effects, the experimental tube will be placed in a nonsensitive area in the accelerator gallery where many thousands of hours of testing can be observed. In the meantime, we will proceed with testing this increased oscillation damping loss in one or more future experimental X-band tubes.

Diffusion Bonding. Diffusion bonding of the individual cavities which make up the klystrons may result in a significant reduction of manufacturing cost. Diffusion bonding is somewhat complicated in the case of the klystron because of the need to bond spacers and pole pieces which are of different materials (monel or copper for the spacers and iron for the pole pieces). These materials also have different thermal coefficients of expansion. An experimental program, intended to develop the process technology (varying temperature, pressure and time) to obtain strong, reliable, vacuum-tight bonds has been launched. Diffusion bonding of a short stack of copper spacers and copper-plated, iron pole pieces of the type to be used on the PPM test diode has been carried out. This work has already demonstrated that vacuum-tight bonds can be made using this bonding technique.

Upgrading Performance

The upgrade to 1-TeV center-of-mass energy requires a 75-MW peak power klystron. The preliminary electrical and mechanical design of the 75-MW klystron, designated X7511, has been carried out. This includes rf simulations which show 60% operating efficiency. The criteria applied in the design were not to exceed the design limits imposed on the 50-MW klystron and, to the greatest extent possible, stay within the gradients and stress levels demonstrated in the X5011.

These restrictions ruled out simply increasing the beam voltage, which would exceed the self-imposed 500-kV limit while also increasing cathode current density and electron gun gradients to unacceptable levels. To stay within the 500-kV beam voltage limit, it was necessary to increase the beam microperveance from 0.6 to 0.75. To maintain cathode current density, the cathode diameter was increased from 5.72 cm to 6.75 cm. Finally, in order to maintain a realizable cathode area convergence and stay within the capability of existing permanent magnets, it was necessary to increase the diameter of the beam tunnel from 0.95 cm to 1.08 cm.

With these changes, cathode current density and gun gradients are approximately the same for the two tubes. Also, a common set of magnets will focus both beams. Based on 2.5D computer simulations, the rf efficiency drops by only 2 percentage points from 63% to 61%. Because of the reduction in repetition rate from 180 Hz to 120 Hz and a small decrease in pulse length, the average power required of the two klystrons is the same. The margin provided by the rf output window, which has demonstrated 100-MW peak power capability, remains adequate. Table 8-10 summarizes the design and performance parameters for the X7511 PPM-focused klystron.

8.4.4 Manufacturing

Because of the large numbers of klystrons required during the NLC construction phase, the cost of manufacturing and testing each tube is significant to the feasibility of the NLC project. Diffusion bonding is one example of possible cost reduction. The substitution of a low-cost oxide cathode for the present dispenser cathode is another possible cost reduction. After completion of the NLC, monthly tube replacement during operation is estimated to be at least 15 times that of the SLC. On-site production and test capability must be considered in detail. Automation of klystron construction and testing, as well as the accelerator structure construction and testing, is key to the economics of the overall project.

Parameter	Units	Value
Electrical:		
Frequency	(GHz)	11.424
Peak Power	(MW)	75
Beam Voltage	(kV)	490
Beam Current	(A)	255
Beam Microperveance	(μA/V$^{3/2}$)	0.75
Gain	(dB)	57
Bandwidth	(MHz)	100
Beam Modulation		Cathode Pulsed
Pulse Duration	(μs)	1.0
Rep Rate	(Hz)	120 (180 for NLCTA)
RF Efficiency	(%)	60
Cathode Current Density	(A/cm^2)	7.4
Heater Voltage	(V)	15
Heater Current	(A)	27
Mechanical and Magnetic:		
Beam Focusing		Periodic Permanent Magnet (PPM)
Tube Weight	(kg)	32 (without lead)
Tube Length	(m)	1.3
Cathode Diameter	(cm)	6.75
Cathode Half Angle	($^\circ$)	29
Beam Area Convergence		124

Table 8-10. *Design and performance parameters for the X7511 klystron.*

An "Alliance for the Advancement of Robotics Technology" (AART) has been set up among several DOE National Laboratories which seeks to foster collaborative research ties between these organizations. The AART has agreed that its first project is to study the concept of building an NLC klystron factory relying on robotic machining, cleaning, inspection, assembly, brazing, processing and testing of klystrons. With funding of the study provided by both the DOE and DOD, the work will include a complete design and cost analysis.

8.5 Klystron Pulse Modulator

Each high-power rf station includes a pulsed energy delivery system that is tightly integrated in design with the beam generation section of the klystron, and a high-efficiency power supply for charging the PFN (pulse forming network) capacitance. A preliminary design is shown in the diagram in Figure 8-39.

The subsystems of each rf station, discussed in this section, include a single-thyratron Blumlein modulator (Section 8.5.2) driving two PPM-focused klystrons, the modulator power supply (Section 8.5.3), and the station-cooling and oil-circulation systems (Section 8.5.4). The protection systems will be discussed in Section 8.7. All of these subsystems are closely interlinked.

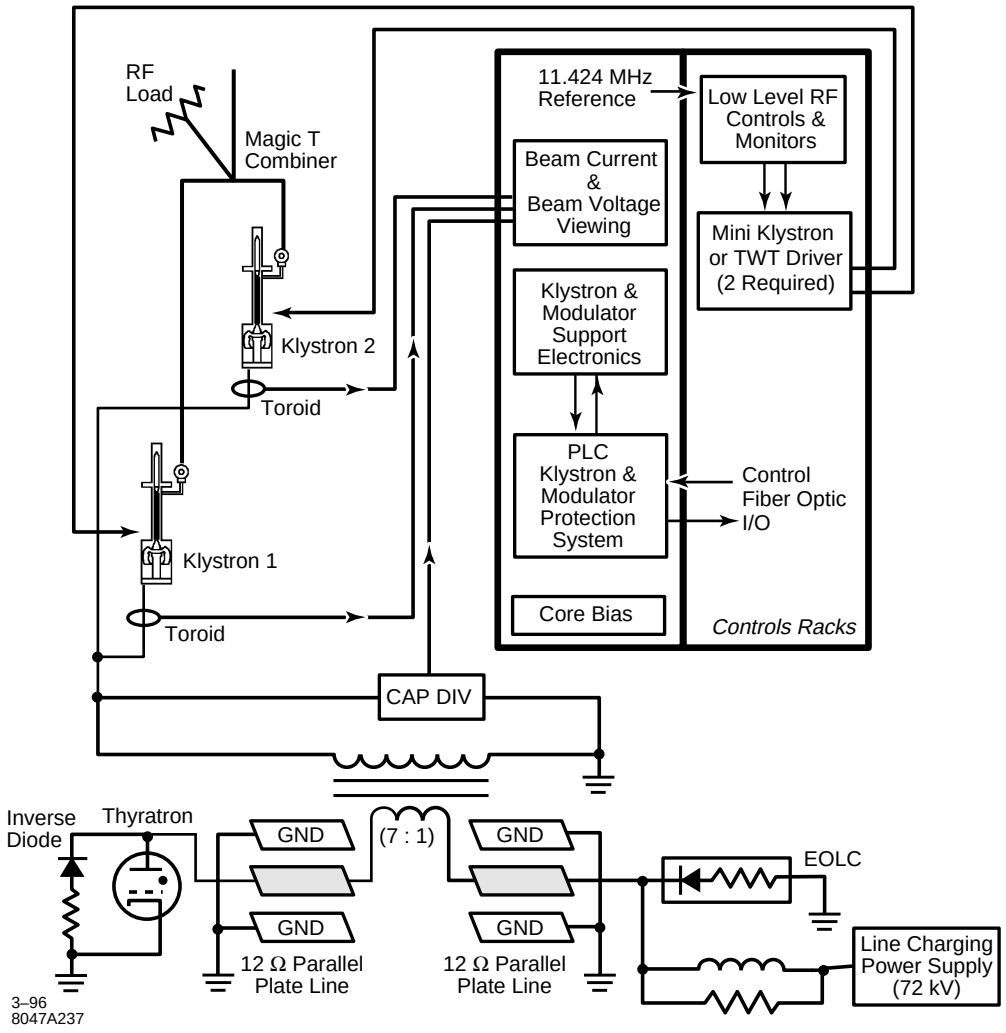

Figure 8-39. *NLC RF Station Block Diagram*

There is much basic research and development that must be accomplished to characterize a final system that will maximize efficiency at minimal cost, and will be reliable and serviceable. Some elements of a program for developing prototype modulator components are outlined in Section 8.5.6. In the meantime, modulator performance can be estimated through simulations. These simulations are based on the best knowledge available for modulator components, in particular the pulse transformer. Simulation examples are given in Section 8.5.5; these are used to obtain the efficiency estimate for the NLC modulator design goals as shown in Table 8-11.

8.5.1 Modulator Requirements

Specifications for the NLC modulator are given in Table 8-11. These specifications are driven by the requirements of the NLC klystron, as listed in the first part of the table. Although the initial design goal for this klystron is an

output power of 50 MW, as required by the 500-GeV NLC design, an improvement program is in progress which will eventually increase the power output to the 75 MW required for the 1-TeV upgrade. The modulator must therefore be capable of driving two klystrons at this higher power level. The repetition rate for the initial 500-GeV NLC design is 180 Hz. To save AC power, this drops to 120 Hz for the later 1-TeV machine. However, during the transition to the higher energy, there may be a mix of 50-MW and 75-MW klystrons on the linac, operating at 180 Hz. In fact, the higher power tube may be available even at the time construction begins on the 500-GeV collider. In either case, the modulator must be capable of driving the higher-power tube at the 180-Hz repetition rate.

The first two columns in Table 8-11 list the design goals for the 50-MW and 75-MW klystrons, and a corresponding set of parameters for a modulator capable of driving two such klystrons. However, as mentioned above, the 75-MW klystron and the modulator must also be capable of operating at a 180-Hz repetition rate, as reflected in the third column of Table 8-11. The efficiency of the 75-MW klystron may also fall short of the 60% efficiency goal, at least initially. To be conservative, the modulator parameters have therefore been chosen so that the modulator can drive a klystron with an efficiency as low as 55% to the required 75-MW output power.

A key consideration for a modulator in a linear-collider application is the efficiency with which power is transferred from the AC line to the klystron beam power in the flat-top portion of the high-voltage output pulse. A 1% decrease in efficiency at any point in this efficiency chain results in an increase by between one and two megawatts in the AC line power required for the NLC rf system. An important component in this efficiency is the ratio of the useful energy in the flat-top portion of the pulse to the total pulse energy, including the energy in the rise and falltime portions of the pulse. This rise- and fall-time energy efficiency is given (very roughly) by the ratio $\mathrm{T}_K/(\mathrm{T}_K + 1.1\mathrm{T}_R)$, where T_K is the flat-top pulse width and T_R is the rise time (the constant 1.1 depends on the precise definition of rise time). In turn, the rise time is determined in large part by the physical design of the pulse transformer, and in particular by the leakage inductance (due to imperfect coupling between the primary and secondary windings). In practical pulse transformer designs, it is observed that the leakage inductance tends to decrease as the transformer turns ratio is decreased. However, a lower transformer turns ratio implies a higher value for the charging voltage for the pulse-forming network (PFN), and a correspondingly high hold-off voltage for the thyratron and other high-voltage components. For a modulator using a standard PFN design which can deliver a 500-kV output pulse, this charging voltage would be about 145 kV for the 7:1 pulse-transformer turns ratio listed in Table 8-11. However, by using a Blumlein-type of PFN, the charging voltage can be reduced by a factor of two to about 72 kV. Although a Blumlein PFN design is somewhat more complex, it makes possible both a low pulse-transformer turns ratio and a reasonable value for the charging voltage.

In a standard modulator design with output pulse lengths longer than a microsecond or so, lumped elements (capacitors and inductors) are used for the PFN. Such a lumped network has the advantage that it can be readily tuned to adjust the pulse shape, although it is still difficult to eliminate all of the ripples to attain a truly flat pulse unless a very large number of elements are used. Also, it is difficult and expensive to manufacture pulse capacitors with a very low series inductance and long life, especially when the polarity must reverse during the pulse, as required by the Blumlein configuration. For these reasons, the use of lengths of smooth transmission line (termed here a pulse-forming line, or PFL) is being proposed for the NLC modulator. The major disadvantage of such lines (long length) can be ameliorated by choosing an appropriate packing geometry and good mechanical design (Section 8.5.2).

The rise- and fall-time efficiency is the major component which determines the overall modulator efficiency. In addition, a voltage drop across the thyratron, eddy currents and hysteresis losses in the transformer core, and resistive losses in the transformer windings and connecting leads contribute an additional loss of several percent. The charging voltage on the PFL must be slightly higher (about 1.5%) to compensate for these losses. The corresponding loss in efficiency (97%), multiplied by the rise- and fall-time efficiency, gives the net efficiency with which energy stored in the capacitance of the PFL is transferred through the pulse transformer into the useful flat-top portion of the output pulse. A discussion of the projected efficiency for the NLC modulator design, based on simulations of the output pulse shape is given in Section 8.5.5.

Description: Blumlein PFL configuration with individual line-charging power supply and 7:1 pulse transformer turns ratio.			
	50-MW Klystrons	75-MW Klystrons	Design Min/Max
Klystron Parameters:			
Klystron Peak Output Power (MW)	50	72	
Klystron Microperveance (μperv)	0.60	0.75	
Klystron Beam Voltage (kV)	465	490	
Klystron Efficiency (%)	57	60	55 Min
RF Pulse Width (μs)	1.2	1.0	
Repetition Rate (Hz)	180	120	180 Max
Modulator Parameters:			
Output Pulse Voltage (kV)	465	490	510 Max
Output Pulse Current, for two klystrons (A)	380	510	550 Max
Flat Top Pulse Width (μs)	1.2	1.0	
Repetition Rate (Hz)	180	120	180 Max
Pulse Flatness (%)	1	1	
PFL Voltage (kV)	68	71	75 Max
Est. Energy Transfer Efficiency[a] (%)	77.5	80.5	76 Min
PFL Stored Energy (J)	274	310	370 Max
Pulse Energy Width (μs)	1.5	1.2	
Pulse Rise Time (ns)	275	175	
Thyratron Current (kA)	5.3	7.15	7.7 Max
PFL Impedance[b] (Ω)	12.4	9.9	9.7 Min
Auxiliary AC Power[c] (kW)	2.2	2.3	2.5 Max
Est. Power Supply Efficiency (%)	93	93	92 Min
Net Modulator Efficiency (%) (excluding auxiliary power)	72	75	70 Min
AC Input Power (kW) (excluding auxiliary power)	53	40	72 Max

[a] See Section 8.5.5. The energy-transfer efficiency is given by the rise- and fall-time energy efficiency times a series loss efficiency (97% is assumed here).

[b] Adjusted to match impedance of production klystrons.

[c] Includes thyratron heater, thyratron reservoir, and klystron cathode heater supply.

Table 8-11. *Klystron-modulator specifications (two klystrons per modulator).*

8.5.2 Pulse Modulator Design Outline

The pulse modulator described in the section below is presented as an example of a design that is physically realizable with present design technology or modest extensions to that technology. In Section 8.5.6, an R&D program is outlined whose results will undoubtedly change this design.

The station klystron modulator drives two PPM-focused klystrons. The modulator is of the Blumlein type, and uses as its energy storage elements distributed-type transmission lines rather than lumped element artificial lines. The design is driven by the need to synthesize the klystron cathode pulse with the highest efficiency consistent with reasonable cost. In a modulator, the major areas where energy is lost are in the rise and fall times of the cathode pulse where energy is dissipated, but no useful rf energy is produced, and in the IR drops and capacitive and inductive stored energy that is dumped after each pulse ends. There is also the power lost in the thyratron voltage drop, and the energy necessary to operate the thyratron heater and reservoir.

In a thyratron-PFN modulator, the element determining the rise time is usually the pulse transformer. Because of the voltage hold-off necessary between the primary and secondary of the transformer, there is always leakage flux generated by the primary that does not couple to the secondary. This shows up as leakage inductance in series with the primary which limits the voltage rise time of the secondary. There is a minimum stray capacity associated with the klystron cathode, and the high-voltage secondary of the pulse transformer. This capacity must be charged on each pulse, and the charging energy is lost during each pulse fall time. The transformer core does not have infinite magnetic permeability, and so a real inductance which is not infinite appears in parallel with the primary of the transformer. This has the effect of lowering the load impedance as a function of pulse length, leading to droop at the tail end of the pulse. The transformer leakage inductance can be minimized by keeping the pulse transformer turns ratio as low as possible. A low ratio dictates a high-primary pulse voltage, and the primary voltage is limited by the switching capability of the thyratron and the voltage holdoff of the pulse forming line.

In the standard-design modulator, a single PFN switched by a single thyratron drives a high-ratio (typically 23:1) pulse transformer. A modulator using this conventional design was optimized for efficiency and minimum rise time in the Test Stand 13 position in the Klystron Test Lab at SLAC. The rise time was less than 600 ns. This is typical of conventional design technology. A modulator design in which two PFNs are used, charged in parallel, and discharged in series (called the Blumlein design) allows the use of a low ratio (7:1) pulse transformer and a thyratron with reasonable voltage hold-off capability. In a lumped element PFN, internal inductance in the capacitors limits the shortness of the rise time that can be obtained. If a distributed transmission line is used instead of the LC lumped line, this limit can be circumvented. Figure 8-40 shows the simple Blumlein modulator concept using two 10-Ω distributed lines, a 75-kV thyratron, and pulse transformer with a 7:1 turns ratio and a primary impedance of 20 Ω. This circuit can provide a pulse rise time of less than 300 ns, delivering a 490-kV pulse of about 500 A to drive two 75-MW klystrons.

The Blumlein pulser circuit as shown in Figure 8-40 operates as follows:

1. A capacitor-charging power supply charges both inner plates of the two lines to a DC potential of +72 kV. The two inner plates and the primary of the pulse transformer are now at a +72-kV potential.

2. The thyratron is triggered and presents a short circuit to the left end of the left transmission line. The 10-Ω transmission line presents to the thyratron a voltage source of 72 kV in series with an internal impedance (line characteristic impedance) of 10 Ω. The current in the thyratron is thus 7.2 kA. In order to match the current and voltage conditions at the thyratron after switching, a -72-kV, 7.2-kA wave must be launched traveling to the right on the transmission line. After a time T (where T is the electrical length of the line), this wavefront reaches the end of the line at the connection to the pulse transformer. There it sees a load impedance of 30 Ω (the pulse transformer primary in series with the 10-Ω impedance of the second line). From transmission line theory,

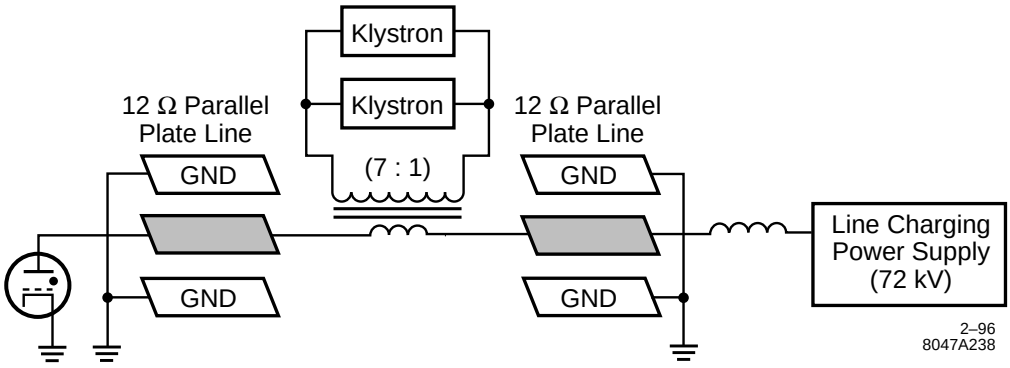

Figure 8-40. *NLC modulator Blumlein schematic.*

this mismatch launches a reflected wave of -36 kV, which travels back toward thyratron carrying a current of 3.6 kA.

3. The remaining current in the initial wave ($7.2\,\text{kA} - 3.6\,\text{kA} = 3.6\,\text{kA}$) will start to flow through the primary of the pulse transformer at time $t = T$. It will also launch a wave with an amplitude of -36 kV traveling to the right in the second transmission line. The net voltage at the right side of the transformer primary is $72\,\text{kV} - 36\,\text{kV} = +36\,\text{kV}$. The net voltage drop across the primary is therefore 72 kV (also given by $3.6\,\text{kA} \times 20\,\Omega$). The transformer output voltage is this voltage drop times the 7:1 turns ratio, or about 500 kV.

4. The two -36-kV waves, traveling to the left on the first line and to the right on the second line, leave behind them voltages of -36 kV and $+36$ kV, respectively. Note that the polarity has reversed on the first line; this reversal imposes an additional burden on the design of pulse capacitors for Blumlein networks.

5. After a second period T, the two waves reach the left and right ends of their respective transmission lines. At that time a reflected wave of $+36$ kV (short circuit termination) is launched in the first line, and a -36-kV wave (open circuit termination) is launched in the second line. These waves travel back toward the pulse transformer during a third period T, and wipe out all the remaining energy stored in the two lines. At time $t = 3T$, the waves reach the pulse transformer and cancel the current flowing in the primary.

Distributed energy storage lines are most familiar as coaxial cables. There are many low-power applications where coaxial cables are used for smooth-pulse energy discharge. At high power, there is a good technology development in water-filled pulse lines for very short pulses at low impedance. These water-filled energy storage lines make use of the very high dielectric constant of pure water, $\epsilon_r > 80$, but they must be charged very rapidly because water as a dielectric cannot withstand high electric fields for more than tens of microseconds before it becomes lossy. An oil-filled line with high dielectric oil ($\epsilon_r = 7$) can in principle hold off a high voltage, but the support structure of the inner coaxial element is subject to creepage breakdown. For the NLC application, physically realizing a 10-Ω distributed line as a coaxial cable requires a very large diameter cable, since high-voltage creepage across the inner support insulator would otherwise limit the charging voltage. Any breakdown across the inner support insulator would be difficult to repair or replace.

An oil-filled five-layer parallel plate transmission line as shown in Figure 8-41, is physically realizable and relatively easy to manufacture and repair. The structure as shown contains two lines of 10-Ω impedance each. The dielectric constant of the oil is just that of normal transformer oil, 2.6. The oil containment for the transmission line is shown as separated from the klystron and pulse transformer oil so that high-dielectric ($\epsilon_r = 7$) oil can be considered in the design development or upgrade. Note that with normal transformer oil, $\epsilon_r = 2.6$, the transmission lines shown match klystrons of 0.6 μperv. By increasing just the dielectric constant of the oil, lower impedance lines result that can match

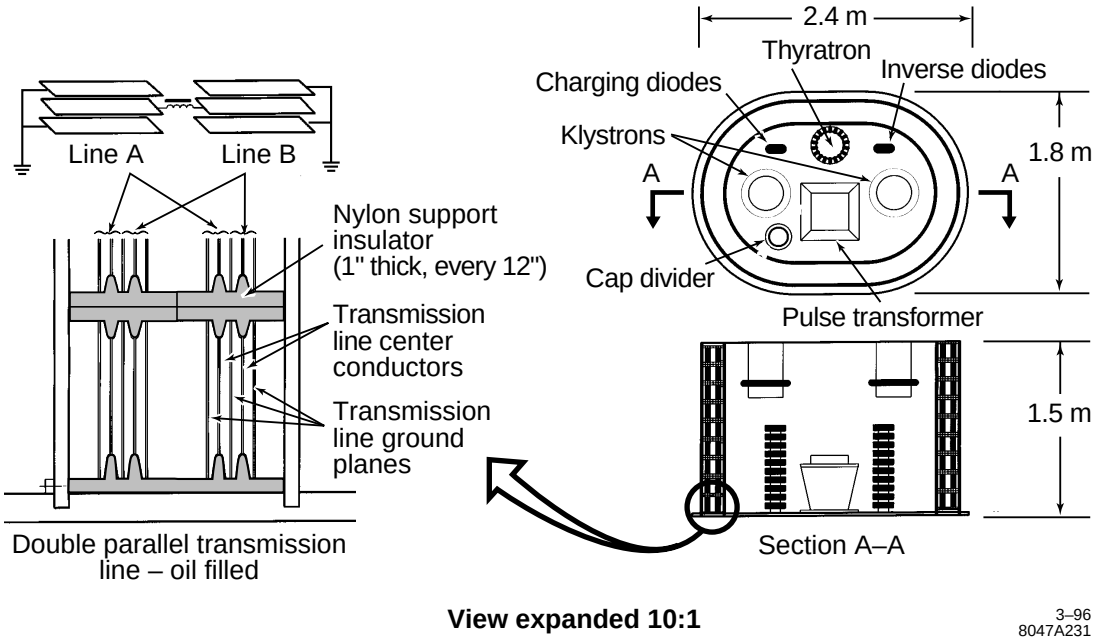

Figure 8-41. *NLC modulator tank assembly showing two klystrons, thyratron, pulse transformer, and two multilayer plate transmission lines.*

higher perveance klystrons. These lines would also be electrically longer by the square root of the dielectric constant ratio.

A proposed modulator tank supporting two klystrons is shown in Figure 8-41. The parallel plate transmission lines are shown mounted in the space between the inner oil tank and the outer containment tank. The total length of this double transmission line assembly is about 460 ft. The oil is contained in an aluminum racetrack-shaped inner tank that also serves as the support for the transmission line assembly. The transmission line assembly consists of continuous aluminum strips supported by molded nylon support insulators approximately one-inch-thick spaced at 12-in intervals. This construction allows easy servicing and repair of the pulse line if an arc destroys one of the support insulators. By supporting the parallel plates from the end of the aluminum strips, the creepage path between the plates can be made long enough to prevent discharge while still keeping the plate-to-plate gap small enough to take advantage of the greater breakdown properties of the oil.

There are a number of secondary elements also housed in the modulator tank: the end-of-line clipper diode stack, the charging diode (if one is used), the current viewing transformers and voltage viewing capacity divider, the core reset inductor, and the thyratron inverse clipper diode. All of these elements are contained in the inner tank adjacent to the thyratron and pulse transformer.

A double-rack enclosure adjacent to the modulator tank contains all the support electronics for the modulator, and the rf-drive electronics. The support electronics includes the klystron cathode heater supply, the thyratron cathode supply, the thyratron reservoir supply, the control power distribution, the rf low-level driver and interlock system, and a custom designed programmable logic controller (PLC) that provides the control and monitor functions for both the pulse modulator and the klystron rf drive and protection systems. Depending on the construction design, this set of racks may also contain the primary capacitor charging power supply.

Charging Voltage	72 kV
Pulse Forming Line Capacitance	0.12μF
Joules/pulse, 2 klystrons	310
Repetition Rate	180 pps at 500 GeV; 120 pps at 1 TeV
Charging Voltage Regulation	0.1%
AC Line	480 V, 3-phase, 60 Hz
AC Line Stability	3%
Power Supply Efficiency	93%

Table 8-12. *Charging power supply specifications.*

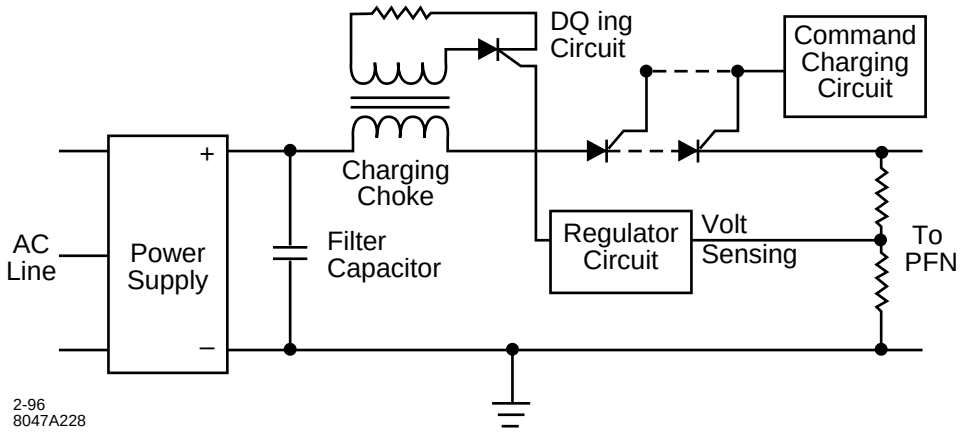

Figure 8-42. *Conventional PFN charging power supply.*

8.5.3 Charging Power Supply Design Outline

Specifications for 500-GeV Operation

The power supply that charges the PFL must fulfill the requirements shown in Table 8-12.

Conventional Charging System

Traditionally, the power supply that charges the PFL capacitance consists of an AC to DC power supply, a filter capacitor bank, a charging choke, a charging diode or a command-charging SCR circuit, and de$Q$ing circuit that regulates the PFN charging voltage (Figure 8-42).

If we assume an AC line stability of 3%, then we must de$Q$ at least 6% to meet the regulation requirements. If the de$Q$ing power is dissipated, the efficiency of the power supply charging system is diminished. An energy recovery scheme could be developed to recover the energy and feed it back to the power lines, but it would be expensive and would only recover a portion of the energy. With energy recovery, we could only achieve a total power supply efficiency of about 90%. The output voltage could also be regulated by using a primary SCR line regulator instead of the de$Q$ing circuit.

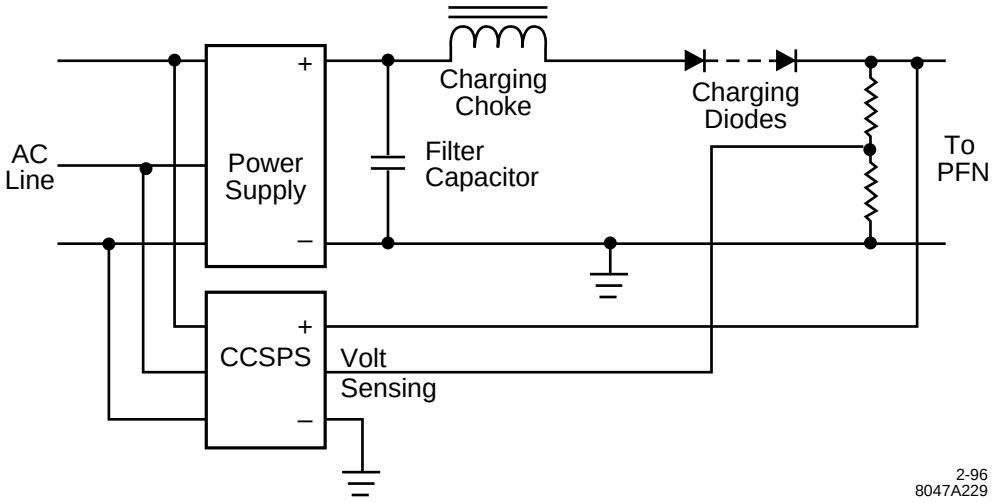

Figure 8-43. *Hybrid circuit consisting of a conventional power supply and a small capacitor charging switching power supply (CCSPS) in parallel.*

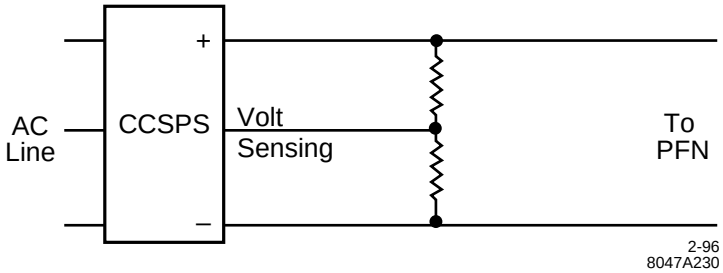

Figure 8-44. *Capacitor charging switching power supply (CCSPS) scheme.*

Hybrid Charging System

A better scheme would be to use a small capacitor charging switching power supply (CCSPS) in parallel with the charging choke output (Figure 8-43). At the lowest line voltage, the PFN would then be charged to 94% of its peak voltage by the charging choke, and the switching power supply would be used to charge the final 6% of the voltage. What we have done is substitute an additive process for a subtractive one with a resulting increase in efficiency. With this additive scheme, power supply efficiency could be as high as 93%.

Capacitor Charging Switching Power Supply System

An even more attractive idea is to use a CCSPS to charge the PFN directly (Figure 8-44). The charging cycle starts with the PFL capacitor at zero volts. The CCSPS starts charging the PFL at constant current until the desired voltage is reached. At that time, the supply becomes a constant-voltage power supply and keeps the PFL charged at the desired value. The charging waveform looks like a linear ramp which flattens out at the desired voltage.

The CCSPS supplies are becoming commercially available now and will be common in the near future. A single 50-kV power supply is presently available which will charge the PFL to 50 kV at 120 pps, will tolerate a voltage reversal of

20%, and has an efficiency of approximately 93%. Research is required to increase the charging voltage to a minimum value of 72 kV. To be able to charge at 180 pps, two CCSPSs, operated in parallel using master/slave connections, are required.

This solution will greatly simplify the charging circuit topology since there is no need for a filter capacitor bank, charging choke, command charging circuit, and high-voltage blocking SCR strings. The elimination of the filter capacitor bank reduces the amount of energy storage and the possibility of thyratron damage in a latch-up condition (when the thyratron fails to turn off, or breaks down during PFL charging). With a filter capacitor bank, a false trigger or a thyratron breakdown will cause the filter bank to discharge completely through the thyratron, and the power supply will then short circuit itself through the thyratron. With the CCSPS, a thyratron breakdown would only result in a maximum current equal to the nominal charging current since the CCSPS reverts to constant current operation when it is short circuited. As an additional advantage, the CCSPS is much more compact than a conventional power supply. For example, the 50-kV supply cited is rack mountable, $19''$ wide, $22''$ deep, and only $12.25''$ high.

Other manufacturers have built power supplies of this power level, housed in a single chassis and having an efficiency of approximately 85%. Additional development is needed to increase the efficiency and to develop a reliable 75-kV supply.

8.5.4 Station Cooling System and Oil Circulation

There are several cooling circuits that remove heat from the klystron and modulator. The klystron has just one water cooling circuit that is a combination of all the passages in the klystron. Temperature monitor points on parts of the klystron (body, anode, collector, etc.) provide interlocking for over-temperature conditions. The modulator contains two oil systems, one for the transmission lines oil which may have a higher dielectric than the main tank, and the other for the low-dielectric oil for the klystron guns, the thyratron, the end-of-line clipper (EOLC) and charging diodes, and the pulse transformer. Each of these systems will have a small oil-circulation pump and an oil-to-water heat exchanger appropriately interlocked.

There is no cooling required in the rf system support racks unless the charging power supply is mounted in these racks and it needs water cooling. There may be a need for water temperature stabilization if the rf components cannot be made to be phase-stable with temperature changes.

8.5.5 Simulations and Efficiency Projections

At the time of this writing, the efficiencies of the various components and subsystems are being analyzed, and the numbers will become clearer as R&D progresses. Pulse response simulations based on projected parameters of various lines, discrete capacitors, and pulse transformers are shown in this section.

Distributed Blumlein

There have been several preliminary network simulations run, using the program ISPICE, which show the general waveshapes on a Blumlein circuit using one or several segments of transmission line, as shown in Figure 8-45. By using several segments of varying impedance, the voltage at the tail of the pulse can be boosted to compensate for transformer droop. A simulated pulse shape is shown in Figure 8-46 for the case of a modulator driving a 50-MW

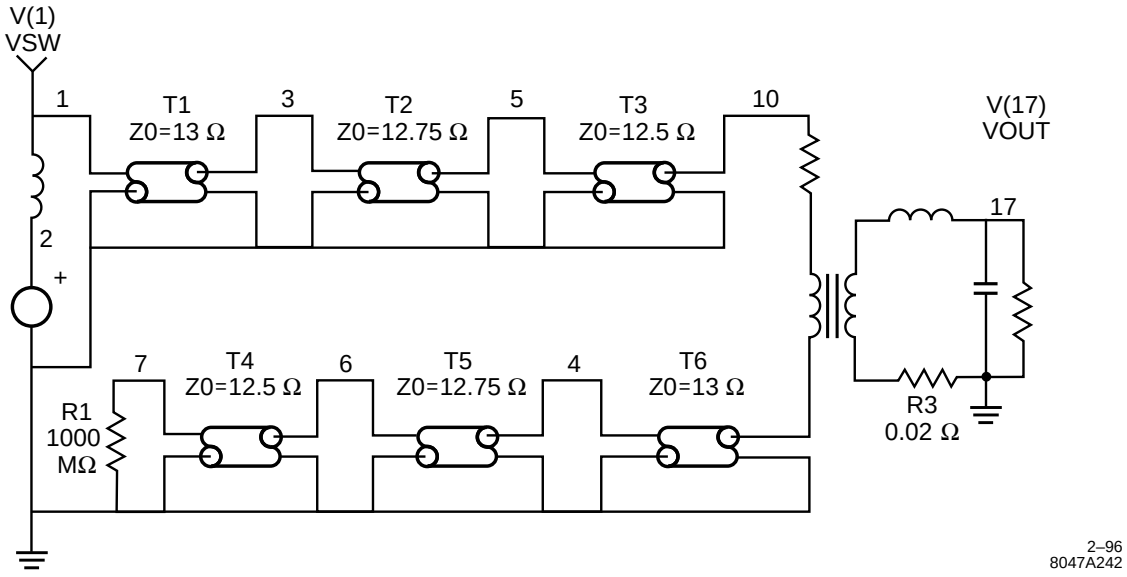

Figure 8-45. *Example of a three-section Blumlein circuit.*

klystron at 465 kV. The flat-top pulse length is about 1.4 μs, the rise time is about 250 ns, the energy efficiency is about 83% and the peak-to-peak ripple about 2%.

More detailed simulations are planned to look at waveshapes using more complex equivalent circuits that approximate real lines and pulse transformers. All the secondary parameters such as klystron stray capacity, the real characteristics of the various diode stacks and monitor elements, and the actual characteristic of a switched thyratron will be added to the model to get a better picture of what the real pulse response will be.

The dielectric constant of the various normal and high-dielectric oils must be characterized as a function of frequency, including dielectric losses, since the propagation of the wavefront on the lines will be limited by these parameters. High frequency losses limit the wavefront rise time, and dielectric constant variations with frequency can smear out the rise time, and cause pulse overshoot if all frequency components of the wavefront do not arrive at the end of the line at the proper times. It will take more development work with a simulation program to allow the dielectric constant to have a real and imaginary part corresponding to loss and propagation velocity.

Discrete Element Blumlein

While smooth distributed transmission lines are attractive substitutes for lumped element lines with discrete capacitors, there are some advantages to using lumped elements, especially if the capacitors can have high-energy storage density, low inductance, and easy manufacturability leading to low cost. Strontium Titanate (ceramic type) capacitors have high-energy storage density, and because they can be automatically manufactured, can have very low per-unit cost. A lumped element line using as many as two hundred elements can approximate the characteristics of a smooth oil-filled line, but can be packaged into a much smaller volume because of the high energy storage density in the Strontium Titanate dielectric. Much R&D will be necessary to physically realize such a line and to produce low-inductance capacitors.

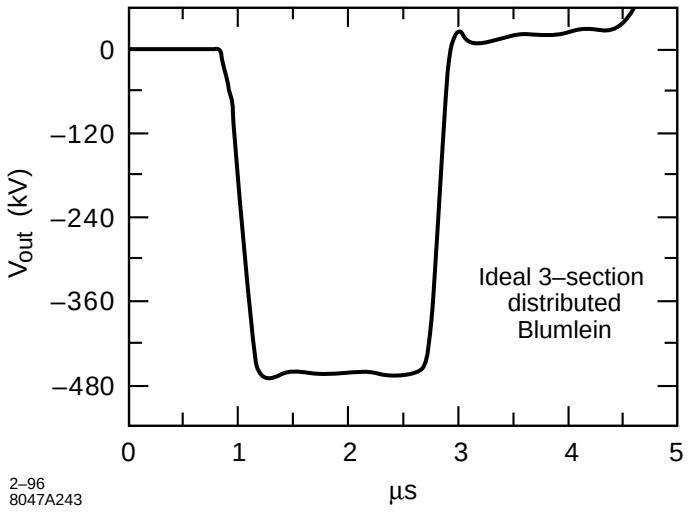

Figure 8-46. *Voltage pulse obtained from simulation of an ideal three-section distributed Blumlein.*

8.5.6 Prototype Modulator Development and Performance

In the Klystron Test Lab at SLAC, there are two modulators which can give some experimental check points to compare with simulations. Test Stand 13 is a high-power conventional modulator which contains close-coupled PFNs and a direct connection to a 23:1 pulse transformer. It produces 550-kV pulses driving a 1.8 microperveance klystron for a 3-μs flat-top pulse.

Test Stand 3 contains a three-section Darlington line modulator driving a 6:1 pulse transformer with all primary pulse-forming elements in one large oil tank. It also is designed to produce 600-kV pulses, but it has not run at full voltage in oil as yet. The capacitors that make up the three PFNs have too much series internal inductance to allow a very fast rise time, flat-top pulse. Additional testing will be done on this modulator to get better data. This test stand will be used as the location for new R&D work on distributed and lumped element pulse line modulators.

As the paper design of a possible NLC modulator evolves, the R&D areas where the new ideas must be tested start to surface. At the present time, we can divide the R&D effort into two categories: System concept development, and component and subsystem design and testing.

System Concept Development

Conventional klystron beam-delivery pulse-modulator systems proceed in design with microwave-oriented klystron engineers developing the klystrons, and electronics-oriented modulator engineers designing modulators to meet klystron specifications. While this cooperative effort can sometimes produce well-coordinated results, more often performance, cost, and efficiency savings are lost in the interface process. By considering the klystron beam formation design as an integrated system with the pulse transformer and primary pulsed energy storage system, trade-offs can be made at an early stage in the design development resulting in a better optimized system.

New concepts can be considered when the system is an integrated whole. As an example, the klystron interface with the pulsed high voltage is traditionally a large, cylindrical ceramic interfacing the high vacuum of the klystron to the oil insulation of the pulse transformer tank. Consider the advantages of a pulse tank under high vacuum instead of

being filled with oil. With vacuum on both sides of the klystron cathode seal, the seal can be redesigned to be smaller, radial rather than cylindrical, and much easier to manufacture. The capacity of the gun structure decreases because of the smaller cathode system, and the absence of high dielectric oil. Inside the tank, the pulse transformer size might be reduced because of the better insulating properties of high vacuum. This smaller size, together with the lower dielectric constant, would reduce the distributed capacitance between windings and other stray capacitances, and possibly also the leak inductance. All these reductions in stray energy storage work to decrease the rise and fall times of the cathode pulse, the whole system becomes more efficient.

To physically realize such a system, new R&D on a variety of components and subsystems must be conducted. These efforts are included in the proposed R&D program outlined below.

Component and Subsystem Design and Testing

In the component and subsystem area, R&D programs are needed to develop both oil-immersed and high-vacuum systems. Efficient charging supplies are a separate area of R&D where cooperation with industry should produce reliable, high-efficiency units that can be adapted for large-scale production. Some of the pulsed energy storage and delivery development efforts are as follows:

Thyratrons: The present design of two- and three-gap thyratrons is well advanced and with minor modifications can meet the needs of the NLC pulsed power switch. Long cathode life, on the order of 50,000 hours, has been achieved with a large dispenser cathode and increased-size hydrogen reservoirs. The R&D effort for thyratrons includes mechanical packaging for low-cost fabrication and quick changing in the field, and the reduction of power needed to heat the cathode and hydrogen reservoirs. This can be done as a joint effort with industry. We are fortunate in having at least three interested thyratron manufacturers with the skills and facilities to enter this development and optimization process.

Distributed Energy Storage Lines: Several different energy storage lines have been suggested, including oil-filled Andrews cable, either coaxial or triaxial, and the parallel plate open network described earlier. The oil dielectric-medium used in these lines requires further study to understand the breakdown properties and the dispersive characteristics of the various oils and other possible dielectric liquids.

The lines themselves need further detailed mechanical and electrical design analysis, including building some full-voltage test models to see how these lines perform. The manufacturability, fabrication cost, and maintainability of such lines must also be studied.

Lumped Element Quasi-distributed Storage Lines: Strontium Titanate (ceramic) high-voltage capacitors have very large energy storage density and in quantity are simple to manufacture. The temperature coefficient is rather large, but in a temperature stabilized oil environment, this drawback is not severe. A quasi-distributed energy storage line can be physically realized with as many as 100 elements which looks much like a distributed line, but is much smaller. R&D would be conducted on examples of this type of line to establish the feasibility of using it for the NLC pulsed power storage.

Pulse Transformers: Since all the pulsed energy storage systems envisioned for the NLC operate below 100 kV, a pulse transformer is required to transform the low-impedance line pulse to the higher impedance 500-kV level needed by the beam-forming elements of the klystron. Traditionally, this pulse transformer has operated in oil for insulation. The core material has been 2-mil tape-wound iron. Improvements can be made in pulse transformers both in the winding of the primary and secondary of the transformer, the use of oil versus vacuum insulation in the windings, and in the properties of the core material. This area is central to the R&D effort to produce a more efficient pulsed energy delivery system.

An oil-immersed transformer is fairly well understood. A transformer using high vacuum as the insulation medium is a challenge in that the materials used in the transformer and core are not usually good vacuum elements. However, with some innovative design both for the core and the windings, and for a bare ion pump contained within the pulse tank vacuum enclosure, a significantly improved pulse transformer and klystron cathode high-voltage seal can be physically realized. The resulting klystron and pulse transformer tank package would be much smaller and lighter than the present 5045 klystron assembly, and would look more like the early-generation, SLAC XK-5 klystron, without the barrel permanent magnet.

Primary Materials Developments: Improvements in the understanding of performance and limitations of basic materials such as insulators, oil and general dielectric fluids, and core materials such as iron, nickel alloys, Metglas, etc. are necessary to develop the pulsed-energy storage elements envisioned above. With better understanding of basic material properties, more compact and reliable devices will be developed. The appropriate materials science research will be part of the modulator and klystron development program.

8.6 RF Drive and Phasing Systems

The design of the rf drive and phasing systems for the NLC will be based heavily on experience gained from existing systems developed for the SLAC linac and its 60-GeV upgrade for the SLC, with further extensions based on the design of the NLCTA. The challenges to be met for the NLC arise from its greater length, number of components that must be controlled, required tolerances, maintainability, and reliability. The requirements imposed on the rf drive and phasing systems are summarized below:

- The drive system must provide stable, adjustable, and reliable input power to 4528 klystrons (approximately 1-kW pulsed peak power per tube). The layout of the system must be such that individual subsystem failures do not cause the beam energy to decrease to less than 85% of its operating level. This requirement is dictated by potential collimator and other damage caused by off-energy beams.
- The amplitude of the drive power must be adjustable so as to individually saturate the high-power klystrons.
- The phase of the drive power must be adjustable in several ways:
  - Slowly, to take care of phase drifts and drifts caused by length changes in equipment and terrain. Included here are the couplers, coax lines, intermediate amplifiers, high-power klystrons, SLED-II, waveguide components, and the changes in time at which the bunch trains are injected into the X-band linacs by the S-band bunch compressors.
  - Quickly (within each 1.2-μs klystron rf pulse), to create the proper resultant amplitude and phase profiles necessary to produce the desired fields in the accelerator structures and to place the bunches at the desired phase positions with respect to the X-band waves. These positions are dependent on bunch number and charge, which can change from pulse to pulse, and are dictated by BNS phasing, single bunch and multibunch beam loading, and other considerations.
  - The phasing system design must also include initial adjustments (upon installation) of the waveguide runs which feed the four accelerator sections driven by one pair of klystrons.

The phases of high-power rf fields which act on bunch trains should be adjusted to about 0.5° at 11.424 GHz. A schematic layout of the rf drive and phasing system for the NLC is shown in Figure 8-47.

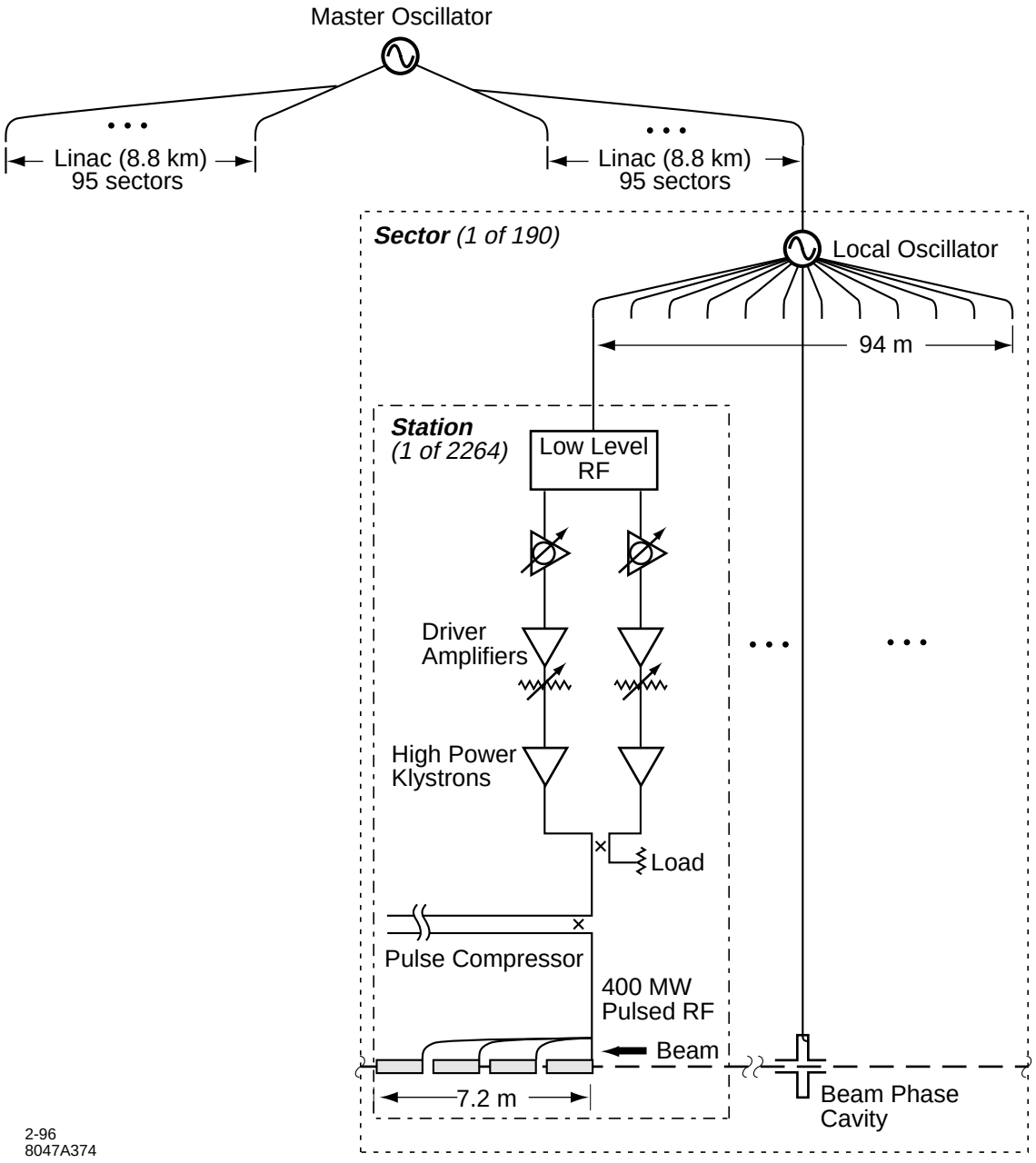

Figure 8-47. *Schematic of rf drive system. The master oscillator provides phase-stable rf to local oscillators in each sector over a fiber distribution system. Local sources in each sector provide 11.424 GHz to each rf station in the sector using coaxial lines. A beam-phase cavity uses the beam to determine the rf phase for optimum operation. Power levels are low (several milliwatts) until the final drive for the high-power klystrons.*

Master Oscillator Quantity: 1	Logical Sectors Quantity: 190	RF Stations Quantity: 2264
• 11.424-GHz reference signal • Fiber optic distribution	• Local oscillator • Beam phase correction • Coaxial rf distribution within sector • 12 rf stations per sector • 94 meters sector length	• One modulator • Two klystrons • SLED-II rf pulse compression (5:1) • Four accelerator sections • Phase coupler for klystron and beam-induced rf • Rf phase detectors

Table 8-13. *Contents and granularity of rf sub-systems.*

8.6.1 Functional Overview

For NLC, the rf system must meet the challenges listed above, while giving the collider control system the tools required to model the machine performance accurately, and to change the operating parameters as conditions mandate. The machine rf requirements and the proposed solutions which follow constitute a proposal to meet these goals.

The sub-systems of the NLC rf drive and phasing systems are shown in Table 8-13 and outlined below. The individual subsystems are fully described in later sections.

The master oscillator for the accelerator generates the accelerator's primary 11.424-GHz reference and uses a fiber-optic based transport system to provide the frequency reference to each sector's local rf source. This signal is used as a diagnostic reference and serves to maintain system stability in the absence of a transported beam.

Each accelerator is divided into 95 sectors of up to 12 rf stations each. The sector size is determined primarily by two operational factors: the practical length of coaxial distribution systems for rf systems, and the requirement of the machine protection system that no single failure of a subsystem result in a destructive, non-transportable beam. For comparison, SLAC has 30 sectors consisting of eight high-power klystron/modulator stations.

Each sector has a local oscillator to generate a harmonically-clean rf signal which is phase locked to the beam for additional stability. This signal is distributed to each station for rf drive and monitoring purposes.

The smallest unit in the accelerator rf systems is the station. Each station consists of a pair of high power klystrons powered by a single modulator. The klystrons are differentially phase modulated to achieve the phase and amplitude control required for SLED-II pulse shape control and to address thermal considerations associated with beam loading (see below). The high power klystron outputs are combined using a four-port power combiner with a high power load on the “unused” quadrature-phase output. The “used” output of the combiner drives a single pair of SLED-II energy compressor delay lines and four accelerator sections.

The amplitude output of the SLED-II compressor is shaped by phase modulation of the two klystrons in order that the power extracted by each electron bunch is exactly matched by the input rf power. In this way all bunches in the bunch train experience equal accelerating gradients. Indeed, the operational goal is to provide an accelerator gradient that will accelerate all bunches equally, allowing for changes in pulse length, shape and total charge.

• The beam energy gain must be stable and understood.
• The rf entering the accelerator must be modulated in amplitude and phase as a function of time to produce the design acceleration of the entire pulse-train. (Transient beam loading compensation was discussed in Section 8.2.3).
• The phase of the rf at the accelerator must be adjustable. Machine operation requires that sectors operate slightly off phase.
• The overall rf amplitude and phase of a sector must be controlled, even in the presence of large changes in beam loading.

Table 8-14. *Basic rf control functions for NLC operation.*

8.6.2 System Functional Requirements and Specifications

The acceleration of long trains of electron bunches places heavy demands on the control and monitoring of each sector's rf sources. The general monitoring and control functions for basic machine operation are listed in Table 8-14. Additional diagnostics and monitoring are required, with some specific items detailed in the sections that follow.

Performance specifications for rf devices, monitoring, and control functions depend on the nature of potential disturbances of the accelerating phase and amplitude, and general beam dynamics considerations. Disturbances with uncorrelated noise spectra ("gaussian processes") act weakly on the beam while disturbances which are strictly correlated across larger sections of the machine have a stronger effect on the beam.

Disturbances which have high frequency components (greater than $1/2\pi T_{fill}$ where T_{fill} is the rf filling time) lead to further relaxation of the tolerances which depends on the power spectrum of the disturbance (see Section 8.2.8) and the characteristics of the SLED-II and accelerator structures. Disturbances with very low frequency components (less than the feedback bandwidth) which are corrected by feedback systems also have relaxed tolerances.

Examples of several rf noise sources for consideration are:

- Errors in SLED-II shaping due to klystron bandwidth limits. These errors have both high and low frequency components, and are correlated and stable.
- Modulator thyratron induced phase and amplitude noise. Thyratrons are the primary source of modulator-induced errors, and are uncorrelated with an intermediate frequency spectrum.
- Local oscillator phase noise. These are broadband and are correlated within a sector.
- Thermally induced phase errors due to changes in average beam current. These have an intermediate frequency spectrum and are strongly correlated among all accelerating devices in the accelerator.
- Thermally induced phase errors due to tunnel temperature changes. These are typically very slow changes and are strongly correlated.

As seen by the above examples, no single set of tolerance values can apply. An interesting metric for gauging a disturbance's effect is obtained by comparing the coherence length of the effect (correlation length of a station, a sector, a linac) to the "interaction length" of the process. The device tolerances may generally be reduced statistically by the square root of the ratio of the interaction length to the coherence length of the disturbance. (For the SLC at SLAC, the effective interaction length is on the order of several betatron wavelengths or, near the injector, the length to achieve an energy gain of several 10's of percent.) Because of this scaling, specifications for station and

Parameter	Accuracy	Stability & Resolution	Units
Energy profile	± 0.5	± 0.1	% voltage
Energy gain knowledge	± 5	± 0.1	% voltage
Phase readback	± 1	± 0.1	degree
Phase stability	N/A	± 0.1	degree

Table 8-15. *Summary of rf control specifications for each station.*

sector performance are looser than the accelerator performance goals. Since different errors have different interaction lengths, different relaxations of tolerances apply.

An example is found in the tolerance on the energy gain of each station, where the modeling code must know the beam's energy to scale the magnetic lattice. Errors in the energy result in the phase of the betatron oscillation "slipping" from the modeled values, generating errors in correction by steering and cascaded feedback systems.

Phase and Amplitude Specifications

As noted above, an additional complication (and relaxation of tolerance) comes from optimizing tuning procedures and feedback systems. Sensitivity to accuracy errors in phase and amplitude are quite low, while slow changes and fast jitters may range from annoying to debilitating for machine operation, depending on the power spectrum and the beam energy. Table 8-15 summarizes these goals.

Energy Profile Control

Knowing the expected beam current and pulse profile, a shaped rf voltage output is computed and programmed into the SLED-II energy compression system. Ramping allows a pre-loading of the accelerator with rf energy prior to the passage of the first bunch, with a reduced energy gain for the first bunch. The accelerator rf power immediately following the start of the passing beam would be near the full available power. This is done to allow the wakefields (which diminish the energy gains) of the leading bunches to be compensated before the subsequent bunches arrive.

The ramping of the power from the saturated klystrons can be done by either of two methods: identical phase modulation or complementary (opposite) phase modulation of the two klystrons in a pair. Identical phase modulation is achieved by applying identical time-dependent phase modulation to each of the two klystrons and thus to the SLED-II compressor input, such that four delay cycles of stored power leaving the delay line ports, plus the incoming klystron power, results in the desired rf voltage and phase modulation at the input to the accelerator during the beam's passage. Alternatively, the complementary phase modulation method takes advantage of the symmetry of the power combiner joining a pair of klystrons. Pulse shaping is achieved by phase modulation of the paired klystrons by equal amounts in opposite directions, resulting in a pure amplitude modulation at the SLED-II compressor input, with unused power being dissipated as heat in the combiner load. Complementary phase modulation need not apply any time-dependent phase modulation at the SLED-II input. In the absence of system bandwidth considerations, both methods can generate the same waveforms for the duration of the rf filling time and beam passage.

For the NLC, we plan to use the method of complementary phasing (in opposite directions) of the accelerator klystrons to program the desired time-dependent SLED-II output. This method has several advantages over the identical

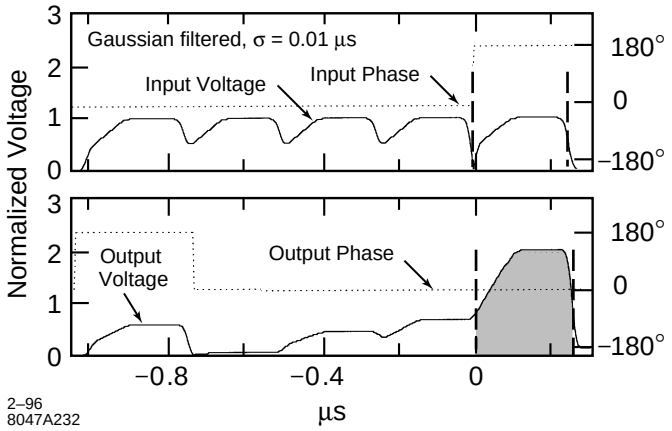

Figure 8-48. *Illustration of SLED-II compression with pulse shaping achieved by complementary modulation of the phases of paired klystrons (equally, but in opposite directions) to achieve the input power modulation. Note that the phase of the SLED-II input is zero (modulo 180°), allowing use of simple nulling phase detectors. Klystron impulse response modeled as a gaussian with* $\sigma = 0.01\ \mu s$.

phase-modulation method from the perspectives of improving performance and simplifying rf control design. These advantages are:

- Reduction of power dissipated in the accelerator. The unused power is dissipated in the power combiner load and not in the accelerator.
- A simpler correction for average power effects when the bunch count or the beam current is temporarily reduced.
- The bandwidth and finite rise time of the klystrons and drive systems do not result in complicated waveforms which may decrease performance and increase diagnosis and maintenance costs.
- A simpler monitoring system. Since the phase input and output of SLED-II are approximately flat (modulo a 180° phase jump), lower cost phase detectors may be used: either simple mixer-type phase detectors or quadrature-type phase detectors operating at a fraction of their potential capability. Phase modulated waveforms require detectors with a large phase dynamic range, and thus careful calibration to insure that changes in the overall phase do not affect the diagnostic reliability.

Sample modulation waveforms for the complementary phase modulation method are shown in Figure 8-48. For this study, the desired SLED-II output pulse shape is a ramped increase in gradient from 40% to 100% over the 100-ns fill time, followed by a 150-ns flattop. (See Section 8.2.3 on Transient Beam Loading.) In this study, the klystron's output bandwidth is modeled by the convolution of a 10-ns gaussian with an ideal klystron's output in the time domain. While there are an infinite number of equivalent solutions satisfying the output requirements, the following simple model with five-fold repeated symmetry for each of the compressed sub-sections is proposed to reduce the diagnostic problems presented to the rf systems maintenance personnel. Amplitude is shown as a solid line, phase as dotted, and the fill/acceleration interval is delineated with vertical dashed lines.

The desired resultant SLED-II envelope and the mathematical basis for the waveform are introduced in Section 8.2.3, “Transient Beam Loading”. The operational goal for the NLC rf control system is to minimize beam energy errors; thus the controls must allow the development of models and algorithms for near real-time modification of the input waveforms to achieve the necessary energy-gain profile needed for the real current pulse shape and charge.

Knowledge of the Energy Gain

Control of the machine lattice (the magnetic optics which guide the beam) requires knowledge of the energy of the beam at all points in the accelerator, and of changes in the energy profile incidental to any significant bunch phasing, klystron phasing, or klystron population changes. Absolute calibration of the results is not as important as the consistency of the derived energy gain readings, since the total machine energy is ultimately determined by direct spectrometer measurements.

Modeling inputs use the nominal energy gain of the individual stations, beam current information, and other factors to compute the energy profile. Rf controls must be able to accurately report the approximate energy gain expected from the station as well as the current operational status of the station.

Experience with the SLC at SLAC has shown that the models for machine operation must be updated whenever the klystron population is varied, and that consistency in the predicted energy contribution of any individual station is more important than the absolute accuracy. Even so, each station's energy contribution has been individually calibrated using bolometric power meters and known coupling ratios, and the results have been compared with direct beam-based energy contribution measurements. Discrepancies in beam energy of greater than 5% have been observed in the two methods, and correction factors are generally placed in the database to insure that the instrumentation accurately reports each station's energy gain.

Phase Control

The DC phase of the output from each SLED-II compressor will be monitored and set to the nominal value using low-level phase shifters upstream of each klystron. Desired phase values will be derived by using a coaxial loop loosely coupled to the last cavity of an accelerator section and comparing a beam-induced rf signal in the accelerator section with the SLED-II rf signal.

Phase Stability

Stable beam operation is required over a range of 1 to 90 bunches and bunch charges varying between 10^9 and 10^{10} electrons per bunch. Uncorrected changes in either parameter vary the power deposited in the accelerator sections, with resultant changes in accelerator temperature of a degree Fahrenheit and average phase changes of 3° to 5°. Thermal characteristics of the accelerator structure are discussed in Section 8.2.5.

Corrections for changes in microbunch configuration will be done iteratively, allowing local controllers to modify energy profile appropriately.

Machine protection system (MPS) algorithms immediately reduce the bunch count to zero in the presence of beam loss. Operation resumes with a single-bunch, high-emittance probe beam at a low rate (1–10 pulse per second), followed by single bunch operation at full machine rate, with a ramped bunch count increase as machine losses permit. Multibunch operation is always initiated with a single bunch probe beam on the previous machine cycle. Bunches are always deleted from the tail of the pulse, and thus will not require real-time modifications to the rf shaping. (Machine protection issues are discussed in Chapter 16.)

Machine repetition rate will be stepped up from the lower to full bunch count, with stable machine operation demanded without any allowance for thermal corrections. Corrections for this effect must be incorporated into the design, reducing the related phase error to less than 0.1° maximum net phase excursion averaged over all klystrons. (See Section 8.6.2.)

Two control paradigms are being considered, both of which may be required to meet the phase-stability imposed by the above MPS requirement for the main linacs. They are:

- Complementary phase modulation of pairs of klystrons to reduce the excess power entering the accelerator by dissipating power in the fourth port of the primary power combiner. In the same manner as the power is ramped up for the fill time prior to injection of the beam, rf amplitude will be stepped down following the passage of the leading bunches to reduce average power to the beam-loaded level. (This requires that klystrons be separately driven by pairs of klystron drivers to allow fast control of power.)
- Feed-forward control of the thermal regulation system for the accelerator cooling water to directly compensate for anticipated thermal changes related to beam current changes. Control using such regulation could practically reduce the thermal excursion by factors of 10 to 30, bringing the net effect to within operational tolerances. Such a feedback system is an NLC-specific development project since the requirements are more stringent than those generally met by industrial control specialists. Experience at SLC also indicates that use of thermal controls of accelerator related water systems has very high installation and maintenance costs, and thus is not being considered as the preferred option.

Phasing of the Accelerator

Phasing of the accelerator will use the beam to establish the optimal phase for each rf station. Fields left in the accelerator following the passage of a short pulse (containing 1 to 10 bunches of 3 to 7×10^9 electrons per bunch) will be used to determine the phase of the beam via a coaxial loop loosely coupled to the last cavity of an accelerator section. Phase measurement equipment monitoring the phase of the rf exiting an accelerator section will measure: a) the rf in the absence of beam loading, b) the beam-induced rf in the absence of klystron rf, or c) a vector combination of klystron and beam-induced rf during normal operation. The optimal accelerating rf phase will be determined from the difference (modulo 180°) of the klystron-driven phase and the beam induced phase, with knowledge of the current beam offset phase (the "phase closure" value). The difference in the readings will be used to phase the klystron station during routine setting of the nominal station phase offset. The phase signal during normal operation (case c) is of limited interest, and is not used for station operation.

8.6.3 Systems Overview

Low-level Accelerator-wide RF Distribution

Phase-stable distribution of X-band rf over the entire length of the NLC by coax is infeasible with current technologies. The NLC rf distribution will be based on:

- A master X-band oscillator.
- Fiber-optic distribution of primary rf to satellite rf oscillators using temperature-stable fiber distribution line.
- Phase-locked ultra-stable satellite oscillators at each sector locked to a phase-shifted reference derived from fiber optic distribution.
- Local beam-induced rf reference cavity near each satellite oscillator.
- Phase feedback controlling phase offset between fiber reference and local oscillator to null phase detector monitoring beam reference cavity.

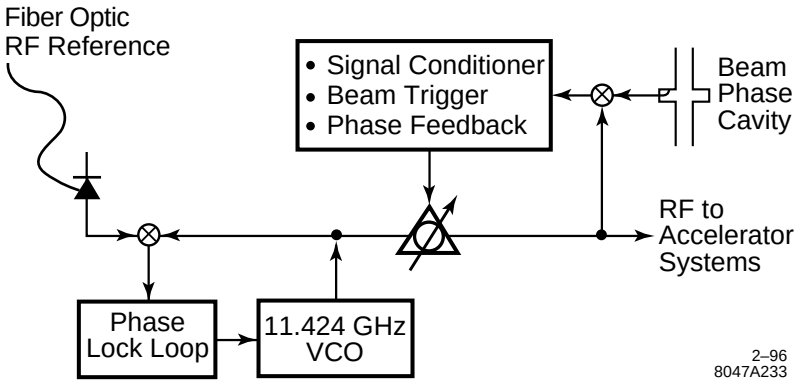

Figure 8-49. *Schematic of a local rf source for each sector. Sector rf is derived from a low-noise oscillator with phase locking to detected beam-induced phase reference. Fiber-optic reference using liquid-crystal polymer (LCP) time-stabilized fiber provides stable reference in absence of beam.*

Sector RF Source

Each sector will receive an amplitude modulated fiber frequency source, which will serve as the basis for the local oscillator's phase lock to master clock. The local oscillator serves as an extremely narrow-band filter, reducing the quantum (shot) noise and thermal noise power that would otherwise dominate the short term stability of an optical based distribution system. Distribution within each sector is achieved using low temperature coefficient copper coaxial lines [Andrew], which deliver a low power signal to each station. An additional cable will transmit the signal to the next sector, allowing a cross-check of each system's stability.

The local beam phase reference will consist of a tuned cavity, or of a few cells similar to the accelerator, that will provide a temperature-invariant reference signal or a high-bandwidth beam pickup followed by an appropriate bandpass circuit. The resultant phase information will be used to remove the local source's residual phase errors prior to distribution to the rf devices in the sector, as shown in Figure 8-49. The use of a beam pickup is considered a technical option which can eliminate an additional tuned cavity in each sector but will require the development of an specialized phase monitoring circuit. (Beam-phase pickups are used successfully at the SLC at SLAC for damping ring phase control at somewhat looser requirements.) Knowledge of the present beam parameters is required for this feedback loop, since the induced phase depends on the so-called “Phase closure” setting.

Long-haul distribution using fiber optic transmission lines has shown promise at SLAC and abroad. Special time of flight stabilized single mode fiber is manufactured with a proprietary coating system [Kakuta 1987, Kotseroglou, Sumitomo, Urakawa 1991], which substantially reduces the thermal drift inherent in glass-based transmission systems. Communication starts at a source laser using either direct intensity modulation or a narrow-band laser followed by an intensity modulator. Parallel fibers distribute signals to local sources in key sectors, where secondary fiber optic lines carry frequency information to each sector's rf source. Instrumentation at distribution points will consist of a local oscillator followed by a laser and modulator system as described above, and may share the oscillator with phase feedback of the standard local source oscillator. An additional fiber will transmit rf information to the next distribution point, allowing a cross-check of each system's stability. The long-haul fibers will be equipped with an interferometric length correction to remove the majority of the fiber's residual phase error. Similar fiber systems are used at SLAC to synchronize a laser for the E-144 experiment to the electron beam [Kotseroglou], with a residual fiber sourced phase error believed to be better than a fraction of a degree at X-band. The use of interferometric length correction has been used successfully for the primary rf distribution system for the two-mile-long SLC linac at SLAC, with distribution-based errors believed to be better than several degrees at X-band diurnally.

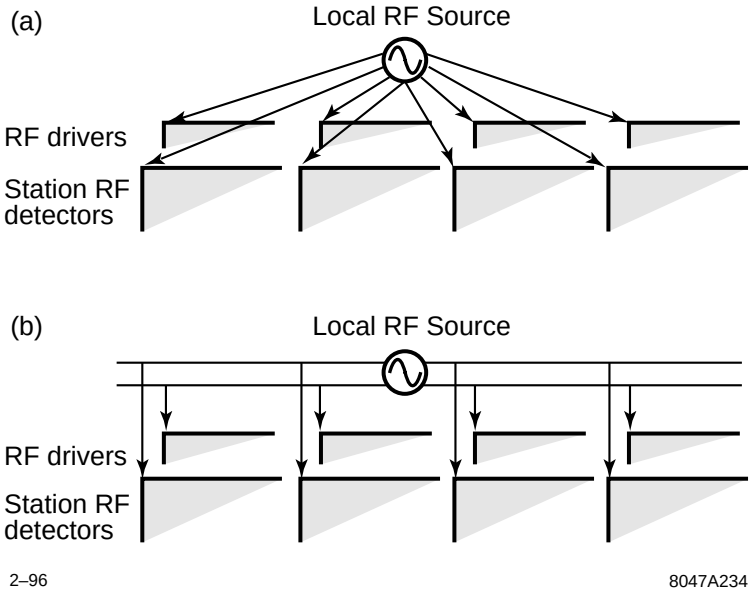

Figure 8-50. *Two methods of rf distribution within any given sector. The use of redundant distribution lines allows identification of distribution-related phase errors. The first schematic (a) uses sets of dedicated lines to each klystron/modulator and instrumentation station, while the second (b) uses common lines for each function, with signal extraction through the use of a directional coupler.*

Sector RF Distribution

Conventional coaxial distribution systems are proposed to transport rf drive and reference signals from the sector's rf source to each station. The choice of coaxial lines is based partially on the quantity of such connections and demonstrated reliability of the medium. Fiber-optic based transmission has been considered, but fails to meet the phase noise requirements of the klystron rf instrumentation without the use of an additional local oscillator at each station.

The cable plant consists of two identical rf cables from the sector rf source to each station: one cable is used for the amplification of the high-power rf by the linac klystrons, while the second cable is used solely for the rf instrumentation for a local phase reference (Figure 8-50). The use of a second reference helps for identifying distribution-related phase problems as anomalous station phase errors which can (with care) be identified and corrected. Experience at the SLC at SLAC has shown such redundancy is critical in identifying problems in the rf distribution system and has been specifically cited as a major factor in achieving the SLC's availability and reliability.

Station RF Components

The smallest unit for control of rf-related devices is the station. Each station consists of a pair of klystrons driven by a common modulator. Rf power is combined using a hybrid “T” with a load on the fourth port, and is compressed in time with a SLED-II compressor. Each station supplies power to four accelerator sections, as shown in Figures 8-47 and 8-51. Rf drive and rf reference signals come directly from the sector's low level rf distribution system on separate cables to allow diagnosing of rf distribution-related failures. The phase modulation generators will deliver different phase modulation when a klystron station is at standby (off-beam) time to maintain correct thermal equilibrium.

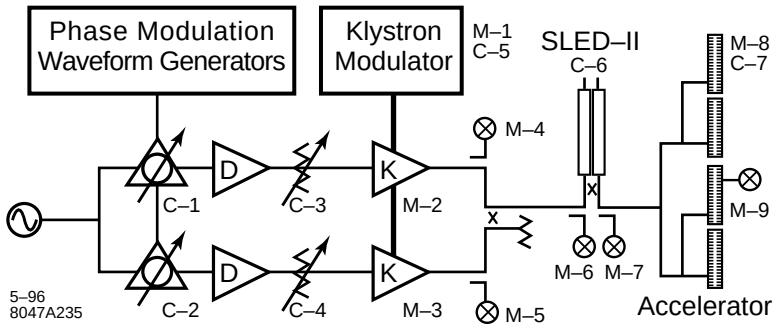

Figure 8-51. *Schematic of rf components and controls for each station. Klystron drive is derived from the sector's rf source, with an adjustable phase and drive control for each klystron. Major control and monitor points are shown.*

C-1 C-2	Klystron Phase Controls	Correction for slow and thermal drifts.
C-3 C-4	Klystron attenuator	Set for saturated operation. Part of klystron protection system.
M-1 C-5	Modulator monitor and controls	Triggering of klystron in response to control systems needs, readback of modulator status plus modulator (beam) voltage and current waveforms.
M-2 M-3	Monitor of klystron parameters	Signals such as klystron vacuum, body beam interception, etc.
M-4 M-5	Monitor of klystron rf forward and reflected signals	Klystron phase and amplitude waveforms. Primary monitor point for klystron performance. Reflected power for klystron protection systems.
M-6	Monitor of SLED-II input	SLED-II input phase and amplitude.
C-6	SLED-II cavity length tuning control	Motors or heaters as chosen to achieve modeled compression factor.
M-7	Monitor of SLED-II output and accelerator input	Phase monitor point for “trimming” phase of klystrons. Phase and amplitude waveforms of forward rf.
M-8 C-7	Accelerator cooling monitors and controls	Adjustment of water cooling set points and readback of temperatures.
M-9	Accelerator output monitor	Phase monitor allows independent measurement of phase of beam and phase of klystron system.

Table 8-16. *Monitor and control points in the rf system.*

Monitor and control points are summarized in Table 8-16.

Klystron RF Driver (TWT or Low-power Klystron)

There are various schemes for providing the approximately 1 kW of pulsed rf needed to drive each high-power klystron. It is useful to have individual drivers because the various phase manipulations involved in the operation of the rf compressors are best done at the milliwatt-level. Power-combining of the two klystrons on the single modulator is done by phase modulation of the two klystron inputs by equal amounts in opposite directions. This has the effect of sending the desired vectorial sum into the rf pulse compressor and dumping the vectorial difference into a load.

There exists extensive traveling-wave tube (TWT) technology at this frequency and power level as a product of military applications. The available TWTs are reliable, but fairly complex to manufacture and operate. They have already been extensively cost-optimized, and are still very expensive.

A small X-band driver klystron of fairly narrow bandwidth and modest gain could be designed. In construction, it would be relatively simple compared to a TWT. It is possible that after the initial engineering models are tested, a modest program of redesign for automatic manufacturing could reduce the unit cost significantly.

Low-level RF Station Controls

The rf for each klystron is appropriately phase modulated, at milliwatt power levels. Downstream from the kilowatt-driver amplifier, klystron attenuator controls are used to maintain saturation levels of individual klystrons. The attenuators will also facilitate soft run-up of stations as might be required following venting of vacuum systems. Interlocks are discussed in Section 8.7.3.

Klystron and Modulator RF-Related Control and Monitor Points

Each station has a single modulator station powering two klystrons. The modulator instrumentation and protection system receives triggers from the rf support system, as well as indications of excessive reflected power requiring a modulator trip.

When the station is not used for the current beam pulse, it is fired in a standby mode, where the trigger time is offset from the normal beam time by at least several microseconds, and the modulation phase patterns are altered to maintain thermal equilibrium in the absence of beam loading. Appropriate triggers and phase controls are supplied by the rf support systems. For the accelerator at SLAC, standby time offsets are used as part of the beam containment system to insure that even a dark-current beam is not generated coherently through the linac. These delays are set on a sector-based pattern and implemented in hardware. The NLC may require similar logic to ensure that the radiation safety considerations have been met, without burdening the operation with unreasonable thermal settling delays.

The modulator system will provide the rf controls status information as well as a few high quality video-bandwidth monitoring signals of klystron beam voltage and beam current for monitoring by the rf digitization system (three channels per station).

High-Power RF Monitor Points

Between the output of the klystrons and the input of the accelerator is a high-power combiner and a SLED-II pulse-compressor system. Forward and reflected rf phase and amplitude are monitored at each point as identified in Figure 8-51.

Klystron forward output couplers are used to diagnose the performance and stability of individual klystrons, while reflected output peak values are provided to the modulator protection system. Phase and amplitude waveforms for the forward rf signal are required.

Combiner output signals are used to identify the performance of the SLED-II system, while reflection signals measure SLED-II tuning accuracy. Phase and amplitude waveforms are required in the forward direction (combiner output), while amplitude is required for the reverse output (SLED-II reflection).

The SLED-II output coupler is used to routinely trim the phase of the two klystrons to meet accelerator phase requirements. Outputs at this point are expected to exactly reflect the modeled rf power profile, and differences in this waveform will be corrected by cautious modifications to the klystron input waveform. The phase stability of this monitor point must exceed the station's phase stability requirements. Phase and amplitude waveforms for the forward rf signal are required.

Peak values of each monitor for each pulse will be sampled and digitized. Waveform recording of each channel will occur periodically and as requested by the control program. Periodic analysis allows a historical monitor (jitter and values) to be stored over days and months, while on request waveform acquisition allows the control room and maintenance personnel to diagnose suspect devices.

Sample size and resolution must allow device bandwidth limited signal acquisition with sufficient granularity. Minimum sampling speeds of 100 MSample/second and buffer depths of 256 allow the entire pulse to be represented with 10-ns sample sizes. 0.1% amplitude and 0.1° phase stability requirements can be met with digitizers with resolution limits of 12 bits per sample ($\pm$2048). The actual instrumentation sampling speed and resolution will be determined to take best advantage of commercially available instrumentation.

There are several cost-containment decisions which must still be made regarding station instrumentation. Current costs for VXI-bus (computer interfaced) digital oscilloscopes of the required bandwidth are quite high, and suggest that dedicated signal acquisition hardware for each channel will be prohibitively expensive. Cost control may dictate multiplexing of the signal inputs into a common digitizer. If the reliability of multiplexers can be improved, their use can reduce instrumentation investments at the operational cost of limiting simultaneous monitoring of multiple channels within a station. Alternately, instrument development efforts combined with waiting for the growth of the related industries may allow cost effective solutions not currently available.

Instrumentation may be shared between adjacent klystron stations or between clusters of stations, resulting in further reductions in cost. The locations and granularity of instrumental and computational support in the NLC must be based on an evaluation of the cost and power of available instrumentation. Serious attention must be paid to the relative costs of shipping rf signals in phase stable cables *vs.* the local conversion of phase data to video and shipping video to the analysis points. The most probable configurations are to have instrumentation centrally located between pairs of stations, or individual instrumentation for each rf station.

SLED-II Delay-line Tuning

The SLED-II delay lines must be tuned to maintain both differential and common errors to a small fraction of a wavelength. This tolerance can only be met through the use of an active temperature or electrical length control.

Differential length errors will result in rf power reflections into the klystrons and reduced energy gain for the station. Differential length adjustment must be done by minimizing the rf power reflections back into the klystron power combiner (by tuning). Common and differential length errors result in a reduction of the station's energy gain. These errors can be removed mechanically by controlling the delay line length. The common length errors can be removed electronically by step-modulation of the input phase to compensate for the common phase-length error in the SLED-II delay lines. Common length errors can be directly measured from the SLED-II forward power coupler as follows: (1) measure the phase of the earliest delay-line fill (this is from the reflections off the coupling irises), and (2) measure the phase of a subsequent fill (reflections off the irises plus the emitted field from the cavity). The second measurement should be at a phase angle of 180° shifted from the first.

The SLED-II delay lines in the NLC will be tuned either by sliding choked shorts at the end of each line (as used in the NLC Test Accelerator), or by thermal control of delay lines. Either solution will work.

Accelerator Control and Monitor Points

The pickup loops at the downstream end of each accelerator structure will extract the beam-induced signal for phasing the accelerator, as discussed in Section 8.6.2. Temperature monitoring of the copper of the accelerator combined with measurements of the average rf power and beam current will be used to set the water system to the optimal control temperature. The pickup loops at the downstream end of the each accelerator structure will be used to optimize this control. The time-dependent phase angle of the output of the accelerator following the passage of a short (single or few bunch) beam will be used as a cross-check of the temperature settings for the accelerator structures.

Accelerator RF Beam Position Monitor

Signals from the damping manifold monitor couplers will be used to optimize the transverse positions of the accelerator structures to minimize steering due to dipole wakefields.

Trigger Timing

The timing system must deliver to each klystron station the appropriate triggers and machine-configuration information to allow the triggering of the modulator and the rf and protection sampling systems. Configuration information will include information identifying if the trigger should result in a beam acceleration, or if the station is on standby timing for the next pulse. Due to the Machine Protection System constraints, the triggers and configuration information must be delivered and sampled at least 100 μs prior to beamtime. The modulator trigger and rf shaping electronics will require timing that is adjustable in steps of about 5 ns, with short- and long term-stability a factor of two smaller.

Feedback and Related Systems

Active feedback systems, similar to those used in the SLC, are required to meet the NLC beam quality and machine performance requirements. Feedback systems, as defined below, which will directly interact with the rf systems are:

- Machine Energy Feedback
- Machine Energy Spread Feedback
- Bunch Energy Spread Feedback
- Pulse Energy Error Feedback
- Intensity Energy Feedforward
- Downstream Feedback Systems

Figure 8-52 illustrates the parameterization of energy and energy spread space for the NLC.

"Machine energy error" is the error in the energy of the bunch centroid. Errors are measured by the feedback system using beam position monitors in a dispersive region and computing the beam parameters (ΔE, X, X', Y, and Y') using the modeled machine lattice. Changes in desired accelerator energy gain are computed and transmitted to the effected sector controllers. The energy gain is controlled by deliberately misphasing sector pairs of klystrons with complimentary phase offsets, producing changes in the net energy gain without affecting the beam energy spread.

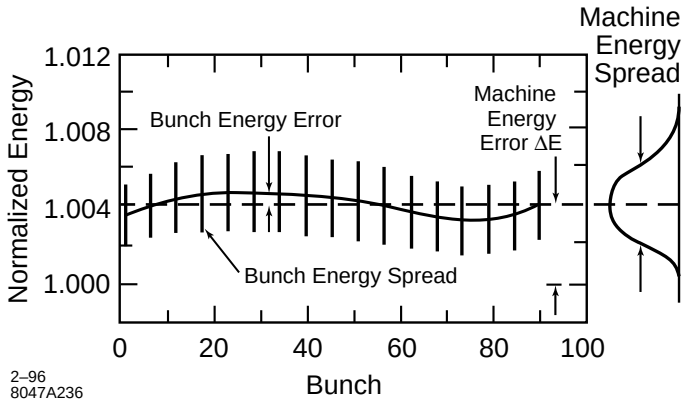

Figure 8-52. *Plot of selected bunches within a NLC pulse. Parameters Energy Error, Pulse Energy Error, and Bunch Energy Spread are shown in the central graph. The projection at right depicts total machine energy spread, with the Machine Energy Error as its mean, and the width representing both the Pulse Energy Error and the Bunch Energy Spread.*

Experience in the SLC suggests that at least $\pm 2\%$ of the total gradient be available for total energy correction, which will be used to correct for gradient errors in the accelerator, and for changes in centroid energy from energy spread and pulse energy corrections [Sheppard 1987]. Experience also suggests that the feedback correction rate for this system will require at least 20 energy corrections per second at 180-Hz machine repetition rate.

Machine energy spread is measured by a dedicated spectrometer which measures the composite energy spread of the entire bunch train. Energy spread errors are fixed by changing the injection phase of the bunch from the damping ring (the "phase closure"). Communication channels for this loop are similar to those for the ΔE correction with a system speed of several corrections per second.

Average beam energy errors and individual bunch energy spread are continuously measured by a dedicated spectrometer which can separately resolve the energy differences and the rms energy spread of the bunches. Energy errors are corrected by designing a modified SLED-II compressed rf profile, while energy spread errors in the individual bunches are corrected by controls in the damping ring extraction system and by the imposition of a phase modulation in the shaped SLED-II output. Communication channels for this loop are similar to those for the ΔE correction with a system speed of order a correction per hour with results available for history buffer logging every several minutes.

Intensity feedforward systems require the energy of the accelerator to be changed within a damping-ring store time. The measured stored beam current is used to predict an expected centroid energy shift ΔE due to off-normal beam loading effects. Communication channel speeds for this loop must be quite high, A dedicated channel to each sector may be necessary to maintain a rate of 180 corrections per second [Jobe 1991, Seeman 1991b].

Specific downstream feedback systems (such as steering systems, energy feedback systems, and detector noise minimization systems) may require knowledge of klystron errors or modulator protection cycles. Detector noise minimization systems, for example, will need to know if an rf station in the early section of the machine has faulted prior to computing orbit corrections to minimize beam scraper spray into the detector. Additionally, in the presence of extended error conditions (such as a vacuum fault), the machine protection system might abort beams to minimize detector backgrounds. In the SLC, each rf station announces its faults to the control system using a dedicated communication channel [Jobe].

Parameter	Resolution
Average Energy Measurement	$<0.5\%$
Machine Energy Spread	$<0.05\%$
Bunch Energy Spread	$<0.1\%$
Bunch Energy Error	$<0.05\%$

Table 8-17. *Spectrometer resolution.*

8.6.4 Spectrometers

Primary machine optimization for the rf phase settings for the individual stations will use beam-induced phasing; all other optimizations will require a beam line spectrometer. Resolution requirements are summarized in Table 8-17 and such measurements should be available at the machine end, and at several points along the accelerator.

In order to meet target resolutions for machine and bunch energy spread, the spectrometers must be located at points of high dispersion ($\eta \gg 2000\sigma$). For a horizontal beam size (σ) of 0.1 mm at the spectrometer, the horizontal dispersion (η) should be greater than 0.2 m. Backgrounds for the spectrometer detectors must be sufficiently low for the spectrometers to operate in the machine environment.

The spectrometer detectors could utilize a pulsed laser beam probing the density of the bunch at the high dispersion point. Compton scattered electrons and a scanned laser probe beam, would provide all the information required. Individual bunch analysis might not be necessary, if the detector is capable of reporting separate values for early, middle, and later bunches in the train with sufficient resolution.

8.7 RF Protection and Monitoring Systems

All protection systems are serviced by dedicated local computers or programmable logic controllers (PLCs) plus some additional faster protection circuitry. This protection system combines the logical protection and operating functions of the modulator, the klystron, and the waveguide and structure systems. It includes the water-cooling system, the temperature-monitoring system, the various electronic monitors of the klystron support power supplies and the modulator electronics, the related vacuum systems, and the high-power rf protection. While these various protection and interlock systems are serviced by one PLC, the functions will be discussed separately in the sections below. The PLC communicates with the central computer to allow remote data logging, error reporting, and configuration control.

8.7.1 Waveguide Protection and Monitoring

Protection includes the high-power X-band waveguide, the SLED-II energy compressors, and the disk-loaded waveguide. Other than accelerated electron beam interception damage over which this interlock system has no control, the primary causes of potential component damage are arcing brought on by poor vacuum and loss of cooling. Because of the limited pumping speed of small waveguide, the high-power rf distribution system contains many individual ion pumps. It is expected that these ion pumps will be powered by a small number of multiple-output ion-pump power supplies that will be interlocked with the rf system module.

There will be a limited number of reflected energy pickup points, especially in the output arms of the klystrons, that will detect reflected energy due to arcs or SLED-II mistuning, and will operate through the PLC to inhibit either the drive rf to the klystron, or the klystron pulse modulator.

8.7.2 Klystron Protection and Monitoring

Klystron protection is accomplished by providing monitoring and interlocks on the systems which provide power and cooling water to the klystron, the klystron vacuum and the rf systems including the system vacuum. These monitoring and interlock signals are both analog and digital.

Most of the interlocking is done with a PLC which provides the interlocking and sequencing logic for the klystron system. Critical interlocks such as Klystron Output Reflected Power, which require faster response time, may be hard-wired for speed, and redundant to the PLC interlock.

The water system is designed for two klystrons per station with separate water circuits for each klystron. Each klystron will have a water circuit for its anode, its body and window and its collector. This water manifold will provide the cooling water for the klystron and modulator oil tank. Water flows will be monitored by the PLC for interlock and general monitoring functions.

Each klystron is instrumented separately for window temperature and body temperature. Increases in the body temperature, which increases if beam interception increases, is fed to the PLC and compared against a predetermined level; exceeding this level will cause the PLC to turn off the klystron beam. Window temperature will cause the rf drive to be removed if a maximum temperature is exceeded.

The klystron ion pumps will be connected in parallel into one controller for each klystron. The controller will have an internal vacuum pressure limit interlock which will be manually set. An excessive vacuum pressure interlock will turn off the klystron beam.

The klystron heater circuit, separate for each klystron, is equipped with an interlock for minimum heater current, and a warm-up time delay is provided by the PLC once the minimum current is exceeded. The klystron beam is inhibited until these interlocks are cleared. Analog signals for heater voltage and current are read by the PLC.

Klystron peak-cathode voltage and peak-cathode current are digitized in the support electronics and read into the PLC for over-current and over-voltage interlocking and into the main computer system for data-taking and storage. Klystron heater and high voltage operating hours will be totaled in the PLC.

The rf output waveguide transport system, which is under vacuum, is connected to ion pump supplies with manually set high-vacuum pressure interlocks. These feed into the klystron and modulator PLC to remove the rf drive when there is an excess pressure condition.

The rf output waveguide transport system also has various forward and reflected monitor points. An example of one of these monitor points is at the output of the klystron. These signals are each transmitted through a four-port coupler. One of these ports feeds a crystal detector into a video amplifier interlock system which provides buffered video outputs, a peak and hold-detected output, and a comparator circuit. The comparator circuits with manual adjustment can be used to interlock any of these detected signals. The output of the interlock is sent to the PLC for action. Klystron-reflected power is one of the critical interlocks which will also be hard-wired from the video amplifier interlock to directly remove the rf drive.

8.7.3 Modulator and Support Electronics Protection and Monitoring

The modulator control, interlocking, and protection is also accomplished through the PLC. The main protection interlocks are excessive EOLC current (for a klystron arc) and high-voltage-power-supply-overcurrent (HVOC).

The modulator protection system contains discharge solenoids, barriers, and door interlocks for protection of both personnel and equipment. It may be connected to the overall accelerator Personnel Protection System.

Thyratron warm-up time delay will be provided in the PLC after the thyratron electrodes are energized. Thyratron heater hours will also be totaled in the PLC.

8.7.4 Klystron and Modulator Logic Controller

At the present time, PLCs are being used for monitor and interlock functions in the Klystron Test Lab. On the NLCTA, two PLCs are used at each klystron station to provide modulator interlocking and control, and to monitor the operation of the klystron rf system and the various interlocks that protect the rf station. It is expected to use this same technology for each NLC rf station, but the general PLC will be replaced by a dedicated logic controller that is designed and optimized for NLC rf station operation.

8.7.5 Modulator Interactions with the Machine Protection System

The Machine Protection System (MPS) requires that the beam quality be maintained at an energy of at least 85% the expected energy. This requirement is determined by the limited ability of the collimators and beam line transport systems to handle a wildly off-energy beam. Under certain failure modes, catastrophic system failures can result from a single errant pulse.

Because of the large number of klystron/modulator stations, the interactions between MPS and klystron controls are fairly weak. The MPS is expecting each station to deliver a readiness confirmation which will be summed using a majority logic system to insure that the energy profile of the machine will follow the modeled values within a small tolerance ($\pm$15% nominal). The implications and rules for the modulator and klystron systems are as follows:

1. The triggers for the klystron operation will be delivered at least 100 μs prior to beam time.
2. Following the receipt of the trigger, the modulator should be fully charged, and ready to fire.
3. The modulator system will promptly return a status indicator to the MPS controller indicating the readiness of an rf station and ability to fire its modulator.
4. Once confirmed, the modulator must fire at the designated time. Normal interlock conditions can not be allowed to disable modulator operation following the transmission of an MPS confirmation.

These MPS rules will insure that vacuum failure, AC power loss, trigger systems failure, and other larger system failures will not result in accelerator damage. Failures which are statistical in nature (such as thyratron triggering failure) are not expected to violate the MPS guidelines. (Special consideration also must be given to the readiness of kickers, dumpers, and perhaps certain critical klystron-driven systems.)

References

[SLAC 1993] SLAC, "Next Linear Collider Test Accelerator Conceptual Design Report", SLAC Report 411 (Stanford University 1993).

[Andrew] Andrew Corporation (Orland Park, Illinois), *Phase Stabilized Cables*, General Catalog No. 34, pp. 454–455.

[Adolphsen] C. Adolphsen, K. Bane, H. Higo, K. Kubo, R. Miller, R. Ruth, K. Thompson, and J. Wang, "Measurement of Wakefield Suppression in a Detuned X-Band Accelerator Structure", SLAC–PUB–6629, submitted to *Phys. Rev. Lett.*

[Adolphsen 1992] C. Adolphsen, K. Bane, G. Loew, R. Ruth, K. Thompson, J. Wang, "Measurement of Wakefields Generated in Accelerator Test Structures Using the SLC", SLAC–PUB–5941, 15th International Conference on High Energy Accelerators, Hamburg, Germany (1992).

[Adolphsen 1994] C. Adolphsen *et al.*, "Measurement of Wakefield Suppression in a Detuned X-Band Accelerator Structure", *Proc. 17th Int. Linear Acc. Conf.*, Tsukuba, Japan, submitted to *Phys. Rev. Lett.* (1994).

[Bane 1993a] K.L.F. Bane and R.L. Gluckstern, "The Transverse Wakefield of a Detuned X-Band Accelerating Structure", SLAC-PUB-5783, *Particle Acclerators* **42**, 123 (1993).

[Farkas 1974] Z.D. Farkas *et al.*, "SLED: A Method of Doubling SLAC's Energy", SLAC–PUB–1453, *Proc. 9th Int. Conf. on High Energy Accelerators*, Stanford, CA, 576–583 (1974).

[Farkas 1986] Z.D. Farkas, "Binary Peak Power Multiplier and Its Application to Linear Accelerator Design", *IEEE Trans. MTT*-**34**, 1036–1043 (1986).

[Farkas 1994] Z.D. Farkas and P.B. Wilson, "Ramping Profile for Exact Beam Loading Energy Compensation in the NLC Detuned Structure", NLC–Note 4 (Rev. 1), SLAC (December 1994).

[Farkas 1995] Z.D. Farkas and P.B. Wilson, "RF and Beam Loading Parameters for the NLC Detuned Structure with Damping Manifold", NLC–Note 15, SLAC (June 1995).

[Hoag 1993] H.A. Hoag *et al.*, "Flower-Petal Mode Converter for NLC", SLAC–PUB–6182, *Proc. 1993 Part. Acc. Conf.*, Washington, DC, 1121–1123 (1993).

[Jobe 1991] R. Keith Jobe *et al.*, "Energy Feed Forward at the SLC", SLAC–PUB–5541, May 1991, in *Proc. 1991 Part. Acc. Conf.*, San Francisco CA, 1464–1466 (1991),

[Jobe] R.K. Jobe, SLC Veto System, unpublished.

[Kakuta 1987] T. Kakuta and S. Tanaka, "LCP Coated Optical Fiber with Zero Thermal Coefficient of Transmission Delay Time", *Proceedings of the 36th International Wire and Cable Symposium*, Arlington, VA 234–240 (US Army Communications Electronics Command, Fort Monmouth, New Jersey, 1987).

[Kotseroglou] T. Kotseroglou, "Picosecond Timing of Terawatt Laser Pulses with the SLAC 46-GeV Electron Beam", SLAC–PUB–7130 (March 1996), submitted to *Nucl. Instr. and Methods*

[Kroll 1994] N.M. Kroll *et al.*, "Manifold Damping of the NLC Detuned Accelerating Structure", SLAC–PUB–6660, in *Proc. 6th Workshop on Advanced Accel. Concepts*, Lake Geneva, WI (1994).

[Kroll 1995] N. Kroll and K. Ko, private communication about work in progress (1995).

[Lanciani 1953] D.A. Lanciani, "H_{01} Mode Circular Waveguide Components", Conference on Millimeter Wave Research and Applications, Washington, DC (1953).

[Lavine 1991] T.L. Lavine *et al.*, "High-Power Radio-Frequency Binary Pulse Compression Experiment at SLAC", SLAC–PUB–5451, *Proc. 1991 Part. Acc. Conf.*, San Francisco, CA (IEEE 91CH3038–7), 652–655 (1991).

[Loew 1988a] G.A. Loew and J.W. Wang, "RF Breakdown Studies in Room Temperature Electron Linac Structures", SLAC–PUB–4647, presented at 13th Int. Symp. on Discharges and Electrical Insulation in Vacuum, Paris, France (1988).

[Matsumoto 1991] H. Matsumoto *et al.*, "Applications of Hot Isostatic Pressing (HIP) for High Gradient Accelerator Structure", *Proc. 1991 Part. Acc. Conf.*, 1008–1010, San Francisco, CA (1991).

[Matsumoto 1994] H. Matsumoto *et al.*, "High Power Test of a High Gradient S-Band Accelerator Unit for the Accelerator Test Facility", 17th Int'l Linac Conf., Tsukuba, Japan (1994).

[Nantista 1993] C. Nantista *et al.*,"High Power RF Pulse Compression with SLED-II at SLAC", SLAC-PUB-6145, in *Proc. 1993 Part. Acc. Conf.*, Washington, DC, 1196–1198 (1993).

[Nelson 1992a] E.M. Nelson, "A Finite Element Field Solver for Dipole Modes", SLAC–PUB–5881, in *Proc. 1992 Linear Accel. Conf.*, Ottawa, Canada (1992).

[OWGR 1993] "Technology and Costs for 2 Million Copper Discs of the CLIC Accelerator at CERN", Optische Werke G. Rodenstock (1993).

[Ramo 1984] S. Ramo, J.R. Whinnery, and T. Van Duzer, Fields and Waves in Communications Electronics, Second Edition (John Wiley & Sons, 1984). See Sections 7.8 and 7.10 for theoretical ohmic losses in waveguides.

[Read 1993] R.F.J. Read and W.J. Wills-Moren, Cranfield Precision Engineering, Ltd., Bedford, England. "Study Report for the Estimation of Unit Cost of Mass Producing Discs for the CLIC Accelerating Sections" (1993).

[Ruth 1993] R.D. Ruth *et al.*,"The Next Linear Collider Test Accelerator", SLAC–PUB–6252, in *Proc. 1993 Part. Accel. Conf.*, *loc. cit.*, 543–545 (1993).

[Ruth 1993a] R.Ruth *et al.*, "A Test Accelerator for the Next Linear Collider", SLAC–PUB–6293, in ECFA Workshop on e^+e^- Linear Colliders (LC92), Garmisch-Partenkirschen, Germany (1992).

[Seeman 1985] J. Seeman *et al.*, "RF Beam Deflection Measurements and Corrections in the SLC Linac", *IEEE NS32*, No. 5, in *Proc. 1985 US Part. Accel. Conf.*, Vancouver, Canada, 2629–2631 (1985).

[Seeman 1991] J. Seeman, "The Stanford Linear Collider", *Ann. Rev. Nucl. Part. Sci.* **41**, 389–428 (Annual Review, Inc., Palo Alto, CA, 1991).

[Seeman 1991b] J. Seeman *et al.*, "Multibunch Energy and Spectrum Control in the SLC High-Energy Linac", SLAC–PUB–5438, in *Proceedings of the 1991 IEEE Particle Accelerator Conference*, San Francisco, CA, 3210–3212 (1991).

[Seeman 1993] J. Seeman, "Accelerator Physics of the Stanford Linear Collider and SLC Accelerator Experiments Towards the Next Linear Collider", *Advances of Accelerator Physics and Technologies* (Vol. 12 of *The Advanced Series on Directions in High Energy Physics*), edited by Herwig Schopper, 219–248, (World Scientific, 1993).

[Sheppard 1987] J.C. Sheppard *et al.,* "Three Bunch Energy Stabilization for the SLC Injector", SLAC–PUB–4100, in *Proc. 1987 Part. Acc. Conf.,* Washington, DC (1987).

[Sumitomo] Sumitomo Electric Corporation (Yokohama, Japan), Liquid-Crystal Polymer (LCP) Fiber data.

[Takeda 1991] S. Takeda *et al.,* "High Gradient Experiments by the ATF", *Proc. 1991 Part. Acc. Conf.,* San Francisco, CA, 2061–2063 (1991).

[Tantawi 1993] S.G. Tantawi, K. Ko, and N. Kroll, "Numerical Design and Analysis of a Compact TE_{10} to TE_{01} Mode Transducer", SLAC–PUB–6085, *Proc. of the Computational Accel. Conf.,* Pleasanton, CA (1993).

[Tantawi 1995] S.G. Tantawi, private communication about work in progress (1995).

[Tantawi 1995a] S.G. Tantawi, A.E. Vlieks, and R.J. Loewen, "Performance Measurements of SLAC's X-band High-Power Pulse Compression System (SLED-II)", SLAC–PUB–95–6775, submitted for publication to *IEEE Microwave and Guided Wave Letters* (1995).

[Tantawi 1995b] S.G. Tantawi, R.D. Ruth, and A.E. Vlieks, "Active radio frequency pulse compression using switched resonant delay lines", SLAC–PUB–95–6748, in *Nucl. Instr. and Methods* **A370**, 297–302 (1996).

[Tantawi 1995c] S.G. Tantawi, T.G. Lee, R.D. Ruth, A.E. Vlieks, and M. Zolotorev, "Design of a multimegawatt X-band solid state microwave switch", SLAC–PUB–95–6827, in *Proc. 1995 Part. Acc. Conf.,* Dallas, TX (1995).

[Tantawi 1996] S.G. Tantawi, NLCTA test results, unpublished (1996).

[Thompson 1990a] K.A. Thompson and R.D. Ruth, "Controlling transverse multibunch instabilities in linacs of high energy linear colliders", SLAC–PUB–4801, in *Phys. Rev. D* **41**, 964 (1990);

[Thompson 1993] K.A. Thompson *et al.,* "Design and Simulation of Accelerating Structures for Future Linear Colliders", SLAC–PUB–6032, in *Particle Acclerators* **47**, 65–109 (1994).

[Thompson 1993a] K.A. Thompson and R.D. Ruth, "Simulation and Compensation of Multibunch Energy Variation in NLC", SLAC–PUB–6154, in *Proc. 1993 Part. Acc. Conf.,* Washington, DC (1993).

[Thompson 1994a] K.A. Thompson *et al.,* "Design and Simulation of Accelerating Structures for Future Linear Colliders", SLAC–PUB–6032, in *Particle Acclerators* **47**, 65 (1994).

[Urakawa 1991] J. Urakawa and T. Kawamoto, "The Improvement of TRISTAN Timing System", *Proc. 1991 Part. Acc. Conf.* (IEEE Catalog No. 91CH3038-7) 1555–1557 (1991).

[Vlieks 1993] A. E. Vlieks *et al.,*"Accelerator and RF System Development for NLC", SLAC–PUB–6148, in *Proc. 1993 Part. Accel. Conf., loc. cit.,* 620–622 (1993).

[Wang 1994] J.W. Wang *et al.,*"High Gradient Tests of SLAC Linear Collider Accelerator Structures", SLAC–PUB–6617, in *Proc. 17th Int'l Linac Conf., loc. cit.* (1994).

[Wang 1994a] J.W. Wang *et al.,* "High Gradient Tests of SLAC Linear Collider Accelerator Structures", SLAC–PUB–6617, presented at 17th International Linear Accelerator Conference (LINAC 94), Tsukuba, Japan, (1994).

[Wilson 1990] P. B. Wilson, Z.D. Farkas, and R.D. Ruth, "SLED-II: A New Method of RF Pulse Compression", SLAC–PUB–5330, in *Proc. 1990 Linear Accel. Conf.,* Albuquerque, NM (1990).

[Wilson 1992] P. B. Wilson *et al.*, "Progress at SLAC on High-Power RF Pulse Compression", SLAC–PUB–5866, in *Proc. of the 15th Int'l. Conf. on High Energy Accel.*, Hamburg, Germany (1992).

[Wright 1994] E. L. Wright *et al.*,"Design of a 50-MW Klystron at X-Band", Pulsed RF Sources for Linear Colliders: SLAC–PUB–6676, in *AIP Conference Proceedings 337*, Montauk, NY 1994, edited by Richard C. Fernow, 58–66 (AIP, New York, 1995).

Contributors

- George Caryotakis
- Dick Cassel
- Len Genova
- Saul Gold
- Harry Hoag
- Keith Jobe
- Ron Koontz
- Ted Lavine
- Greg Loew
- Bob Phillips
- Ron Ruth
- Sami Tantawi
- Kathy Thompson
- Juwen Wang
- Perry Wilson